AL-FURAT AL-AWSAT TECHNICAL UNIVERSITY - IRAQ

Design and Implementation of Microstrip Fractal Band Pass Filter with Metamaterial Performance

A THESIS

SUBMITTED TO THE COUNCIL OF COMMUNICATION TECHNIQUES ENGINEERING DEPARTMENT IN PARTIAL FULFILLMENT OF THE REQUIREMENTS FOR THE TECHNICAL MASTER DEGREE IN COMMUNICATION ENGINEERING

BY

Mohammed Yaqoob Yousif

(B. Sc Communication techniques Eng.)

Supervised by

Prof. Dr. Faris Mohammed Ali

April/2023

Abstract

The main key of research is to explore and investigate a microwave bandpass filters with improved overall performance and compact size exploiting advantages of the substrate integrated waveguide, SIW), such as the evanescent-mode SIW and half-mode SIW (HMSIW). Typically, the evanescent-mode (non-propagating mode) behavior is not preferred in the guided-mode microwave structures, where this type of mode operates under the cutoff frequency of the waveguide. Thus, the thesis combines the evanescent-mode and metamaterial techniques in one design to convert the non-propagating mode into a propagating one. The proposed design leverages both techniques.

The first part is to design the main unit cell, considering as the milestone (i.e., the core) of the whole work introduced in this research. The fractal H-I-hybrid shaped curve is cut out of the upper layer of the SIW in which this procedure aids to change signs and values of the constitution parameters (i.e., the permittivity and permeability) of the SIW. The propagation occurs only when both parameters are either positive or negative. In the former, the propagation-mode is called forward propagation mode, and the latter is known as the backward propagation mode. The propagation (forward) mode supports both phase and group velocities in the same direction, whereas these two velocities are in the opposite direction in the non-propagation (backward) mode. The SIW unit cell without the fractal slot has a cut frequency of 5.2GHz, whereas the SIW with fractal slot operates at the resonance frequency of 2GHz. Moreover, the 1st, 2nd, and 3rd iterations of the adopted fractal curves are utilized to design the unit cells. Depending on these investigations, the obtained miniaturization ratios are 32.9% and 51.6% for the 2nd iteration and 3rd iterations, respectively compared to the 1st iteration.

Next, the unit cell resonators are arranged linearly to design the 1st, 2nd, and the 3rd full mode-SIW (FMSIW) bandpass filters operating close to 2GHz. These filters have good performances with transmission coefficient to enhance the overall performance. The transmission coefficients S_{21} are very close to 0dB, demonstrating that the proposed filters have low losses which are close to zero. Also, the reflection coefficients S_{11} are less than –10dB, showing good matching within the passband.

Finally, the HMSIW bandpass filters will be demonstrated in the thesis, the HMSIW filters have the same responses of the FMSIW filters. This procedure aids to reduce the overall size by 50% to design very compact microwave structures. The magnetic wall crossing the longitudinally central line of the SIW is exploited to carry out this task. All the proposed filters are designed, analyzed, simulated by Advanced Design Simulator ADS and fabricated using Computerized Numerical Control CNC machine and tested by Vector Network Analyzer VNA with frequency rang starting from 10 Hz to 6GHz, The simulated and measured results are in very good agreement.

Acknowledgement

In the beginning, I would like to thank Allah Almighty, the most gracious, the most merciful, for giving me the determination and the strength to complete this research work in the field of communications technology engineering.

I appreciate the guidance and advice that I have received from the supervisor Prof. Dr. Faris Mohammed Ali for his continued support and encouragement to me.

I am very grateful to my family for their help, understanding, patience, and encouragement. Finally, I say to thank my father and mother for their patience, long-suffering and great encouragement, to whom I owe everything in my life from birth to death.

DEDICATION

To the greatest person that Allah has ever created, Prophet **Mohammad peace** is on him.
To the best person that Allah has ever created after His Prophet, **Imam Ali** peace be upon him.
To those who have all the credit on me, to those who were the cause of my existence, to my beloved **parent**.
To my **brothers**, my **wife,** my little **daughter** and my **friends**...
To all who supported and encouraged me to achieve my success.

List of Contents

CHAPTER TWO

CHAPTER FOUR

CHAPTER FIVE

List of Tables

List of Figures

List of Abbreviations

Abbreviations	Meaning
5G	Fifth Generation
ADS	Advanced Design System
BPF	Band Pass Filter
BW	Band Width
CAD	Computer-Aided Design
CM	Common Mode
CNC	Computer Numerical Control Machine
CPW	Coplanar Waveguide
CR	Capacitor
CRLH	Composite Right/Left-Handed
CRLH FM-SIW	Composite Right/Left-Handed Full Mode-Substrate Integrated Waveguide
CRLH HM-SIW	Composite Right/Left-Handed Half Mode-Substrate Integrated Waveguide
CSRR	Complementary Split Ring Resonator
DB	Dual Band
DGS	Defected Ground Structure
DNG	Double Negative Metamaterials
EBG	Electromagnetic Bandgap
ECSRR	Elliptic Complementary Split-Ring Resonators

E_{mn}	Electric Field
Eq	Equation
FBW	Fractional Bandwidth
FMSIW	Full Mode Substrate Integrated Waveguide
FOCSRR	Fractal open Complementary Spilt Ring Resonator
FR-4	Flame Retardant
FSS	Frequency Selective Surfaces
GHz	Giga Hertz
H_{mn}	Magnetic Field
HMSIW	Half Mode Substrate Integrated Waveguide
HTS	High-Temperature Superconductor
IFS	Iterated Function Systems
IL	insertion loss
LC	Indictor
LH	Left Hand
LPF	Low Pass Filter
LTCC	Low-Temperature Co-fired Ceramics
MHz	Mega hertz
MMIC	Monolithic Microwave Integrated Circuit
MSL	Micro-Strip Line
MTM	Electromagnetic Metamaterials
OCSRR	open Complementary Spilt Ring Resonator

PCB	Printed Circuit Board
PLH	Purely Left Hand
PRH	Purely Right Hand
Q-factor	Quality factor
QMSIW	Quarter Mode Substrate Integrated Waveguide
RF	Radio Frequency
RWG	Rectangular Waveguide
S-CSR	S-shaped complementary spiral resonators
SIR	Step Impedance Resonator
SIW	Substrate Integrated Waveguide
SMA	Sub-minotaur Version A Connector
SRR	Split Ring Resonator
TE10	Dominant Mode
TE101	Transvers Electric (Fundamental Mode)
TE201	Transvers Electric (Higher Mode)
TL	Transmission Line
TM	Transverse Magnetic
VNA	Vector Network Analyzer
WiMAX	Worldwide Interoperability for Microwave Access
WLAN	Wireless Local Area Network

Nomenclatures (Symbols)

Symbol	Meaning
β	The propagation constant
a_{equ}	SIW equivalent width
c	Speed of light (3 x 108) m/sec
d	Diameter of via holes
D_f	Fractal dimension
N	Number of order
a	Conventional rectangular waveguide width
b	Conventional rectangular waveguide height
f_z	Frequency of the transmission zero
τ_p	Phase delay
τ_d	Group delay
$\varphi(\omega)$	phase of the voltage transfer function
p	Space between two adjacent vias
Z	Impedance
λ	Wavelength
w	Width of the HMSIW
v_p	Phase velocity
v_g	Group velocity
f_c	Cutoff frequency

f_H	Highest frequency
f_L	Lowest frequency
f_r	Resonant frequency
h	Substrate height
k	Coupling coefficient
l	Substrate length
n	The refractive index
γ	The complex propagation constant
g	Slot width
S_{21}	Return loss
S_{11}	Reflection coefficient
μ	Permeability
$\tan \delta$	Tangent loss
ε	Permittivity
λ_g	The guided wavelength
λ_o	Free-space wavelength
μ_o	Permeability of free space
σ	Conductivity of the metal
$\mathcal{E}_{eff}$	Effective dielectric constant
ϵr	Relative dielectric constant of substrate

CHAPTER ONE

GENERAL INTRODUCTION

1.1 Introduction

Recently, researchers have paid attention to the salient features of the conventional rectangular waveguides, such as higher quality factors, lower losses, and larger power transmission capabilities compared to other transmission lines. However, because they are bulky and non-integrable with printed circuits, a new technique known as substrate integrated waveguide (SIW) has been invented [1]. The SIW technology [2–3] offers both advantages of printed circuits and conventional waveguides. In other words, the SIW can be called printed waveguides. The SIW is used in different types of microwave devices, especially filters. The high power handling, the low loss, and the low cost of fabrication consider the main benefits of the SIW. In the SIW, the substrate is sandwiched between two metallic layers. Also, the metallic layers are physically and electrically connected by using two rows of vias placed along the side ends of the SIW [4]. To reduce the size of the SIW structure, there are several proposed attempts, such as ridge SIW, by adding a row of vias in the center of the structure, offering a reduction ratio of about 40% [5,6]. The half-mode SIW (HMSIW) is produced by exploiting the symmetry of the magnetic wall of the structure. It is cut off the longitudinal center. The quarter-mode SIW (QMSIW) and the folded SIW are furthermore reported in the literature [7-13]. All these attempts have sought to reduce the overall size with keeping the same performance of the whole SIW as much as possible. However, filters utilizing these structures of the SIW operate over the cutoff frequency of the conventional SIW, considered as a drawback. To circumvent this problem, converting the evanescent modes to the propagating modes using metamaterial technology is used in a lot of research works [14-15]. The metamaterial is a technique allowing the SIW to work under the cutoff frequency [15], and it has been widely investigated due to its potential to miniaturize the RF circuits [16, 17]. The conventional transmission line is right-handed, but the metamaterial transmission line is left-handed. The evanescent-SIW combines both properties to be a composite right/left-handed (CRLH) transmission line (TL). The split ring resonator (SRR), and complementary split ring resonator (CSRR) are commonly used to develop the metamaterial for RF circuits [18- 20]. CSRRs are negative permittivity structures because they work as electric dipoles. Typically, the SIW structure sports under the cutoff frequency, negative permittivity for dominant mode TE10. Frequencies of the waves which are less than the cutoff frequency known as evanescent waves, cannot propagate. Hence, the waveguides will be non-useful under the cutoff frequency. There are two options to make the evanescent-mode become propagating mode. The first choice is to convert the negative permittivity into positive (i.e., both permittivity and permeability are positive), while the other is to provide negative permeability under cutoff frequency (i.e., double negative DNG metamaterials) [11]. To obtain miniaturization greater than 50%, it may be easily reached by enabling evanescent waves to travelling inside the SIW, so the devices working under the umbrella of this technique is called evanescent-mode. The half mode substrate integrated waveguide HM-SIW is generated by dividing the FM-SIW structure into two halves. Each segment can become a HM-SIW structure and it’s reflected the same propagation characteristics of FM-SIW. The HM-SIW structure has also been utilized extensively for the creation of microwave-circuits [21]. Moreover, the fabrication difficulty is maintained up to the exact degree as in the FM-SIW, and it also keeps the same benefits of low losses, small size and high Q-factor. Many filters have been created, [22, 23, and 24], particularly based on the HM-SIW since its release. Studies on HM-SIW demonstrate that an alternate structure of FM-SIW can lower the original width by around 50% while preserving equal cutoff frequency and propagation properties. The HM-SIW designs have been extensively employed for the building of filters as well as other microwave-circuits [25]. On other hand, the combination right/left-handed CRLH transmission line concept has been applied to both FM-SIW and HM-SIW structures to achieve a further reduced size by applying CRLH working under the cutoff frequency of both FM-SIW and HM-SIW [26]. Many microwave-circuit based on CRLH FM-SIW and CRLH HM-SIW have been successfully investigated [26]–[28].In this paper we will introduce the FM-SIW structure which works as a high pass filter at the cutoff frequency 5.2GHz and loaded upper layer by Hybrid I-H fractal slots to let it working under the cutoff frequency of the original design, then horizontally divide the overall structure to the half to achieve the HM-SIW bandpass filter using a metamaterial Hybrid I-H fractal slot with same cutoff frequency and the same advantages of the FM-SIW.

1.2 Literature review

This section reviews the most related research found in the literature, and they are summarized as follows:

- **In 2011,Vikram Sekar, and Kamran Entesari,**[29], Using cross-shaped fractal structures, we developed a new miniaturization technique to produce half-mode substrate integrated waveguide (HMSIW) bandpass filters, when the first and second iterations of the cross-shaped fractals are used, the total filter area is decreased by 28% and 37%, respectively, when compared to conventional HMSIW bandpass filters. This study introduces an innovative capacitive coupling method to make the filter compact, which results in better upper stopband rejection due to a transmission zero above the filter passband.
- **In 2012, Sougata Chatterjee, and Shantanu Das,** [30], a compact CRLH microstrip BPF has been proposed, where its size was reduced by six times than the conventional transmission lines. The obtained transmission and reflection coefficients were very good.

- I**n 2015, Juan de Dios Ruiz**,[31], the electromagnetic bandgap EBG technique was applied to the SIW and HMSIW BPFs which aids to reduce the overall size and enhance the performance.

  The Cauchy function was adopted to taper EBG to increase the matching, thereby enhancing the response. Nine of the tapered EBG Koch fractal slots were used.

In 2016, A. Coves, et al .[32], the step impedance resonator SIR and SIW were combined in one design in which the researchers sought to enhance the performance and reduce the size. The operating frequency was 4GHz, and the vias were empty without any conducting material inside them. This type of vias aids to decrease the effective permittivity, resulting in controlling the waveguide impedance.

In 2016, Qiao-Li Zhang,et al,[33] Proposed an electromagnetic bandgap (EBG)-loaded half-mode substrate integrated waveguide (HMSIW) and a composite right/left-handed (CRLH) HMSIW are used. The suggested filter works below the HMSIW's characteristic cutoff frequency. First, the CRLH HMSIW with EBG frameworks is investigated. The filter is then applied in a miniaturized form with two slots etched on HMSIW to minimize coupling effects between EBG structures and interdigital capacitors. To achieve ultra-wide out-of-band rejection, defective microstrip structure (DMS) input lines are used.

- **In 2018, Hayder S. Ahmed, et al.** [34], proposed and designed a filter operating with three bands, using the open square loop resonator. Then, the Minkawaski-like fractal shape (0^{th} to 2^{nd} iteration) was applied to each side of the resonator to reduce the overall size.

- **In 2018, Mostafa Danaeian, Hossein Ghayoumi-Zadeh,**[35] The unit-cell of fractal open complementary split-ring resonators (FOCSRRs) is used to create a tiny substrate integrated waveguide (SIW) bandpass filter. The suggested structure is achieved by engraving the proposed FOCSRR unit cells on the SIW structure's upper copper layer. The suggested filter's operation depends on evanescent-mode propagation. In the presence of appropriate stimulation, the suggested FOCSRRs act as an electric dipole, capable of yielding a forward-wave passband region below the waveguide structure's cutoff frequency.
- **In 2018, Feng Wei, et al.** [36], A half-mode substrate integrated waveguide (HMSIW)-based compact wideband bandpass filter (BPF) was suggested. It was accomplished by etching a pair of S-shaped complementary spiral resonators (S-CSRs) on the upper layer of the HMSIW cavity to achieve a broad passband as well as two transmission zeros in the region of the passband to increase selectivity.
-
- **In 2018, G. Vicent,et al**.,[37], proposed putting a periodic array of metallic cylinders along the waveguide to increase the permittivity in a SIW. A comprehensive investigation of the resultant effective permittivity as a function of cylinder diameter and separation between them.
- **In 2018, Dong-Fang Guan, et al,** [38], suggest a new slow-wave half-mode substrate integrated waveguide (HMSIW) construction with spoof surface plasmon polariton (SPP). To enable an SPP mode, subwavelength corrugated grooves are engraved on the top copper layer of HMSIW in this configuration. The suggested hybrid HMSIW-SPP structure's dispersion and propagation properties are investigated and compared to the conventional HMSIW.

- **In 2019, Sourav Moitra, et al.**[39], Design and analysis of a multi-mode HMSIW BPF. Transmission zeroes are introduced into the transmission pass band using reactive periodic slots. Several slot characteristics are investigated, and their impacts on stopband attenuations and transmission bandwidth. The given analysis achieves the goal of creating a flexible design and application-oriented output with calculated adjustments inside the resonant slots. The measured findings of the produced prototypes are in good agreement with the predicted values.
- **In 2019, Zied Troudi, Lotfi Osman**,[40], A novel compact HM-SIW C-band bandpass filter based on an elliptical CSRR-based irregular impedance method. Simply altering the Resonator settings and the electric cross-coupling controls the resonance frequency and transmission zeros.
- **In 2019, Ahmed Noura, et al,** [41], Using SIW technology in combination with DGS dumbbell cells, a unique and original design of HMSIW C-band band pass filter has been realized. The constructed HMSIW filter is 50% less in size than a comparable SIW filter, the measured insertion loss is roughly 2.6 dB, while the lower recorded return loss is less than 34 dB. Furthermore, good rejection is recorded outside of the filtering bands.

- **In 2020, Mostafa Danaeian**,[42], A dual band bandpass filter based on a SIW cavity that contained two mushroom resonators was proposed. The fundamental mode and next higher order mode of the resonators, TE101 and TE201, are excited to create the dual passbands. A second order direct coupled dual passband is obtained by loading two mushroom resonators adjacently to the SIW cavity. To activate the resonators via capacitive coupling, a microstrip feedline is used.

- **In 2020, Ayad M. Hamzah, Lukman Audah, and Nasr Alkhafaji,**[6], SIW metamaterial unit cells were produced and studied. Instead of CSRR inclusions, which were used in conventional SIW-metamaterial unit cells, fractal slots were etched across the upper walls of the SIW structures. The third iteration of the H-shaped fractal curve was chosen to produce more compact unit cells than previous fractal iterations.

- **In 2021, Yang-kun Han, et al.** [43], A compact dual-band dual-mode SIW balanced BPF with intrinsic CM suppression is proposed using a single perturbed circular cavity. The planar differential excitation structures are designed to excite the SIW cavity, while the CM noise cannot excite the SIW cavity.

- **In 2021, Yun Jiang, et al.**[44], A slow-wave defective ground structure (DGS) is placed on the top layer of a half-mode substrate integrated waveguide (HMSIW), and a compact wideband DGS-HMSIW filter with high harmonic suppression and low insertion loss (IL) is proposed.

- **In 2021, Hichem Boubakar, et al.**[45], In its first part, the authors introduced a novel SIW bandpass filter and HMSIW BPF loaded with complimentary hexagonal form metamaterial resonators for C-band applications. The HMSIW

BPF has a bandwidth ranging from 5.9 GHz to 6.5 GHz and is 50% less in size than a conventional SIW filter.

- **In 2021, Zied Troudi,et al**.[46], Using the stepped impedance approach, an unique miniaturized metamaterial unit cell is suggested. The suggested CSRR's electric dipole nature is used to produce a bandwidth below the SIW cutoff frequency. The tiny SIW bandpass filters are demonstrated by etching the CSRR on the metal cover of the SIW structure, which results in a downward frequency shift. To improve the size and performance of SIW filters, two configurations of the stepped impedance octagonal CSRR are proposed: reversely side-by-side and nested.

- **In 2021, Mostafa Danaeian**,[47], By loading the suggested DB metamaterial unit cell on the metal surface of the HMSIW structure, a novel compact DB BPF and three novel DB FPDs have been realized. The suggested configurations' working principle is based on the evanescent-mode approach. The DB metamaterial unit cell's electric dipole nature has been used to produce two forward passbands in a waveguide environment. These two passbands have been observed below the HMSIW structure's waveguide cut-off frequency. The measurement and simulation findings show that they agree well and exhibit the capability of the introduced devices in terms of compact size.

- **In 2022, Hichem Boubakar, et al.**[48], New miniaturized HMSIW bandpass filters are being developed and tested. The original ECSRR is fed into the first filter. This filter's simulation results are excellent. The second filter has the same structure and dimensions as the first, but it has an extra ECSRR put onto its bottom conductive layer. This extra ECSRR reduces the center frequency by approximately 300 MHz, implying further downsizing. Furthermore, it has improved the electromagnetic characteristics of the second filter over the first.
- **In 2022, Nabil Cherif, et al.**[49], A DGS SIW band-pass filter with a compact size and good stop-band rejection is presented. The bandpass filter's innovative design maintains stopband rejection from 3.8 to 6 GHz. When compared to conventional waveguide filters, this form of filter is easier to integrate with other planar circuits for practical applications. The measurement findings show that the filter is a good candidate for sub-mm applications.

- **In 2022, Nitin Muchhal, et al.**[50], A compact and wide-stop band half mode substrate integrated waveguide (HMSIW) filter with a hybrid fractal on the upper plane and a complementary split ring resonator (CSRR) along with a defected ground structure (DGS) etched on the bottom plane is proposed. A CSRR minimizes the resonant frequency, resulting in size miniaturization, by roughly 40% by increasing the CSRR's corresponding inductance and capacitance. Furthermore, the DGS's low-pass features assist in the suppression of out-of-band spurious harmonics.

1.3 Problem statement

1. Most filters have narrow bands especially ones using printed technology.
2. Most filters have large size especially ones using the waveguide.

1.4 Thesis aim

1. Using the SIW technology as a step to combine advantages of conventional waveguides and printed circuits in one structure to getting the first miniaturization step and overcome the narrow band issue in the printed circuits.

2. Adopting the metamaterial technology to make the structure operate under the cutoff frequency, by both options which are convert the evanescent mode to the propagation mode to achieve the backward propagation (which have negative permittivity and permeability) and the forward propagation (which have positive permittivity and permeability) to achieve the second miniaturization step.

3. Reducing the size of the conventional SIW into half by exploiting the magnetic wall of waveguides for a highly miniaturization ratio about 50% less than the conventional SIW.

1.5 Thesis organization

Chapter one will provides an overview of the study endeavor and the literature review in the same field.

Chapter two will introduces filter theory and the methods used to create typical microwave filters, substrate integrated waveguide the metamaterial using the fractal technique, where many types of fractals were discussed.

Chapter three will contains Hybrid I-H fractal iterations generation to design a FMSIW BPF using Hybrid I-H fractal slots, and extracting the parameters to prove to achieve metamaterial and miniaturization.

Chapter four will contain the design, fabrication, result extraction, and measuring of the parameters for the HMSIW BPF.

Chapter Five will be the conclusion of the results of simulation and measurements, and also the achievements to overcome the problems

CHAPTER TWO

THEORETICAL BACKGROUND AND LITERATURE SURVEY

2.1 Introduction

Most of today's RF/microwave applications operate in the frequency range of 300 kHz up to 300 GHz as shown in Figure 2.1. Communications, radar, navigation and radio astronomy are some of the applications that operate on different frequency bands within this frequency range. Hence, filters are needed to select, suppress, or combine RF/microwave signals within certain frequency bands for each application [51]. Low-pass, high-pass, bandpass and band-stop are the typical filter functions needed in any RF/microwave application. In the late 1930s, filter theory and practice started to develop, and the image parameter method of filter design was introduced [52]. This method was suitable for low-frequency filters which are mainly utilized in radio and telephony. The insertion loss method was introduced later, and most of today's microwave filter design is based on this method.

Recent technologies, such as wireless communication, challenge RF and microwave filter designers and researchers to design filters that perform better with compact size and low fabrication cost. Designing such a filter can be accomplished today because of recent advancement in new materials and fabrication technologies such as high-temperature superconductor (HTS), monolithic microwave integrated circuit (MMIC), and low-temperature co-fired ceramics (LTCC) [51]. Also, advances in computer-aided design

(CAD) tools complemented the above mentioned fabrication technologies to design filters with exceptional filtering characteristics.

The main objective of this thesis is to suggest a new approach in RF/microwave filter design, which can either provide size reduction while maintaining similar passband/stopband performance or improve filtering characteristics beyond what, can be achieved using classical filter design methods. In the following section, a review of basic concepts of filter design theory is presented.

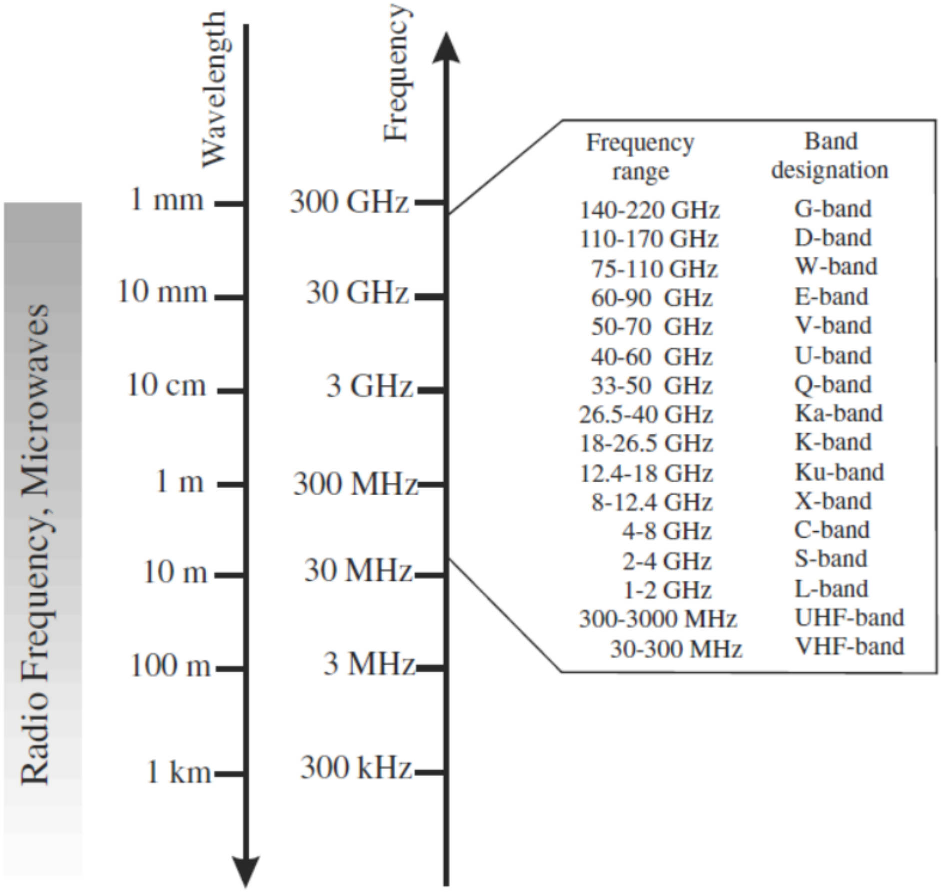

Figure 2.1 RF/microwave spectrums [51]

2.2 Filter design methods:

There are two well-known methods for classical filter design: image parameter and insertion loss [51]. Filters designed using the first method can provide the desired cut-off frequencies and attenuation characteristics by cascading simple two-port filter networks. The drawback of this method is that particular frequency response cannot be specified and an iterative process is needed to get the desired results. The second method, insertion loss, uses a network synthesis technique, which can completely specify the frequency response desired for the designed filter. In this method, the design process starts with LPF prototypes that are scaled to the appropriate impedance level and frequency [51]. Then, conversion of the prototype design is done using transformations to achieve the required frequency range and impedance level. However, microwave filters cannot be implemented directly using the above mentioned methods since both methods provide lumped-element circuits that are difficult to realize at high RF and microwave frequencies. Moreover, the range of values for available capacitors and inductors is limited and need to be estimated by distributed elements such as transmission lines. Approximation of lumped elements is done using transformations, such as Richard’s transformation and the Kuroda identities, which allow practical microwave filter implementation.

As stated in the previous section, only basic concepts of filter theory and design will be presented in this chapter, and interested readers can refer to [51, 53, and 54] for further detailed study of theoretical background about microwave filters.

2.3 S-Parameters

The scattering parameters of a network relates incident voltage waves to reflected voltage waves at any arbitrary ports. For an N port system, S parameters matrix contains N^2 elements, relating to the complex transmission and the reflection coefficients of the network. For a 2 port network, this means that scattering matrix contains four elements, which is shown below [52]:

$$S_{11} = \frac{b_1}{a_1}|_{a_2=0} , S_{12} = \frac{b_1}{a_2}|_{a_1=0} \tag{2.1}$$

$$S_{21} = \frac{b_2}{a_1}|_{a_2=0} , S_{22} = \frac{b_2}{a_2}|_{a_1=0} \tag{2.2}$$

S_{11} and S_{22} indicates the reflection coefficients of the network at ports 1 and 2 respectively, while S_{21} and S_{12} indicates the transmission coefficients in a similar fashion. Reflection coefficients, in this context, refer to the ratio of reflected voltage wave to the incident voltage wave at the same port. This is also the same for transmission coefficients, which refers to the ratio of incident voltage wave at one port, to the incident voltage wave at the other port.

In order to correctly determine the S parameters of a network, reflections at the ports other than the driven port should be eliminated. Therefore, it is assumed that all ports except the nth port of S_{mn} are terminated with loads that are matched to the network characteristic impedance. This way, the reflected voltage waves at these matched ports will be eliminated. In a 2 port system, for example, this will mean that for S_{m1} measurements, port 2 should be terminated with a matched load, thus reducing a2 to zero. Similarly, doing S_{m2} measurements requires that port 1 should be terminated with a matched load, thus, reflected voltage wave at port 1 (a1) disappears. As a general description, for an N port network, S_{mm} measurements require that all ports other than port m should be connected to matched loads. Similarly, S_{mn} measurements indicate that all ports except port m and n are terminated with matched loads.

The S parameters are complex variables and can be expressed in terms of amplitudes and phases as:

$$S_{mn} = |S_{mn}|e^{j\varphi mn} \quad m, n = 1{,}2 \tag{2.3}$$

Amplitudes of S parameters are defined in decibels (dB) as:

$$20\log|S_{mn}|dB \quad m, n = 1{,}2 \tag{2.4}$$

Two important parameters for filter design can be defined using S parameters. These parameters are: insertion loss (LA) and return loss (LR), which can be represented as:

$$L_A = -20\log|S_{mn}|dB \quad m, n = 1{,}2\ (m \neq n) \tag{2.5 a}$$

$$L_R = 20\log|S_{nn}|dB \quad n = 1{,}2 \tag{2.5 b}$$

The first parameter measures the amount of energy that is lost between port n and m and LR represents the return loss at port n. Signals transmitted through a filter experience some delay at the output, and there are two parameters, phase delay and group delay, which are related to this delay and can be defined as:

$$\tau_p = \frac{\varphi_{21}}{\omega}(\text{sec.}) \tag{2.6}$$

$$\tau_d = -\frac{d\varphi_{21}}{d\omega}(sec.) \tag{2.7}$$

τ_p: Phase delay, τ_d: Group delay

Port 1 is the input port and port 2 is the output port. Group delay is basically the delay of a packet of frequencies while phase delay considers the delay confronted by a single sinusoid.

Furthermore, it should be mentioned here that these parameters can be used in composite networks that contain many sub-networks and elements connected in series, parallel, or in cascade.

2.4 Filter response types

There are many transfer functions that may satisfy the attenuation and/or phase requirements of a particular filter. The one that you choose will depend on the particular system. The importance of the frequency domain response versus the time domain response must be determined. Also, both of these considerations might be traded off against filter complexity, and thereby cost.

2.4.1 Maximally flat

Also called Butterworth response or binomial, and it is the better response, where give a flat passband response for the filter order or complexity. Low pass filter LPF specified as below:

$$P_{LR} = 1 + k^2 (\frac{\omega}{\omega_c})^{2N} \tag{2.8}$$

Where N is refer to the order of filter and ω_c refer to the cutoff frequency. The passband extends from $\omega = 0$ to $\omega = \omega_c$; at the band edge the power loss ratio is $1 + k^2$. If we choose this as the −3 dB point, as is common, we have $k = 1$, which we will assume from now on. For $\omega >> \omega_c$, the attenuation increases monotonically with frequency. Like the binomial response for multi section quarter-wave matching transformers, the first (2N − 1) derivatives of Eq.(2.8) are zero at $\omega = 0$.

2.4.2 Equal ripple

If a Chebyshev polynomial is used to specify the insertion loss of an Nth-order low-pass filter as

$$P_{LR} = 1 + k^2 T_N^2 (\frac{\omega}{\omega_c}) \tag{2.9}$$

Then a sharper cutoff will result, although the passband response will have ripples of amplitude 1 + k2,k2 determines the passband ripple level. For large x, T_N (x)≈1/2 $(2x)^N$, so for $\omega >> \omega_c$ the insertion loss becomes

$$P_{LR} \cong \frac{k^2}{4} (\frac{2\omega}{\omega_c})^{2N} \tag{2.10}$$

Which also increases at the rate of 20N dB/decade. However, the insertion loss for the Chebyshev case is $(2^{2N})/4$ greater than the binomial response at any given frequency where $\omega >> \omega_c$.

The maximally flat and equal-ripple responses both have monotonically increasing attenuation in the stopband. In many applications it is adequate to specify a minimum stopband attenuation, in which case a better cutoff rate can be obtained. Such filters are called elliptic function filters, and they have equal-ripple responses in the passband as well as in the stopband. The maximum attenuation in the pass-band, Amax, can be specified, as well as the minimum attenuation in the stopband, Amin. Elliptic function filters are difficult to synthesize, so we will not consider them further.

2.4.3 Linear phase

This filters specify the amplitude response, but in some applications (such as multiplexing filters for communication systems) it is important to have a linear phase response in the passband to avoid signal distortion. Since a sharp-cutoff response is generally incompatible with a good phase response, the phase response of a filter must be deliberately synthesized, usually resulting in an inferior attenuation characteristic. A linear phase characteristic can be achieved with the following phase response:

$$\phi(\omega) = A_{\omega}[1 + P(\frac{\omega}{\omega_c})^{2N}] \tag{2.11}$$

where φ(ω) is the phase of the voltage transfer function of the filter, and p is a constant. A related quantity is the group delay, defined as

$$\tau_d = \frac{d\phi}{d\omega} = A[1 + P(2N+1)(\frac{\omega}{\omega_c})^{2N}] \tag{2.12}$$

which shows that the group delay for a linear phase filter is a maximally flat function[55].

The Figure (2.2) shows the comparison between the three filters' responses.

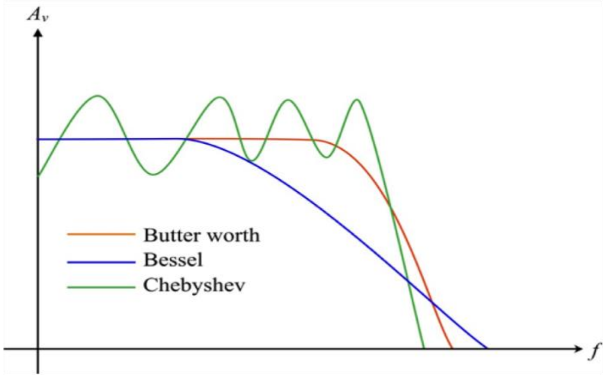

Figure 2.2: Comparison between Butterworth, Chebyshev, and Bessel filters.

A Butterworth filter has good transient behavior with fairly good amplitude, while the Chebyshev filters improve the amplitude response at the sacrifice of transient behavior. But the better transient response is optimized by the Bessel filter due to the linear phase in the pass band that means poorer frequency response.

2.5 Waveguide transmission line:

2.5.1 Rectangular waveguide

A rectangular waveguide is a type of structure which directs the propagation of the electromagnetic wave by confining the wave energy. It is normally composed of a hollow or dielectric-filled conducting metal pipe with a uniform cross section (see Figure 2.3). The rectangular waveguide was one of the earliest types of transmission lines that was used to transport microwave signals and is still being used today for a lot of applications [56]. A large variety of components such as filters, couplers, detectors and isolators are commercially available for various standard waveguide bands from 1 to 220 GHz. Nevertheless, because of the trend towards miniaturization and integration, most of the microwave circuits are currently fabricated by using planar transmission lines such as microstrip lines and straplines. However, there is still a need for waveguides in many applications, such as satellite systems, high-power systems and millimeter wave systems. The possible configuration of the electromagnetic fields that propagates in a rectangular waveguide can be obtained by solving Maxwell’s time-invariant field equations under the waveguide boundary condition [57]. There are two types of modes, namely, the transverse electric (TE) mode and transverse magnetic (TM) mode, can propagate in the waveguide. The TE and TM modes can be described in the form of TE_{mn} mode and TM_{mn} mode, where m and n represent the mode numbers. These two types of modes are independent of each other and the electromagnetic field in the waveguide can be expressed as their linear superposition.

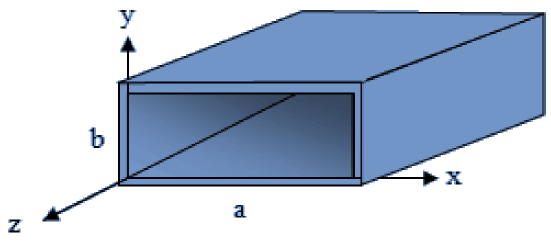

Figure 2.3 Configuration of the rectangular waveguide

2.5.2 SIW waveguide

The substrate integrated waveguide (SIW) is an integrated waveguide-like structure implemented on planar dielectric substrates with periodic rows of metallic vias connecting the top and bottom ground planes [58]. As shown in Figure 2.4, the top and bottom broad walls of the SIW are covered with metal ground, and a rectangular guide is created within a substrate by caging the structure with rows of metallic vias on either side.

The SIW is known to have similar guided wave and mode characteristics to conventional rectangular waveguide with equivalent guide wavelength. It also has the advantages of planar printed circuits, such as compact size, low cost, easy fabrication and integration with other circuits.

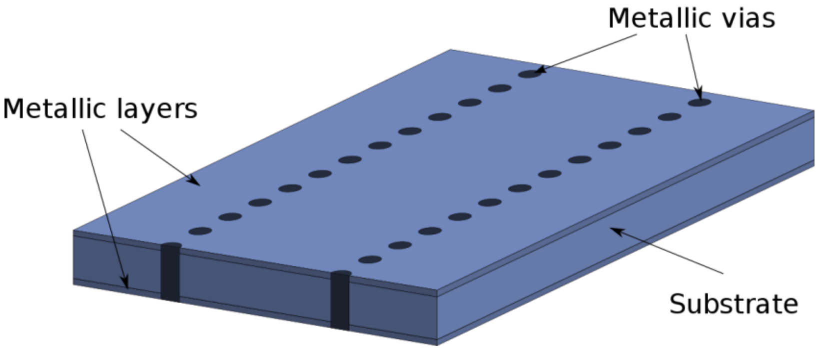

Figure 2.4 Configuration of the substrate integrated waveguide

The electromagnetic properties of the SIW have been studied in several papers [59-61]. It is shown that the guided wave properties of the SIW are similar to that of the corresponding conventional rectangular waveguide with a certain equivalent width. Therefore, the well-developed theory of waveguides can be applied to the design and analysis of SIW structures provided that the equivalent width of the SIW is given. Nonetheless, it should be noted that the differences between the SIW and the rectangular waveguide are also obvious. Since the SIW is a sort of periodic (or discrete) guided-wave structures, the propagation modes in the SIW are slightly different from those in normal waveguides, and there exists a certain type of leakage waves in SIWs due to the periodic gaps [59].

2.5.3 Supported Modes in the SIW

F. Xu and Ke Wu [59] have shown that the SIW exhibits similar guided wave properties to the canonical rectangular waveguide. Both of these two structures support the TE_{m0} modes, and the TE_{10} mode is the dominant mode. However, in terms of the TM and TE_{mn} (with $n \neq 0$) modes that exist in a conventional rectangular waveguide, they cannot propagate in the SIW due to the discontinuous structure of the SIW sidewalls [59]. Consequently, only TE_{m0} modes can exist in SIWs.

A clear physical explanation for the modes existing in the SIW has been given in [59] from the perspective of the surface current. As is known, when a mode is established in a guided-wave structure, the surface currents are then established. The SIW can be regarded as a special rectangular waveguide with a series of vertical slots on the sidewalls. When the slots cut along the direction of current flowing, i.e. TE_{n0} modes, only very little radiation will be yielded and thus these modes can be preserved in the waveguide. Figure 2.5 presents the flowing pattern of the TE_{10}-mode

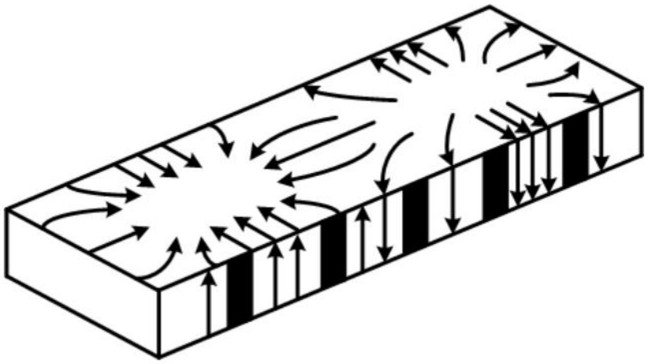

Figure 2.5 TE_{10}-mode surface current

Figure 2.5 The TE_{10}-mode surface current flowing pattern of a rectangular waveguide with slots on its sidewalls [59] surface current of a rectangular waveguide with slots on its sidewalls. It can be seen that the slots do not cut the surface current, and hence the TE_{10} mode can propagate along the waveguide. Similarly, other TE_{m0} modes can also propagate along the waveguide as they have similar surface currents on the narrow walls. However, when the surface current is longitudinal along the sidewalls of the waveguide, as is the case for TM and TE_{mn} (with $n \neq 0$) modes, the vertical slots will cut these currents and bring about a large amount of radiation out of the sidewalls. Consequently, the TM and TEmn (with $n \neq 0$) modes cannot propagate along the SIW and only TE_{m0} modes can exist in the SIW.

2.5.4 Effective Width of the SIW

SIW structure consisting of three layers, the mid layer is dielectric and covered from both sides by metallic layers, two rows of vias passing through these layers periodically, where connecting the upper and lower layers electrically which acting as an electrical side wall for the waveguide. [60, 61], as shown in Figure 2.4.

The cutoff frequency of the SIW has been investigated in [62]. It is shown that the cutoff frequencies of the TE_{10} and TE_{20} modes in the SIW with respect to the diameter of the metallized vias and the spacing between them can be expressed as follows in [62]:

$$f_{c(TE_{10})} = \frac{c_0}{2\sqrt{\varepsilon_r}}(a_{equ} - \frac{d^2}{0.95.b})^{-1} \tag{2.13}$$

$$f_{c(TE_{20})} = \frac{c_0}{\sqrt{\varepsilon_r}}(a_{equ} - \frac{d^2}{1.1.b} - \frac{d^3}{6.6.b})^{-1} \tag{2.14}$$

Where $\boldsymbol{c_0}$ is the speed of light in free space; a_{equ} is the width of the SIW, d is the via diameter and p is the via spacing as shown in Figure 2.6).

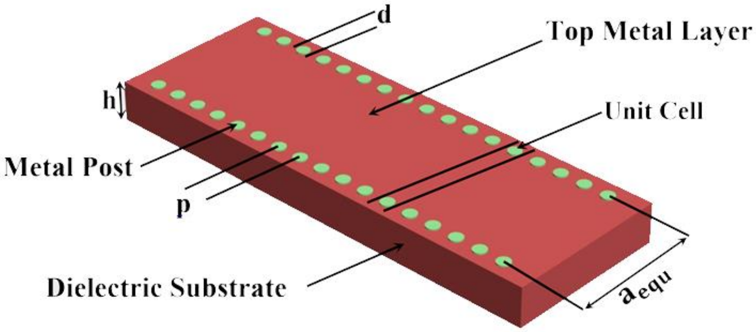

Figure 2.6 The SIW design structure derived from the conventional RWG

The SIW design structure derived from the conventional RWG, where the dielectric substrate of SIW acting as the dielectric which filled to the conventional wave guide [63, 64]. The effective variables are controlled on the required design showing in the figure below, ‘d’ is the via diameter, ‘p’ is the pitch between vias, ‘a’ is the distance between vias from side wall to the other side wall, and ‘h’ is the dielectric substrate thickness.

‘fc’ is the cutoff frequency, ‘c’ is the light velocity, and ‘εr’ is the permittivity of the substrate, the cutoff frequency can be found from equation (2.15) [65]

$$fc_c = \frac{c}{2a_{equ}\sqrt{\varepsilon r}} \tag{2.15}$$

The cutoff frequency resulted her is the same of the cutoff frequency of the conventional rectangular waveguide. The equation (2.15) can be writing in below form to calculate 'aeq':

$$a_{equ} = \frac{c}{2fc\sqrt{\varepsilon r}} \tag{2.16}$$

The diameter of vias 'd' and the pitch between vias should be chosen according to Equ.(2.17) to decrease the leakage losses in the SIW and be reliable physically [65]

$$d < p \tag{2.17}$$

By considering the limitation of fabrication, that is the time of manufacturing, possibility, and complexity of SIW fabrication are depends on the numbers of vias according to the below condition the number of vias shouldn't exceed 20% of wavelength [65].

$$0.05 < \frac{p}{\lambda c} < 0.25 \tag{2.18}$$

The distance between the vias center at the side rows 'a' can be found by Equ (2.19) [65]:

$$a = ae\text{q} + \frac{d^2}{0.95\text{p}} \tag{2.19}$$

2.5.5 Substrate Integrated Waveguide Transition

SIW transitions play an important role in integrating SIW components with other electronic devices. The design and implementation of transition structures between conventional rectangular waveguides and planar circuits have been widely studied [66-69]. Many of these structures can be adopted for the transition between SIW structures and planar circuits directly or with little modification, but with lower cost and more reliable fabrication process. Furthermore, since the SIW can be integrated with planar circuits on the same substrate, the whole circuit, including the planar circuit, transition and SIW structures, can be constructed in a dielectric substrate conveniently by just using a standard PCB processing technique [70].

The tapered microstrip transition [58] is one of the most commonly used structure for the transition between the microstrip line (MSL) and SIW. As illustrated in Figure 2.7, a microstrip line is connected directly to the top wall of the SIW through a tapered microstrip section; the vertical components of the electric field in both microstrip line and SIW regions are well matched and therefore the transition can be easily achieved. The tapered microstrip transition is a wideband structure that covers the complete useful bandwidth of the SIW. However, if a thicker substrate is used in SIWs in order to achieve a smaller conductor loss, the radiation loss will increase in the microstrip line as the substrate thickness is increased. Hence, the tapered microstrip transition is not suitable for active component integration, especially for those at mm-wave frequencies [71].

An alternative structure for the transition between planar circuits and SIWs is the coplanar waveguide (CPW). As shown in Figure 2.8, the CPW-SIW

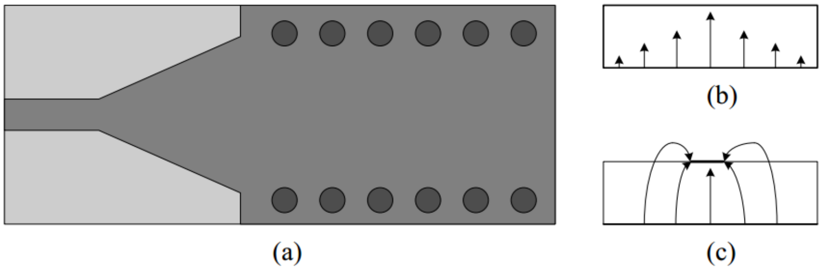

Figure 2.7 MSL to SIW transition with tapered microstrip feeding: (a) transition structure; (b) electric field distribution in SIW cross section, and (c) electric field distribution in MSL cross section

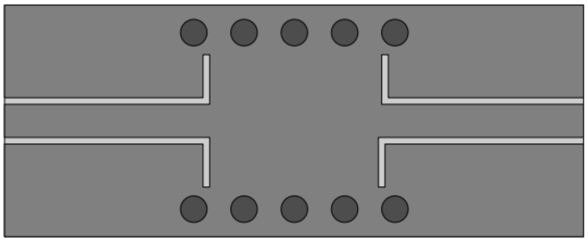

Figure 2.8 Configuration of the CPW-SIW transition [72]

A coplanar waveguide section to excite the SIW, with an inset stub employed to better match the CPW and SIW. Since increasing the height of the dielectric substrate might not have too much influence on the inherent characteristics of CPW, this transition is less sensitive to substrate thickness and hence exhibits a better performance than the microstrip transition in relatively high frequencies, especially in mm-wave frequencies.

2.5.6 Half-Mode Substrate Integrated Waveguide (HMSIW)

The configuration of the half-mode substrate integrated waveguide (HMSIW)[73] is shown in Figure 2.9. The structure of the HMSIW is similar to that of the SIW, but with the waveguide width half of conventional SIWs. The HMSIW was proposed based on the approximation of the vertical cut of the waveguide as a virtual magnetic wall [73]. The electric field of the main mode of a conventional SIW is maximum at the vertical center plane along the direction of propagation; therefore, this vertical plane can be viewed as an equivalent magnetic wall. Since half of the waveguide will keep the half field distribution unchanged if the cutting plane is a magnetic wall, the SIW can be bisected with this vertical center plane to achieve a more compact size, but with the main electromagnetic properties of the SIW unchanged. In fact, the open side aperture of the HMSIW is nearly equivalent to a perfect magnetic wall due to the high ratio of the waveguide width and height [73]. Consequently, the HMSIW is capable of achieving a size reduction of nearly 50% in comparison to conventional SIWs, while keeping the main properties of the SIW. The propagation properties of the HMSIW have been investigated in [74]. It is shown that only $TE_{p-0..5,\ 0}$ (p = 1, 2, ..…) modes can propagate in the HMSIW due to the large width-to-height ratio of the HMSIW and the discrete arrangement of metallic vias. The dominant mode in the HMSIW is the $TE_{0.5,0}$ mode. The electric field distribution of the $TE_{0.5,0}$ mode in the HMSIW is shown in Figure 2.9(c). It can be seen that the electric field distribution is similar to half of the fundamental TE_{10} mode in the conventional SIW. This is also why it is termed the half-mode SIW.

The cutoff frequency of the main mode of the HMSIW ($TE_{0.5,0}$ mode) can be calculated by [74]:

$$f_{c(TE_{0.5,0})} = \frac{c_0}{4\sqrt{\varepsilon_r w_{eff\_HMSIW}}} \tag{2.20}$$

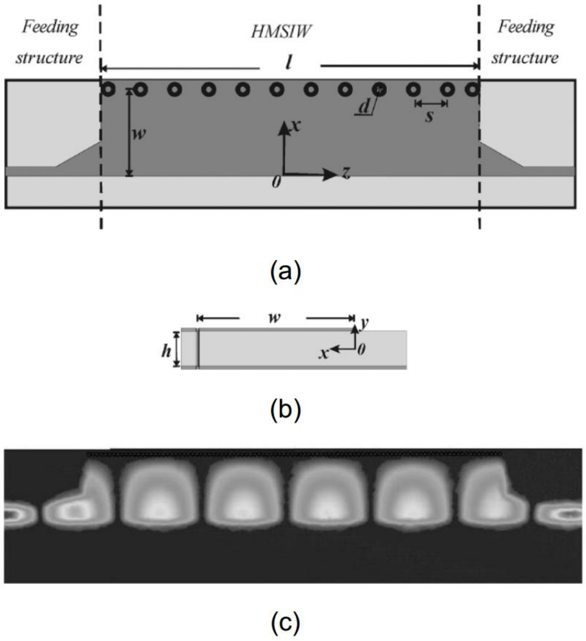

Figure 2.9 (a) Top view of the configuration of the HMSIW. Dark grey shading represents metallization. (b) Side view of the configuration of the HMSIW. (c) Electric field distribution of the $TE_{0.5,0}$ mode in the HMSIW [74]

where w_{eff_HMSIW} represents the equivalent width of the HMSIW, which can be expressed as:

$$w_{eff_{HMSIW}} = \dot{w}_{eff_{HMSIW}} + \Delta w \tag{2.21 a}$$

$$\dot{w}_{eff_{HMSIW}} = w - 0.54\frac{d^2}{p} + 0.05\frac{d^2}{2w} \tag{2.21 b}$$

$$\frac{\Delta w}{h} = \left(0.05 + \frac{0.3}{\varepsilon_r}\right).\ln(0.79\frac{\dot{w}^2_{eff_{HMSIW}}}{h^2} + \frac{104\dot{w}_{eff_{HMSIW}} - 261}{h^2} + \frac{38}{h} + 2.77) \tag{2.21 c}$$

where w is the width of the HMSIW, h is the height of the HMSIW, d is the via diameter, and p is the via spacing.

For the first high mode $TE_{1.5,0}$ mode, the cutoff frequency can be approximated as:

$$f_{c(TE_{0.5,0})} = \frac{3c_0}{4\sqrt{\varepsilon_r w_{eff\_HMSIW}}} \tag{2.22}$$

From equations (2.20)-(2.22), it can be seen that the cutoff frequency of the first higher mode is three times that of the fundamental mode in the HMSIW. Therefore, if not considering the suppression of the high modes, a HMSIW with a width w has a single-mode operation frequency range approximately twice that of a SIW with a width 2w [74].

As described above, the electric field distribution of the main mode of the HMSIW is similar to half of the fundamental TE10 mode in conventional SIWs [74]. Since the ridge SIW is capable of achieving a more compact size in comparison to conventional SIWs by loading the SIW with a ridge, it may be possible to load the HMSIW with a Hybrid I-H fractal to achieve a further size reduction, while keeping the main advantages of the HMSIW. This solution to reduce the size of HMSIWs will further be studied in detail in Chapter 4.

2.6 Metamaterials

2.6.1 History of Metamaterials and Left-Handed Metamaterials

Electromagnetic metamaterials (MTM) are artificial electromagnetic structures with special properties that cannot be found in nature [75]. The structural cell size p should be at least smaller than a quarter of guided wavelength λg to meet the effective homogeneity condition as shown in Figure 2.10.

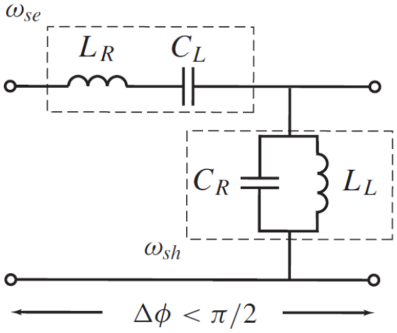

Figure 2.10 MTM transmission line unit cell.

This condition ensures refraction dominates over scattering or diffraction for reliable wave propagation inside the MTM media. When this condition is met, the structure can be seen as a material with constitutive parameters of electric permittivity ε and permeability μ, where it is electromagnetically uniform along the direction of propagation [76]. The refractive index n can be defined in terms of the constitutive parameters ε and μ as[75]:

$$n = \pm\sqrt{\varepsilon_r \mu_r} \tag{2.23}$$

Where ε_r and μ_r are the relative permittivity and permeability respectively, which are associated with free space permittivity and permeability by $\varepsilon_0 = \frac{\varepsilon}{\varepsilon r} = 8.854 \times 10^{-12}$ (F/m) and $\mu_o = \frac{\mu}{\mu r}$ = $4\pi \times 10^{-7}$ (H/m). It can be concluded from (2.23) that the sign for (ε, μ) can be (+,+), (+,-), (-,+) and (-,-) as shown in Figure 2.11. The first quadrant of ε- μ diagram corresponds to the conventional right-handed material with forward wave propagation. When either ε or μ is less than zero, the wave cannot propagate because the negative sign for either ε or μ results in an imaginary propagation constant ($\beta = nk_0$ (rad/m) where $n = \pm\sqrt{\varepsilon_r \mu_r}$, $k_0 = \omega\sqrt{\varepsilon_0}$) and stopband can be observed [77]. The fourth quadrant in Figure 2.11 represents left-handed (LH) material where $\varepsilon = \varepsilon_r \varepsilon_0$ and $\mu = \mu_r \mu_o$ are simultaneously negative. Such materials can be identified by antiparallel phase and group velocities because of their double negative parameters [75].

In 1967, Viktor Veselago predicted the existence of LH MTM that allows backward wave propagation [78]. This prediction was confirmed three decades later by Smith [79], where he proposed a structure consisting of a periodic array of split ring resonators and continuous thin wires shown in Figure 2.12 that allow wave propagation at a certain frequency region with negative- ε and negative-μ.

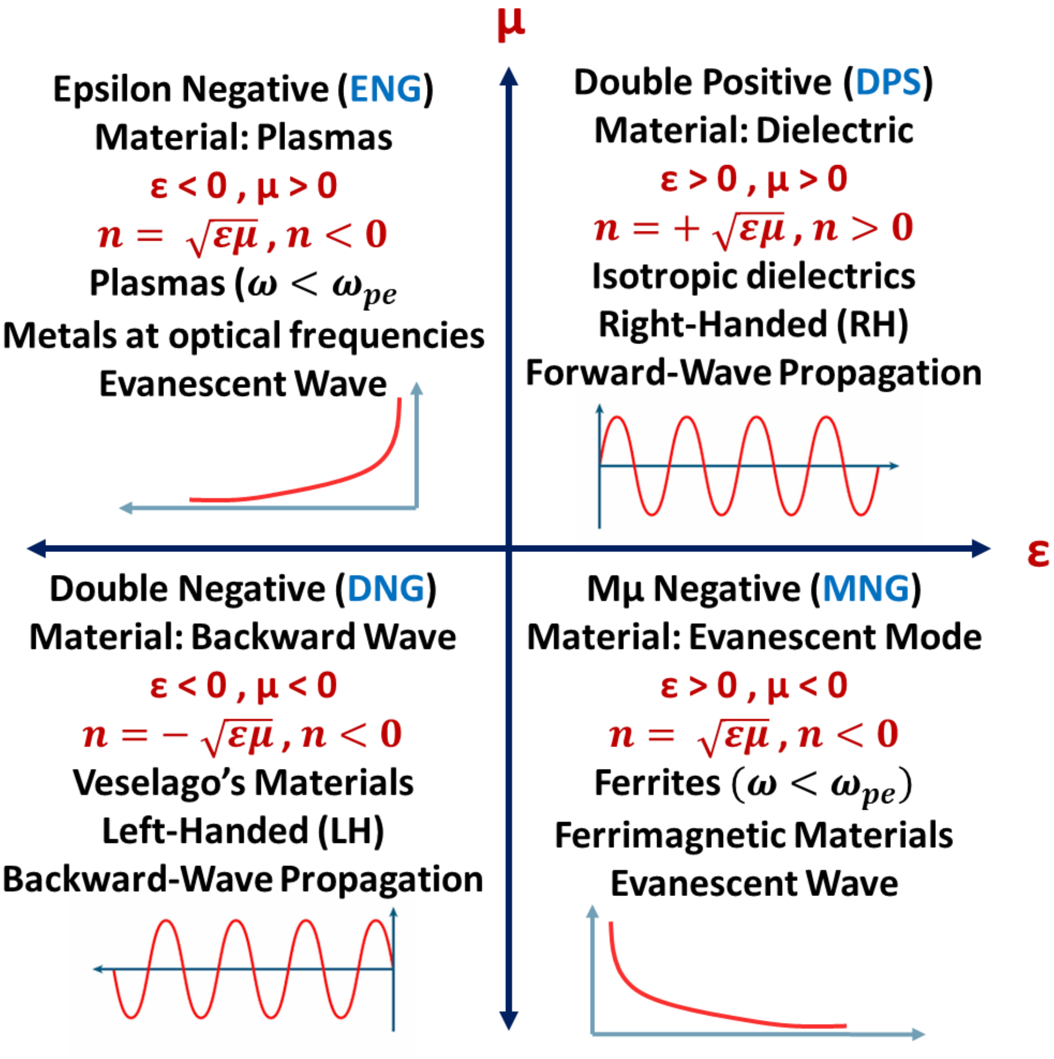

Figure 2.11 Permittivity-permeability (ε- μ) diagram where the sign of refractive index (n) is controlled by ε and μ [75].

After Smith's breakthrough, the thesis on LH MTM continued and different theoretical and experimental approaches were used to verify the backward wave propagation in LH MTM. The LH structure presented in Figure 2.11 was inspired by Pendry's work in [80, 81] and can be considered as a resonant type structure that suffers from high loss and exhibits narrow bandwidth. Therefore, transmission line approach of MTM was presented by Caloz in [82, 83] to solve the problems of the resonant type structure presented by

Smith. In the next section, it will be shown that TL approach of MTM is preferred since classical TL theory can be used to design and analyze LH MTM.

2.6.2 Transmission Line Approach

The main characteristic of the LH TL is the antiparallel phase and group velocities, which can be easily verified when considering the incremental circuit model for a lossless LH TL shown in Figure 2.12.

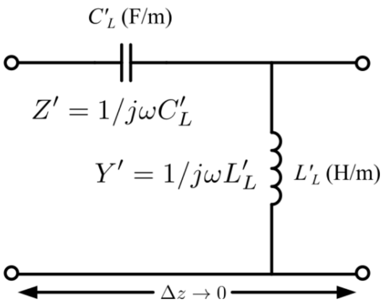

Figure 2.12 The “incremental circuit model for a hypothetical uniform LH TL” [75]

The complex propagation constant γ, for the above lossless transmission line is given by [75]

$$\gamma = j\beta = \sqrt{Z'Y'} = \frac{1}{j\omega\sqrt{L'_L C'_L}} = -j\frac{1}{\omega\sqrt{L'_L C'_L}} \tag{2.24}$$

where β is the propagation constant and the phase and group velocities can be expressed as:

$$v_p = \frac{\omega}{\beta} = -\omega^2\sqrt{L'_L C'_L} \tag{2.25}$$

$$v_g = (\frac{\partial\beta}{\partial\omega})^{-1} = +\omega^2\sqrt{L'_L C'_L} \tag{2.26}$$

It can be concluded from the above equations that phase propagation (β) is in the opposite direction of the power flow, which proves the TL of Figure 2.11 is LH. For practical design of LH TL, the average cell size p should be much smaller than the guided wavelength λ_g. Satisfying such condition, allows the realization of LH medium in a certain frequency range. The first microstrip LH TL structure was presented by Caloz et al. in [84], which consisted of a series interdigital capacitor and short-circuited shunt stub inductors. One of the main benefits of TL MTM is that it can achieve low loss by designing a balanced structure and minimizing the mismatch between the input and output ports. Also, broad bandwidth can be attained by adjusting the TL constitutive LC parameters. Moreover, Integration with other passive and active RF/microwave components is easy since TL MTM structures can be realized in planar configuration.

2.6.3 Ideal Composite Right/Left-Handed (CRLH) TL

The series capacitor CL and shunt inductor LL are needed to realize a LH TL as shown in Figure 2.11, but wave propagation through the structure introduces series inductance and shunt capacitance parasitic effect. Magnetic flux can be induced when the current flows along the series capacitor CL, which resembles the existence of a series inductor LR. Also, a shunt capacitor CR is present due to the existence of voltage gradient, i.e. electric field E, between upper conductors and ground [75]. Since the contribution of right-handed (RH) conventional TL elements LR and CR cannot be disregarded, it is impossible to realize a purely LH (PLH) TL structure, and the term composite right/left-handed (CRLH) is a general term used to describe LH structure.

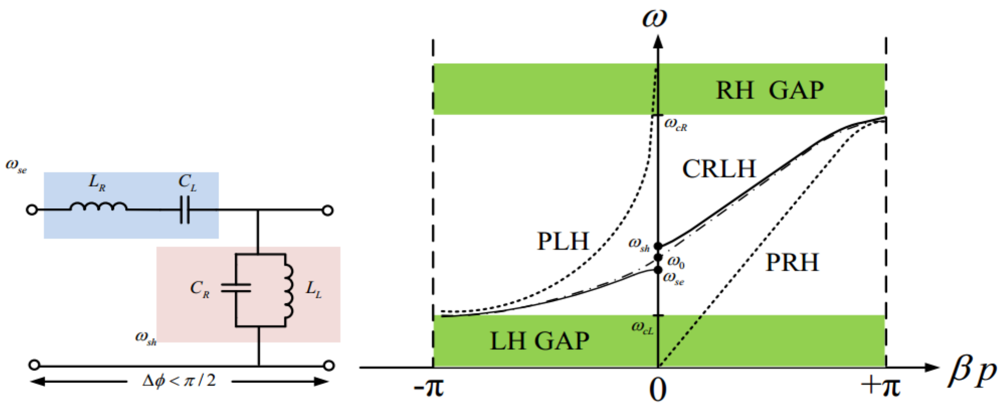

Figure 2.13 Characteristics of CRLH TL. (a) Circuit model for unit cell TL. (b) Dispersion diagram for CRLH, PLH, PRH structures [75].

CRLH TL structure can be studied using the equivalent circuit model in Figure 2.13(a). At low frequencies, series inductance LR and shunt capacitance C_R can be interpreted as short and open circuit respectively. So the remaining series capacitance C_L and shunt inductance L_L can be regarded as a high-pass filter with a cut-off frequency ($= 1/\sqrt{L_L C_L}$, (rad.m)/s). At high frequencies, only the RH elements (L_R, C_R) are taken into account in the equivalent circuit since LH elements (C_L, L_L) can be considered as short and open circuit respectively. Therefore, the resulting circuit acts as low-pass filter with cut-off frequency ($\omega C_R = 1/\sqrt{L_R C_R}$, (rad.m)/s) where only RH elements are considered (L_R, C_R). The transmission characteristics of CRLH TL are determined by considering the effects of RH and LH elements at all other frequencies. Therefore, CRLH TL has bandpass response due to the existence of RH and LH elements.

From the dispersion diagram for CRLH TL in Figure 2.13(b), it can be seen that attenuation occurs at a certain range of frequencies within the passband when shunt resonance ($\omega_{sh} = 1/\sqrt{L_L C_R}$) and series resonance ($\omega_{se} = 1/\sqrt{L_R C_L}$) are different, which refers to the case of unbalanced CRLH TL. On the other hand, when the transition frequency $\omega_0 = \omega_{se} = \omega_{sh}$, balanced CRLH TL can be realized and an infinite wavelength ($\lambda_g = 2\pi/|\beta|$) is attained at ω_0 [75]. The cases for balanced and unbalanced CRLH TL are discussed in the following section.

2.6.3.1 Balanced and Unbalanced CRLH TLs

The properties of balanced and unbalanced resonance observed in CRLH TL are both useful in filter design. For example, ultra-wide bandpass filter (BPF) can be constructed using one unit cell of balanced CRLH TL [85] where dual-band BPF can be realized using the unbalanced case [86]. Both cases can be examined by considering the characteristic impedance Z_c of the CRLH TL unit cell defined as [75]:

$$Z_c = Z_L\sqrt{\frac{(\omega/\omega_{se})^2-1}{(\omega/\omega_{sh})^2-1}} \tag{2.27}$$

$$\begin{cases} Z_c[0 < \omega < \min(\omega_{se}, \omega_{sh})] \in R(LH\ pass\ band). \\ Z_c[\min(\omega_{se}, \omega_{sh})] \in/(gap\ for\ unbalanced\ case). \\ Z_c[\omega > \max(\omega_{se}, \omega_{sh})] \in R(RH\ pass\ band). \end{cases} \tag{2.28}$$

where $Z_L = \sqrt{L_L/C_L}$ is the impedance of purely LH TL. It can be seen from (2.27) when $\omega = \omega_{se}$ or $\omega = \omega_{sh}$, a zero and a pole will be introduced in the characteristic impedance which results in a zero group velocity or stopband. Unbalanced CRLH TL can be only matched in a certain frequency range since Z_c is a function of frequency, whereas balanced CRLH TL can be matched over an infinite frequency band because Z_c ideally becomes frequency independent when ($\omega_{se} = \omega_{sh}$). Moreover, propagation constant of PRH and PLH TL can be added to obtain the propagation constant of balanced CRLH TL.

Non-zero group velocity at the transition frequency ω_0 is one of the remarkable properties of a balanced CRLH TL. Propagation is supported at this frequency while propagation constant $\beta = 0$. Hence, phase origin is defined at ω_0. This can be easily understood by calculating the phase shift along the TL with physical length l, i.e. $\emptyset = -\beta l = 0$. Phase behavior in CRLH TL is different than conventional RH TL. Below ω_0, phase shift is positive and reaches positive ∞ as frequency approaches zero: $\emptyset\ (\omega \to 0) = -\beta d \to +\omega_{CL}.(l/\omega)$. In the other hand, phase becomes negative as frequency increases above ω_0 and reaches negative ∞ at very high frequencies: $\emptyset\ (\omega \to \infty) = -\beta d \to -\omega.(l/\omega_{CR})$ [75]. Guided wavelength shows different behavior in CRLH TLs when compared to RH TLs. As shown earlier, $\lambda_g = \infty$ at ω_0 and it becomes smaller at frequencies ($\omega < \omega_0$) or ($\omega > \omega_0$).

2.6.3.2 LC Network Implementation

Ladder networks consisting of LC unit cells can be used to realize CRLH TL since it's not readily available in nature. These networks are operative in a restricted frequency range as long as effective homogeneity condition is met. The operational frequency range or bandwidth for these networks can be easily controlled by the LC parameter values. It worth mentioning here that bandwidth obtained using TL approach of MTM is larger than that of resonant approach mentioned before (i.e. TW-SRR)[75]. Hence, appropriate number of LC unit cells N is repeated to obtain a TL with total length of l as shown in Figure 2.14. Assuming the structural average cell size p is very small, ideal CRLH TL can be represented by NLC unit cells to ensure homogeneity condition. This condition is needed to avoid resonance along the discontinuities of the lines. Although, CRLH TL is generally implemented in periodic configuration due to its design simplicity, non-periodic implementation of CRLH TL unit cell exist [87]. Additional degree of freedom is usually associated with non-periodic structure at the expense of higher design complexity.

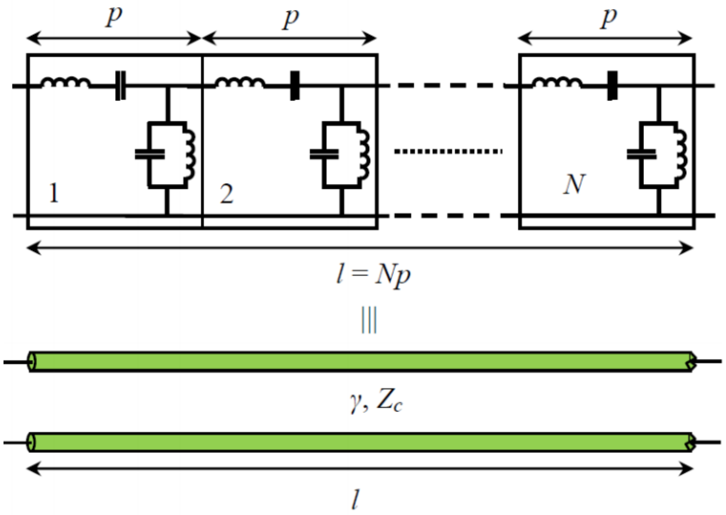

Figure 2.14 Equivalent periodic LC network for an ideal TL with length l assuming effective homogeneity condition; $\boldsymbol{p} = \Delta \boldsymbol{z} \rightarrow \mathbf{0}$.

2.6.3.3 Comparison between conventional bandpass filters and CRLH TLs

Filtering characteristic obtained by the use of CRLH TLs is quite similar to conventional bandpass filters. One important characteristic of filters is the sharp roll-off rate which can be attained by increasing the filter order in conventional filter. Similarly, increasing number of unit cells in CRLH TL has similar effect [75]. However, major differences between these two are obtained when studied thoroughly [75]. These distinctions are mentioned below:

- Homogeneity condition (i.e. $\Delta_z << \lambda_g$) is not satisfied in conventional filters, whereas unit cell of CRLH TL must satisfy this condition.
- Conventional filters can be realized only as a 1D structure, while CRLH TL based structures can be 2D or 3D and behave as a bulk media.
- Conventional filters are mainly designed according to magnitude specifications, whereas LH structures are generally designed to meet certain phase specifications. Thus, RH and LH transmission can be only observed in LH structure.
- Finally, identical unit cells are usually employed in LH structures while each unit-cell in conventional filters has a different LC value to meet certain design specifications.

2.7 Fractal Geometry

2.7.1 What is Fractal ?

Fractal geometry first appeared at the end of the nineteenth century when Peano created a continuous curve traversing every point in a given area [105]. Fractal curves were produced by repeating a single shape in an iterative way. It can be thought of as a collection of scaled imitations of the original form. After each iteration, more orders of the fractal curves are acquired, and these new orders have longer curves than the produced in the previous iterations to completely fill the specified region. For high miniaturization in MW elements, using feature of space filling of fractal curves due to it is can be achieved theoretically by filling the small spaces with lines have an infinity length. Printing a very long microstrip line on a small area of substrate lead to produce a compact designs of antenna, resonator, and filters. The fractal geometry also used in multi band and small designs for a different applications such as left handed metamaterials (LHMs) [106], frequency selective surfaces FSSs [107], high impedances surfaces HISs [108], and RF identifications [109]. The geometry that describes the irregular structures having a fractional dimensions (dimensions where not whole numbers) [91]. These structures could not be described by Euclidean Geometry this geometry has a fixed number of dimensions (1D, 2D, 3D) [90]. There are many natural shapes around us have complicated geometric shapes (fractal) such as ferns, length of coastline, snowflakes, mountains, branching of trees, density of clouds, etc.. Fractal shapes shown in Figure (2.15). Mathematically, fractal can be represented by complex numbers. These numbers are plotted on a plane [92, 93]

Figure (2.15): Natural shape of fractals.

2.7.2 Fractal Shape Characteristics

Fractal can be defined as a set (F) has some characteristics expressed below [90,94].

2.7.2.1 Fractal set is self – similar

An object is said to be self-similar when it is entirely constructed by many copies of itself at different scales, i.e. the shape of the object repeated itself through successive magnifications, as shown in Figure (2.16).

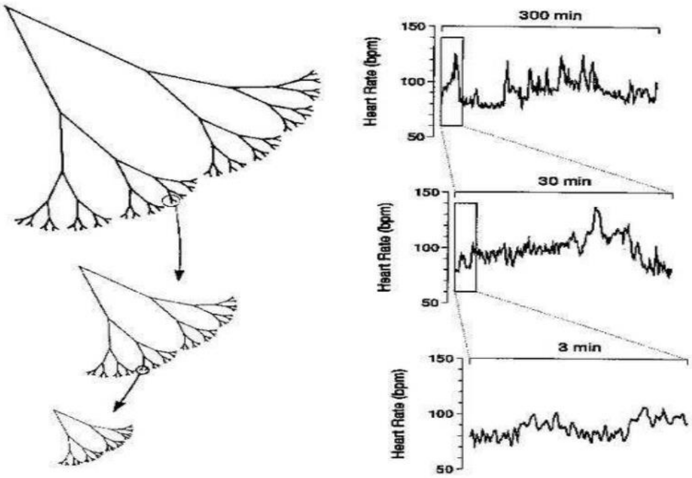

(a) (b)

Figure (2.16): (a) self-similarity structure (b) self-similarity dynamics.

All fractals show self-similarity character, but there are different degrees of self-similarity. They can be classified into three types according to their self-similarity [95].

2.7.2.1.1 Exact self-similarity: Fractals are exactly self-similar when every small part is structurally similar to the larger part under any magnification, also these parts reduce by a scale factor.

2.7.2.1.2 Quasi-self-similarity: Fractals exhibit less self-similar than the first type. They are approximately similar under any magnification. Small parts of a quasi-self-similar fractal are not completely such as the whole fractal structures.

2.7.2.1.3 Statistical self-similarity: Fractals have the weakest self-similarity. Their magnified small parts look statistically similar to the whole fractal but in detail they are different.

2.7.2.2 Fractal set has a fine structure

Fractal set contains details at small scales. The property of fine structure can be visualized by the coastline example. This is shown in Figure (2.17).

Figure (2.17): Britain coastline.

The ruler that is used to measure the length of the coastline is represented by red line. If we measure this coastline with a ruler of length one kilometer, we will obtain a certain length of coastline. If we decrease the length of this ruler then the length of the coastline will be increased. We will get a different lengths because of the small details that smaller ruler can get it. If we decrease the ruler length once again, we could get into the smallest details and crannies, and the measurement of the coastline will be greater. One could even measure it with infinitesimally short rulers, and the coastline would be infinitely long, that is a fractal [88, 90].

2.7.2.3 Fractal dimension

Before we explain the fractal dimension concept, it is better to have some information about the dimension measurement in Euclidean space. In this space all objects have integer dimensions usually called Topological dimension. For example, a point has a zero topological dimension. If we have infinitely neighboring points in one dimension, they are represented as a line. Plane has a two line in two different dimensions, and so on a cube has a three line in three different dimensions. This is shown in the Figure (2.18) [90].

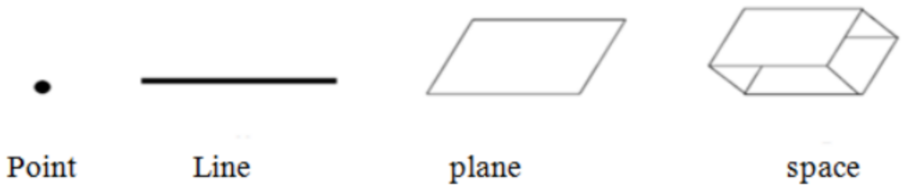

Figure (2.18) Topological dimensions.

Now, if we divide this topological dimension into self-similar sub-dimension, and l will be a magnification factor in each spatial dimension. This is shown in the Figure (2.19).

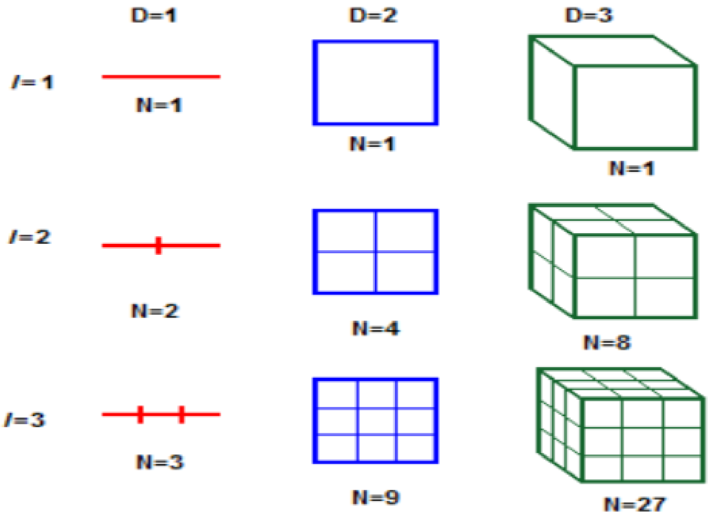

Figure (2.19): Topological sub-dimension

We can calculate the number of self-similar objects (N) by the relation:

$$N = \ell^{D_f} \tag{2.29}$$

Where, D_f is the fractal dimension and can be defined by the relation [94]:

$$D_f = \frac{\log(no.of\ self\ similar\ objects)}{\log(magnification\ factor)} = \frac{\log N}{\log \ell} = \frac{\log \ell^{D}}{\log \ell} \tag{2.30}$$

If we apply the previous relation on the line, plane, and cube, we will get the dimensions 1 , 2 , 3 respectively .

The relation (2.30) is applied to determine the fractal dimension D_f [96]. Previously, we have talked about the fractal as a non-integer number, so its value lies between zero and first or first and second dimension.

2.7.3 Fractal Shape Generation

There are multiple processes in mathematics used to generate the fractal shapes and plotted in the space, such as, Escape-time fractal, Random fractals, and strange attractors [95, 97, and 98]. For geometric (exactly self-similar) shape, the iterated function systems are used.

2.7.3.1 Iterated Function Systems (IFS)

One of the most popular techniques that used to create fractal shapes (especially the self-similar ones), because they have a fixed geometric replacement rule [95]. In this method, fractals can be generated by transforming segments of a data set to the smaller segments that have self-similarity. The iterative function consist of self-affine transformations that takes the form [99]:

$$w = \begin{pmatrix} x \\ y \end{pmatrix} = \begin{pmatrix} a & b \\ c & d \end{pmatrix} \begin{pmatrix} x \\ y \end{pmatrix} + \begin{pmatrix} e \\ f \end{pmatrix} \tag{2.31}$$

The affine transformation, w, is represented by six parameters: a, b, c, d, e, and f. These parameters are responsible for movement of fractal element in space, (a, d) for scaling, (b, c) for rotation by φ1 , φ2 angles with respect to axis of coordinate system, and (e, f) are the control linear translation, as shown in Figure (2.20) [100,101].

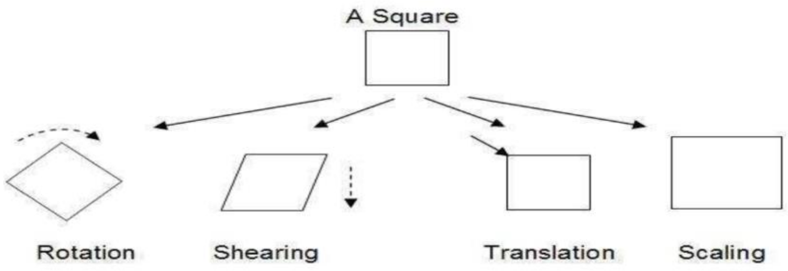

Figure (2.20): The affine transforms.

2.7.4 Geometric Fractal Shapes

This section introduced some fractal structures that used in antenna and metamaterial models. Generally, the geometric (or Deterministic) fractals are creating by (IFS), some of the most commonly fractal shapes used, such as Hilbert curve, Sierpinski gasket, Sierpinski carpet, Koch snowflake, Peano curve, etc. [95,102]. These fractals contain multi scale down and rotated copies of itself and they are exactly self-similar. The generation process of all shapes, starts with an initiator and generator [100].

2.7.4.1 Koch Curve Generation Process

Fractal Koch shape generating process is a straight line that has broken into three pieces of equal sizes. The middle segment is removed and replaced by two segments equal in size to the removed one, these segments are fit into the gap in a form of triangle. Koch curve shown in Figure (2.21) [103,102].

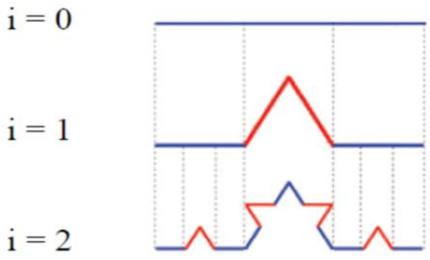

Figure (2.21): Koch curve generation [101].

This fractal shape has a dimension equal to (1.26), the iterated function of Koch curve 1st , 2nd , and 3rditerations given by [101,102]:

$$W_1(x,y) = \left[\frac{1}{3}x; \frac{1}{3}y\right] \tag{2.32}$$

$$W_2(x,y) = \left[\frac{1}{6}x - \frac{\sqrt{3}}{6}y + \frac{1}{3}; \frac{\sqrt{3}}{6}x + \frac{1}{6}y\right] \tag{2.33}$$

$$W_3(x,y) = \left[\frac{1}{6}x + \frac{\sqrt{3}}{6}y + \frac{1}{2}; -\frac{\sqrt{3}}{6}x + \frac{1}{6}y + \frac{\sqrt{3}}{6}\right] \tag{2.34}$$

2.7.4.2 Hilbert Curve Generation Process

Hilbert curve was first introduced in (1862-1943). This curve is called a space-filling curve, because it will fill the whole plane after multiple iterations [102], as shown in the Figure (2.22).

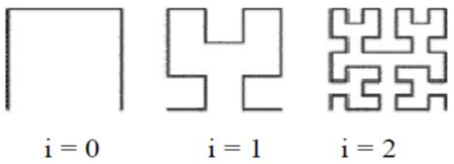

Figure (2.22): Hilbert curve generation steps [101].

In Hilbert curve generating process, each successive step consists of four copies of the previous step, connected with additional line segments [89]. Fractal dimension equal to (1.2619), the iterated function of Hilbert curve 1st , 2nd, and 3rd iterations will be [101,102]:

$$W_1(x,y) = \left[\frac{1}{2}y - \frac{1}{2}; -\frac{1}{2}x - \frac{1}{2}\right] \tag{2.35}$$

$$W_2(x,y) = \left[\frac{1}{2}x - \frac{1}{2}; \frac{1}{2}y + \frac{1}{2}\right] \tag{2.36}$$

$$W_3(x,y) = \left[\frac{1}{2}x + \frac{1}{2}; \frac{1}{2}y + \frac{1}{2}\right] \tag{2.37}$$

2.7.4.3 Sierpinski Gasket Generation Process

The Sierpinski gasket or Sierpinski triangle was first introduced by the Polish mathematician Sierpinski in 1916 [103]. It is one of the most common fractal geometries, It is created by starting with equilateral triangle and removing a central equilateral triangle leaving three halvestriangles. Then repeating this process to infinity, the remaining form has infinite lines but it is less than a plane [93,102]. This is shown in the Figure (2.23).

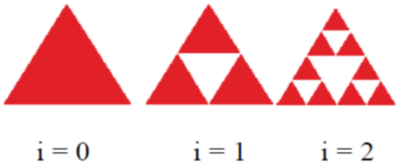

Figure (2.23): Sierpinski gasket generation [101].

Fractal dimension of Sierpinski gasket is (1.5849), the iterated function for Sierpinski gasket 1st, 2nd, and 3rd iterations given by [101,102]:

$$W_1(x, y) = \left[\frac{1}{2}x; \frac{1}{2}y\right] \tag{2.38}$$

$$W_2(x, y) = \left[\frac{1}{2}x + \frac{1}{2}; \frac{1}{2}y\right] \tag{2.39}$$

$$W_3(x, y) = \left[\frac{1}{2}x + \frac{1}{4}; \frac{1}{2}y + \frac{\sqrt{3}}{4}\right] \tag{2.40}$$

2.7.4.4 Sierpinski Carpet Generation Process

Sierpinski carpet is a fractal shape introduced by Wacław Sierpiński in 1916. Its generation procedure is similar to that of the gasket. The initiator here is square and then generated by removing the middle square. Middle square is one-third the original one [93], as shown in Figure (2.24).

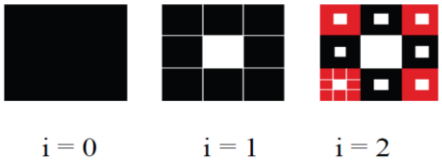

Figure (2.24): Sierpinski carpet generation [101].

Fractal dimension of Sierpinski carpet is (1.8927), and the iterated functions of first three iterations can be expressed as below [101]:

$$W_1(x,y) = \left[\frac{1}{3}x; \frac{1}{3}y\right] \tag{2.41}$$

$$W_2(x,y) = \left[\frac{1}{3}x; \frac{1}{3}y + \frac{1}{3}\right] \tag{2.42}$$

$$W_3(x,y) = \left[\frac{1}{3}x; \frac{1}{3}y + \frac{2}{3}\right] \tag{2.43}$$

2.7.4.5 Hybrid I-H Fractal Shape Generation Process

Hybrid fractals used to fill the whole space as much as possible to be useful in the proposed designs. I-Shape and H-Shape combination fractals shown in Figure (2.25) exhibit less self-similar than the first type. They are approximately similar under any magnification. Small parts of a quasi-self-similar fractal are not completely such as the whole fractal structures. The measurement of filling a small area with fractal curves can be determined from below equation:

$$D_f = log\,(k)/log(r) \tag{2.44}$$

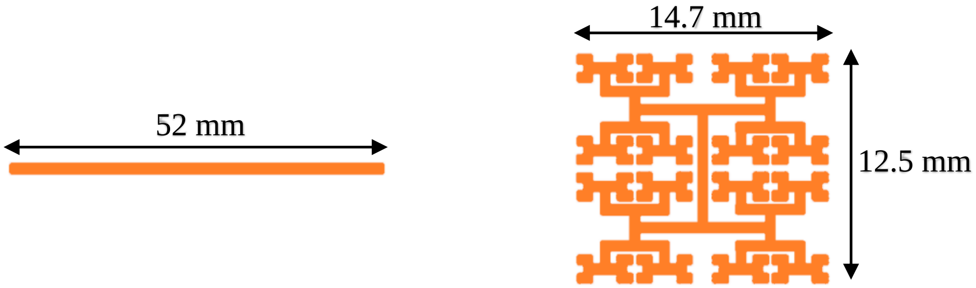

Figure 2.25

A comparison between the conventional straight-Line and its length equivalent Hybrid I-H fractal curve.

CHAPTER THREE

FULL MODE SIW BPF

3.1 Design Procedure of Hybrid I-H fractal Metamaterial-SIW

SIW design procedure and their mathematical equations will be discussed firstly in this section then the procedure of the Hybrid I-H fractal curves design, and their principles of the proposed SIW-Hybrid I-H fractal unit cell. Then the effective parameters of SIW-Hybrid I-H fractal unit cells extraction to illustrate how the unit cell operate below the cutoff frequency of the original SIW structure by both options which are convert the evanescent mode to the propagation mode to achieve the backward propagation (which have negative permittivity and permeability) and the forward propagation (which have positive permittivity and permeability). The equivalent circuit by lamped elements designed, derived, analyzed, and losses due to different factors are illustrated.

3.1.1 SIW design

As a planar form of waveguide, SIW can be a promising candidate for the conventional non planar rectangular waveguide, compatible with planar devices such as standard printed circuit board (PCB) or low temperature co-fired ceramic (LTCC). Compared to the classic rectangular waveguide, SIW preserves some similar characteristics to RWG, and exhibits its unique advantages than SIW as well, such as [104]: SIW having the same dispersion and propagation characteristics to conventional rectangular waveguide, self-electrical shielding, capability of high power handling, high Q-factor, and easily integrated with planner structures on the same substrate like stripline, microstrip, and co-planner wave guide.

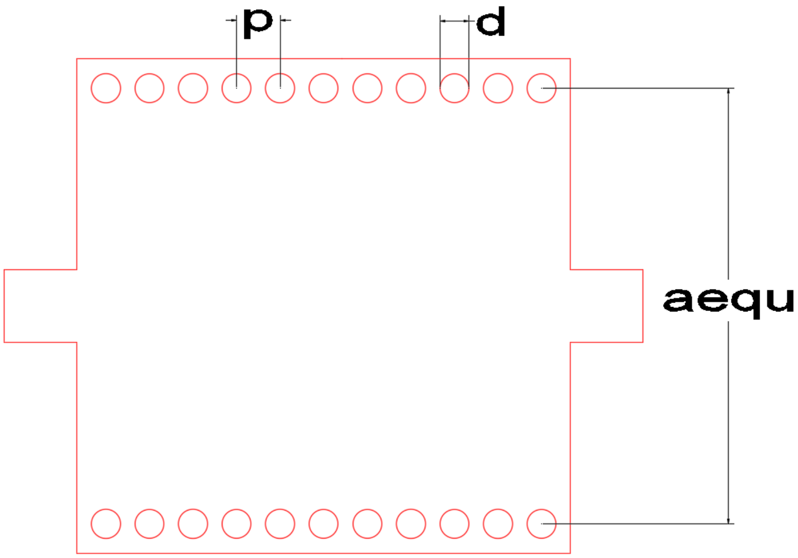

Figure 3.1. Dimensions of design for SIW are (aequ= 15 mm, d = 1 mm, p = 1.5 mm).

To achieve the desired cutoff frequency of the conventional SIW, the dimensions above were calculated using the equations (2.15-2.19), and the dielectric material for substrate was FR4 with thickness h=1.5, $\varepsilon_r = 4.3$, tangent loss=0.205, and copper conductivity $\sigma=5.8*10^7$ s/m.

3.1.2 Hybrid I-H fractal Curves Design

The proper dimension of Hybrid I-H fractal curves is between 1 and 2 for the Hybrid I-H fractal curves from the equation (2.44) ,where (k) is refer to the number of similar segments of the Hybrid I-H fractal curves which is obtained from the segment of the first iteration, and (r) is refer to the number of segments which obtained in each iteration. The Figure 2.25 shows how the conventional transmission line with a specific width can be converted to its equivalent curve, and it can be printed on the smaller region

The electrical length of both configuration in Figure 2.25 may be equality, and this property allows using of a transmission lines that are shorter in length but have a larger equivalent electrical length. This helps to miniaturize transmission lines, which is an important step to miniaturize of MW circuits. There are several well-known fractal curves nowadays, such as Koch, Sierpinski, and Piano. Some factors should be evaluated in advance to identify which fractal curve is appropriate for our design. One of the purposes explored in this thesis study is the miniaturization ratio which a fractal curve may introduce, therefore the fractal curve dimensions are selected as an important parameter. Fractal curves that reach dimension 2 are superior because of their capability to efficiently fill up small spaces, resulting in highly compact devices. In Figure 3.2 several fractal curves, including the H-shaped, Piano, and Hilbert fractal curves, have dimensions equal to 2, which is the maximum value. For reasons explained later in this study endeavor, we our fractal curve over others in our design.

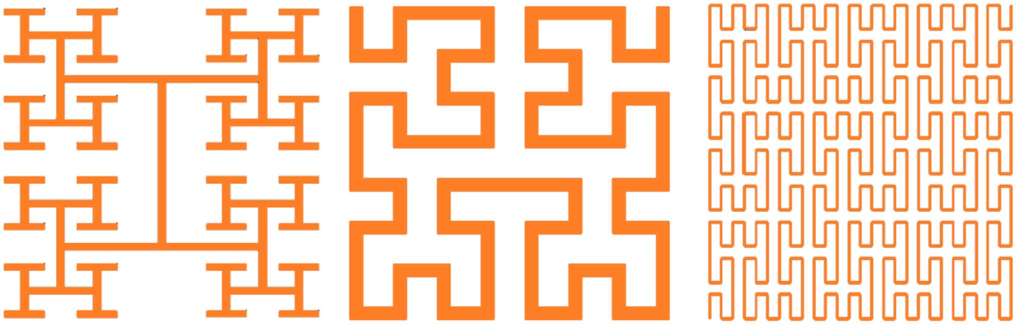

Figure 3.2 Three types of fractal curves (H, Hilbert, and Piano)

Figure 3.3 demonstrates the method of creating the fractal curve. As can be shown, the dimension of the fractal curve reaches the value 2 as the iteration order increases, filling the whole specified region.

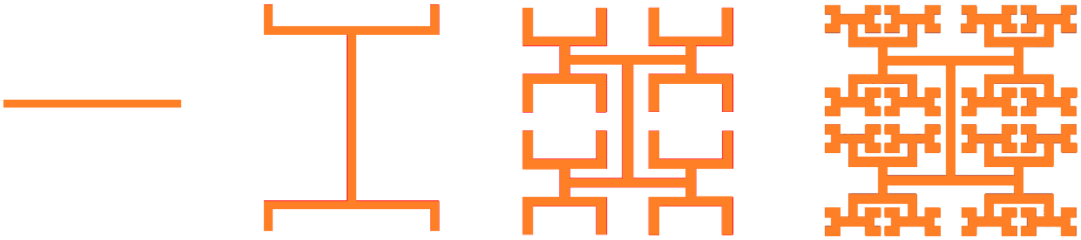

Figure 3.3. Process of the Hybrid I-H fractal curve generation.

3.2 The SIW-Metamaterial Unit Cells' Working Principles

In the proposal, conventional transmission lines are substituted with their fractal slot counterparts. The third iteration of a Hybrid I-H fractal was selected to satisfy the design criteria. To achieve negative permeability at the resonance frequencies, typically use a conventional slot engraved under a microstrip transmission line, as shown in Figure (3.4). Thus, the suggested Hybrid I-H fractal slot is utilized to achieve the negative permeability. Figure (3.5) depicts the extraction of a real parts of relative permittivity and permeability of a 3rd iteration Hybrid I-H fractal slot engraved under a transmission line on the ground layer using the S-parameters, and Figure (3.6 b) compares the effective permeability of the conventional and Hybrid I-H fractal slots. Figure (3.6 a) shows that a negative permeability for the design with the Hybrid I-H fractal slot ranges from 1.9 GHz to 3 GHz, and a bandwidth 1.9 GHz, while the negative permeability for the design with the conventional slot ranges from 5.4 GHz to 6 Hz, and a bandwidth 2.45 GHz. Furthermore, the permittivity remains positive for both designs at all frequencies. Hence the, evanescent waves emerge, producing band-stop filters BSFs in each of these frequency bands.

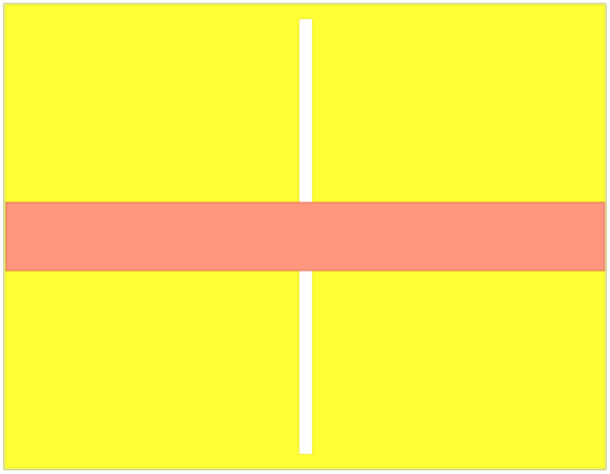

Figure 3.4.Structure with conventional slot.

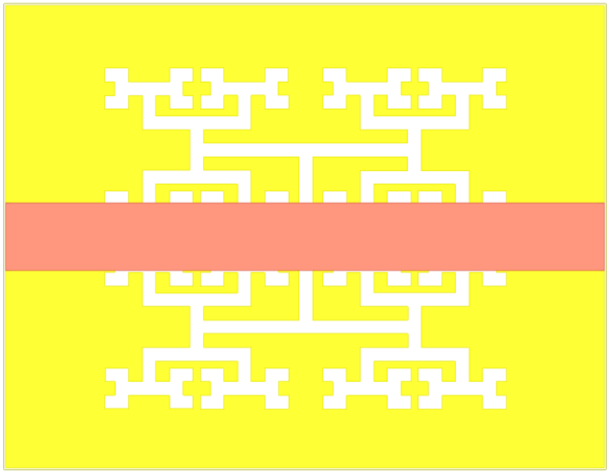

Figure 3.5 Structure with Hybrid I-H fractal slots,

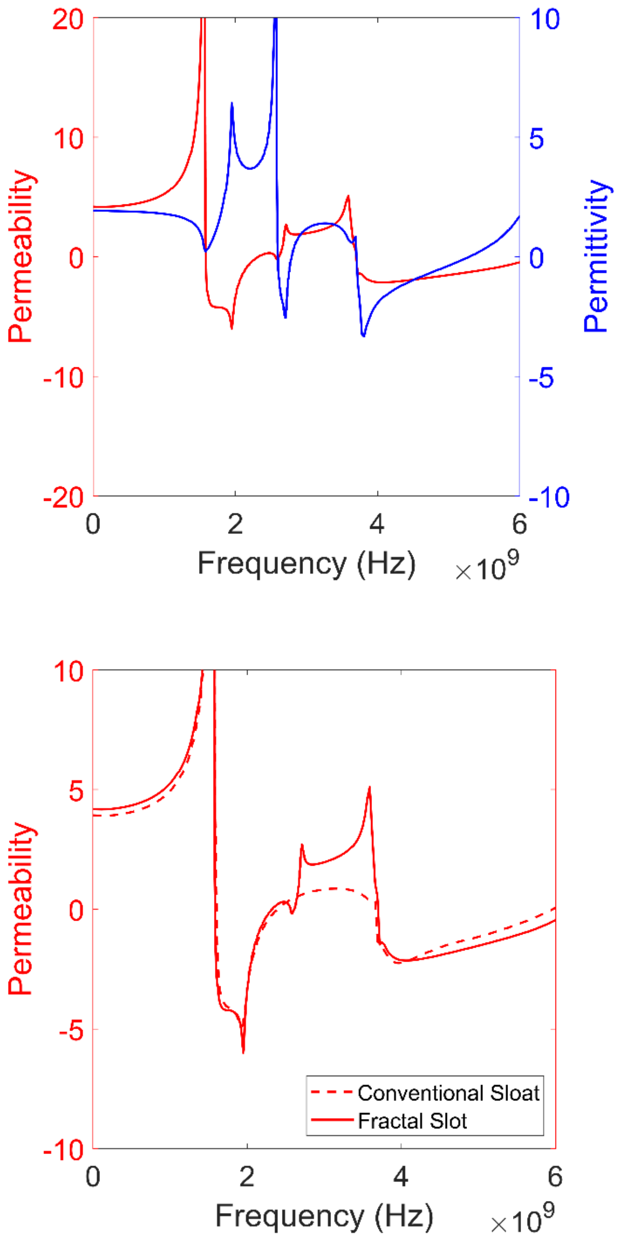

(a) (b)

Figure 3.6. (a) Effective permeability and permittivity of a structure with Hybrid I-H fractal slots (b) Comparison between the effective permeability of a structure with the 3rd iteration Hybrid I-H fractal slot structure with conventional slot,

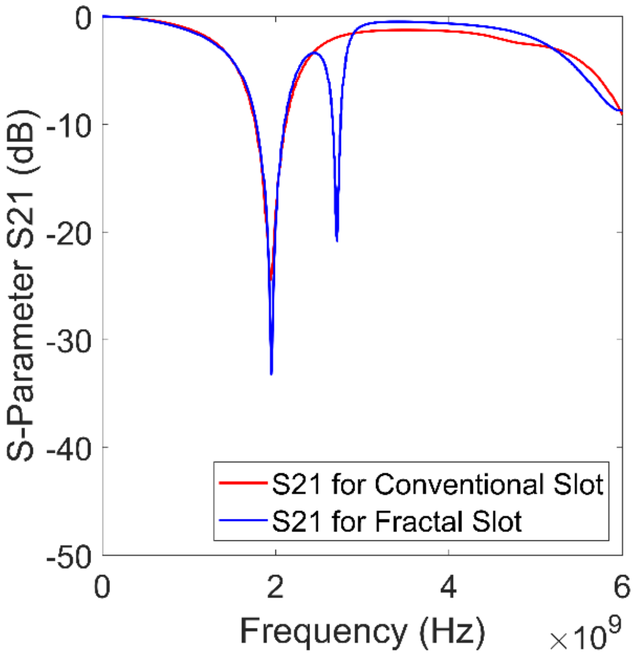

Figure 3.7 Simulated frequency responses S_{21} comparison

Figure 3.7 shows a compare the S_{21} of conventional and the S_{21} of the 3rd iterations Hybrid I-H fractal slots carved on the ground of conventional microstrip transmission lines. As shown, both designs restrict the signals passing from one port towards another almost at the same frequency, despite the fact that the two responses don't have the same BW. Miniaturization can be observed due to the fractal geometry's space filling feature. As a result, the frequency will decrease to the lower frequencies even the side length of the Hybrid I-H fractal slot equal to the side length of the conventional slot. To achieve the metamaterial, both permittivity and permeability should be negative. The substrate integrated waveguide SIW was used as a transmission line instead of the conventional microstrip in the proposed filter. The negative permittivity can achieve in the SIW structure under the cutoff frequency. As a result, the suggested design is simpler compared to the conventional metamaterial designs. [110]. As illustrated above, the slot that works as a magnetic dipole produces a negative permeability at specified frequency ranges. In the proposed SIW fillter, the Hybrid I-H fractal engraved on the upper layer of board. Slots, on the other side, can be engraved on the bottom layer of the SIW structures, giving the same response. However, leaving the ground layer solid, it is preferable to minimize the noise and the radiation losses in the high-frequency radio systems. To obtain a high couplings between both the Hybrid I-H fractal slot and the SIW structures, the Hybrid I-H fractal slot are engraved on the waveguide center and excited by the greatest electric field of a dominant mode TE10. Three metamaterial Hybrid I-H fractal unit cells as well as the conventional SIW structure are showing in Figure 3.8. The SIW metamaterial unit cells for the first, second, and third Hybrid I-H fractal slot iteration are shown.

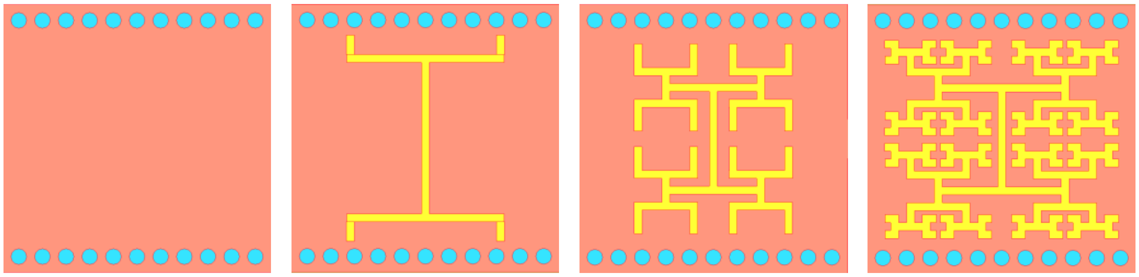
(a) (b) (c) (d)

Figure 3.8. (a) Conventional SIW, (b) The 1st iteration Hybrid I-H fractal SIW, (c) The 2nd iteration Hybrid I-H fractal SIW, (d) The 3rd iteration Hybrid I-H fractal SIW

All the simulations and fabrications were performed on a FR4 substrate with a height of 1.5 mm and a dielectric constant of 4.3. The equivalent width of SIW a_{equ} was 15 mm to achieve the cutoff frequency at 5.2 GHz; the diameter of via d was1 mm, the distance between two adjacent vias b was 1.5 mm; the Hybrid I-H fractal curve side length p was

12.5 mm; and the width of slot g was 0.5 mm. The S-parameters of the conventional SIW and the SIW metamaterial Hybrid I-H fractal unit cells are shown in Figure 3.9. As can be shown, the metamaterial unit cell allowing signals to propagate under cutoff frequency of SIW structure about 5.2 GHz, whereas the conventional SIW prevents propagating the signals under that frequency having evanescent modes. So, may be called an evanescent resonators. Figure 3.10 and Figure 3.11 are shows the distribution of current for the conventional SIW design and the 3rd iteration of the SIW metamaterial Hybrid I-H fractal unit cell to prove that the signals propagation allowed in the SIW metamaterial Hybrid I-H fractal unit cell structure and prevented in the conventional SIW structure under the cutoff frequency, let's take 2GHz as example. And the distribution of current for the 3rd iteration of the SIW metamaterial Hybrid I-H fractal unit cell at the frequencies 1GHz and 5GHz to prove also how the signals prevented from propagation under the cutoff frequency.

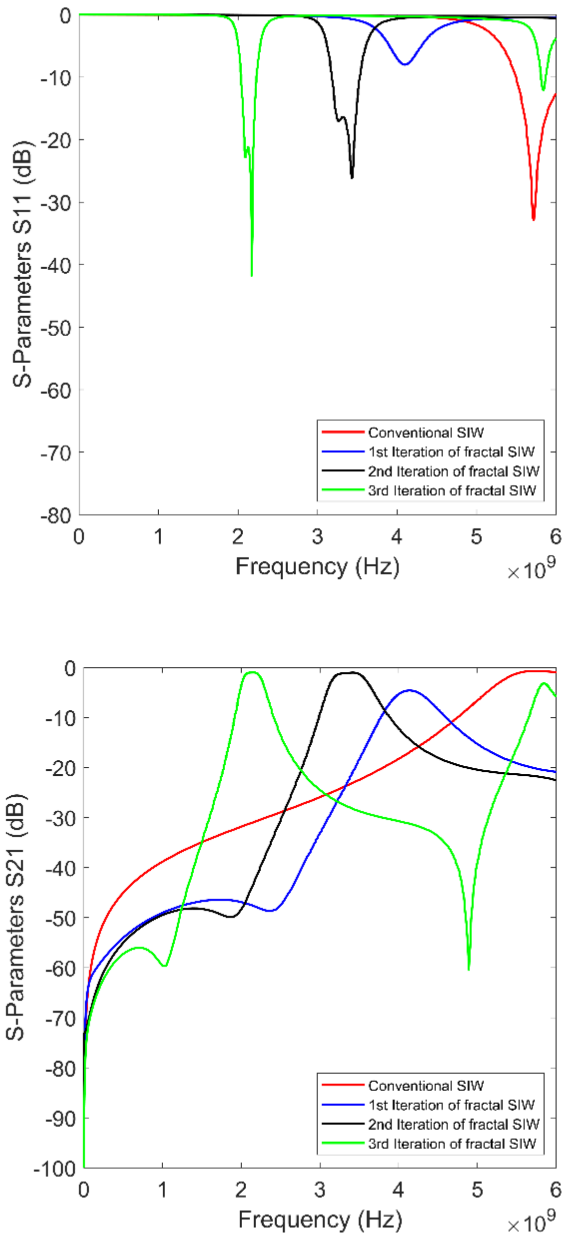

(a) (b)

Figure 3.9. Frequency responses of structures shown in Figure 3.8 (a) :(S11), (b) :(S21)

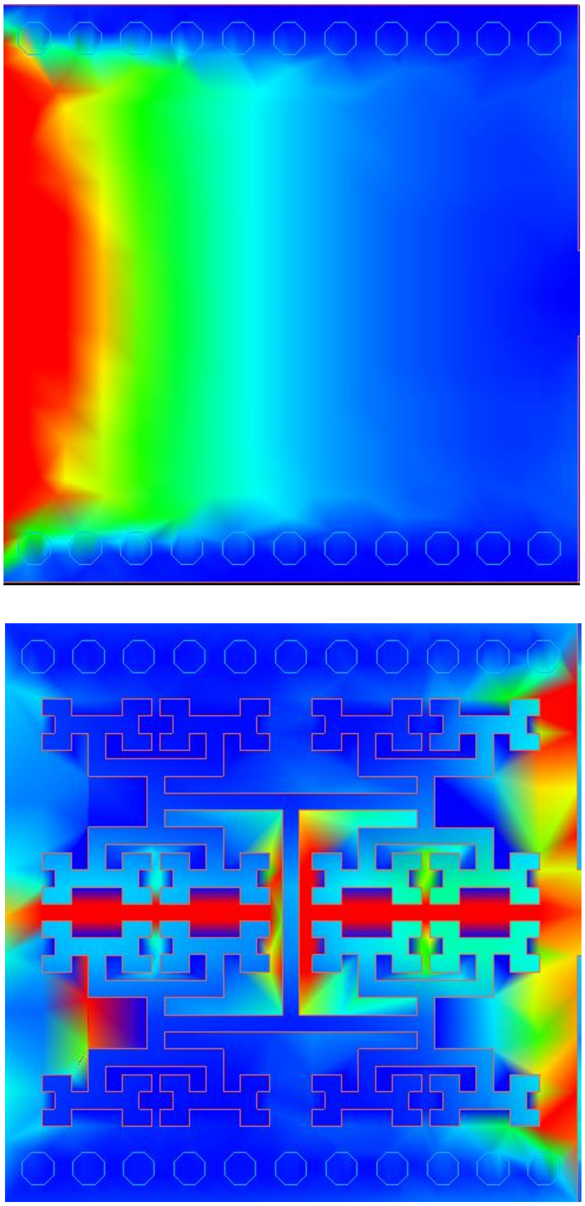

(a) (b)

Figure 3.10. Current distribution at 2GHz inside (a) the conventional SIW (b) inside the 3rd iteration Hybrid I-H fractal SIW-metamaterial unit cell

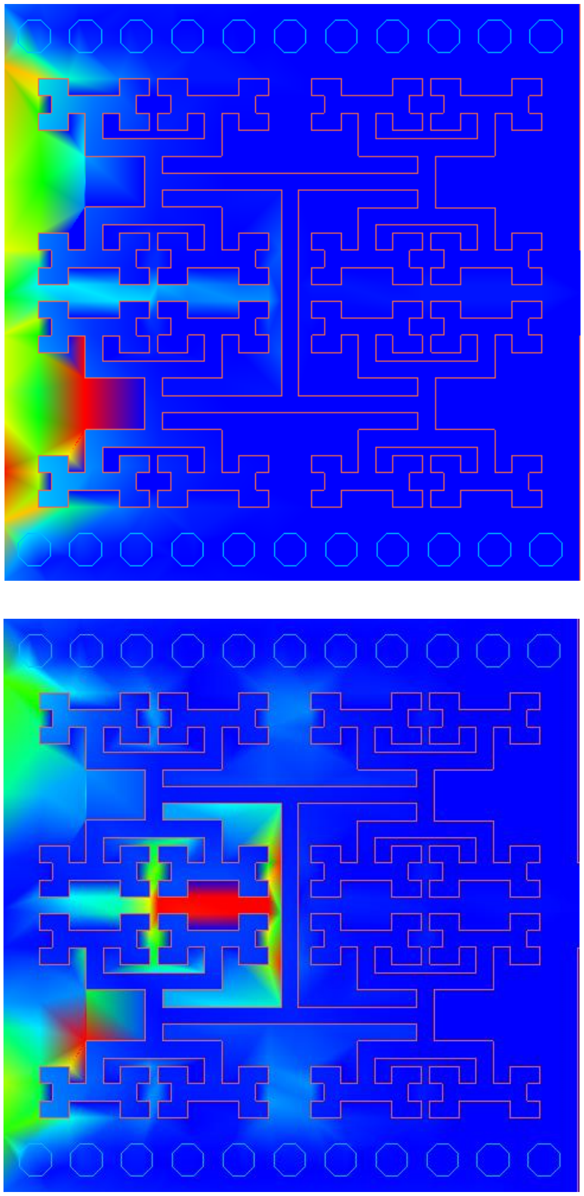

(b) (c)

Figure 3.11. Current distribution inside the 3rd iteration Hybrid I-H fractal SIW-metamaterial unit cell (a) at frequency 1GHz, (b) at frequency 5GHz

The previous figures provide a fast overview of which frequencies can be distributed inside the designated unit cells. The Hybrid I-H fractal slots behave as a conventional inductance when excited by the normal dominant electrical fields components extended from the ground to the broad wall of the SIW, whereas the magnetic field components are in parallel to the upper wall of the SIW structure and normal to the sides. Furthermore, as the Hybrid I-H fractal iteration increases, the passband's center frequency decreases. The passband slightly under the cutoff frequency of the conventional SIW structure being clear in the response for the 1st iteration of the SIW metamaterial Hybrid I-H fractal unit cell, emergence of the passband at the frequency 4.2 GHz. In other words, the conventional high pass response of the SIW were converted to the bandpass. The center frequency of both the SIW metamaterial Hybrid I-H fractal unit cells in the 2nd iteration and 3rd iteration were 3.875GHz and 2.959GHz, respectively. Keeping the same side lengths for multiple iterations of the Hybrid I-H fractal slots engraved on the SIW metamaterial unit cells of the same overall size resulted in responses with varying frequencies, which was similar to a size decrease. The reductions ratios of the 2nd iteration and 3rd iteration for the SIW-metamaterial Hybrid I-H fractal unit cells were 32.9% and 51.6%, respectively, when comparing to the 1st iteration unit cell. As shown in Figure 3.9, the 2nd iteration and 3rd iterations of the SIW-metamaterial Hybrid I-H fractal unit cells produce good filtering response. The Hybrid I-H fractal slots engraved on the upper layer of SIW structures created two transmission poles that coupled and excited two different modes. Additionally, the two transmission zeros were created, which enhanced the selectivity of filtering. The SIW metamaterial Hybrid I-H fractal unit cells showed high pass characteristics placed after the pass - band that shifted to the frequencies higher than the original cutoff frequency of SIW structures.

Because the suggested SIW-metamaterial Hybrid I-H fractal unit cells restrict the dominant modes TE_{01} by slots, the guides become shorter. Readers can find more information at [111].

3.3 Metamaterial Parameters

The designed metamaterial unit cells were studied and investigated to show that they had negative permittivity and negative permeability at certain bands in order to further explain the principles of the backward propagation of pass - band under the cutoff frequency of the SIW structure. For a simplicity, just the SIW metamaterial Hybrid I-H fractal unit cell with a 3rd iteration was used to obtain its effective metamaterial characteristics. Figure (3.12 a) showing the comparison between the response of the conventional SIW with the same overall dimension and the transmission response of the 3rd iteration of SIW metamaterial Hybrid I-H fractal unit cell at 2 GHz. Since the total size of the Hybrid I-H fractal slot is important in determining the passband's center frequency, three separate sizes for the third iteration Hybrid I-H fractal slots were etched on the upper layer of the SIW structure.

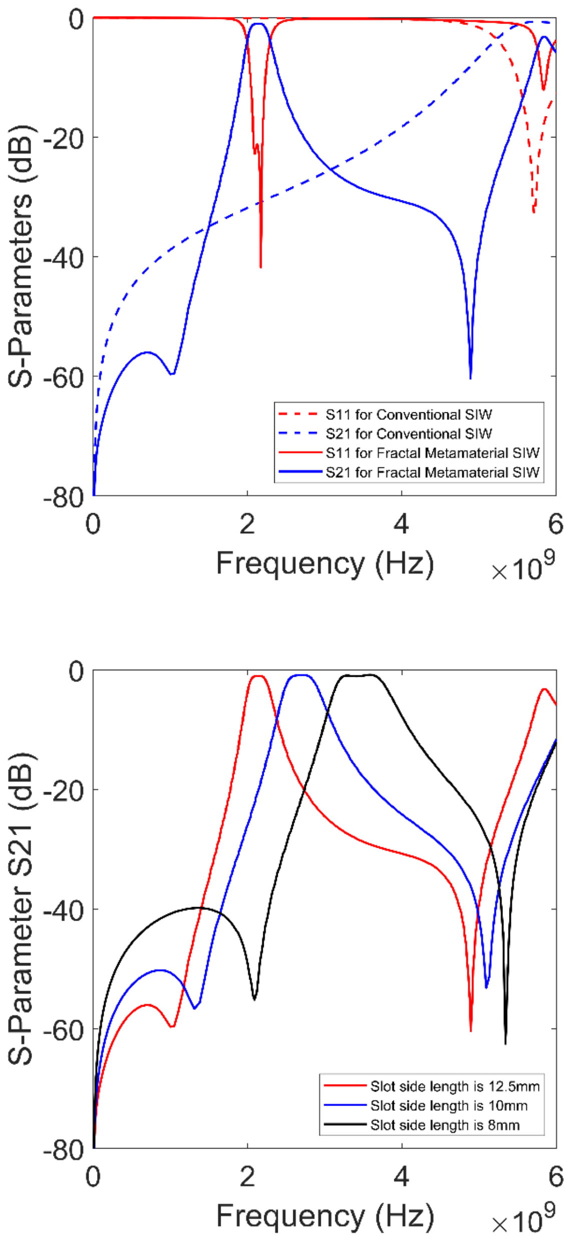

(a) (b)

Figure 3.12. (a) A comparison between the frequency response of the 3rd iteration Hybrid I-H fractal SIW-metamaterial unit cell, (b) the transmission coefficient (S21) of the 3rd iteration Hybrid I-H fractal SIW-metamaterial unit cell for three different Hybrid I-H fractal slot sizes

These sizes have b = 8 mm, 10 mm, and 12 mm as a side lengths. The frequency reduces as the overall size of the Hybrid I-H fractal slot increase, as seen in Figure (3.12 b), where the insertion losses (S21) are shown. The larger size of the third iteration Hybrid I-H fractal slot was used in all subsequent designs. The simulation result (permittivity and permeability) of the SIW metamaterial Hybrid I-H fractal unit cell with 3rd iteration are shown in Figure (3.13). The highlighted regions in the figure represent places where both permittivity and permeability were simultaneously negative or positive, giving for backward propagation or forward propagation. Based on the simulated S-parameters, these two important metamaterial parameters were obtained. Based on the results, we conclude that there are two kinds of propagations based on permittivity and permeability signs. They are negative from 1.97 GHz to 2.17 GHz, then their signs shift to positives from 2.17 GHz to 2.42 GHz. Luckily, these two frequency ranges are very near together, resulting in a balanced response. It is important to note that our designed metamaterial unit can propagate both backward and forward. Figure (3.14) shows a normalized dispersion graph with both negative and positive slopes for backward and forward propagation respectively. The appearance of the two poles in the transmission responses of the metamaterial unit cells as a result of these two types of propagation modes is referred to as dual mode responses. The attenuation constant graph, as shown in the Figure (3.14), is another indicator showing that signals pass through the proposed waveguide under the cutoff frequency due to the losses are very low. Furthermore, there is no ripple in the transition of the attenuation constant graph between both of backward and forward propagation regions.

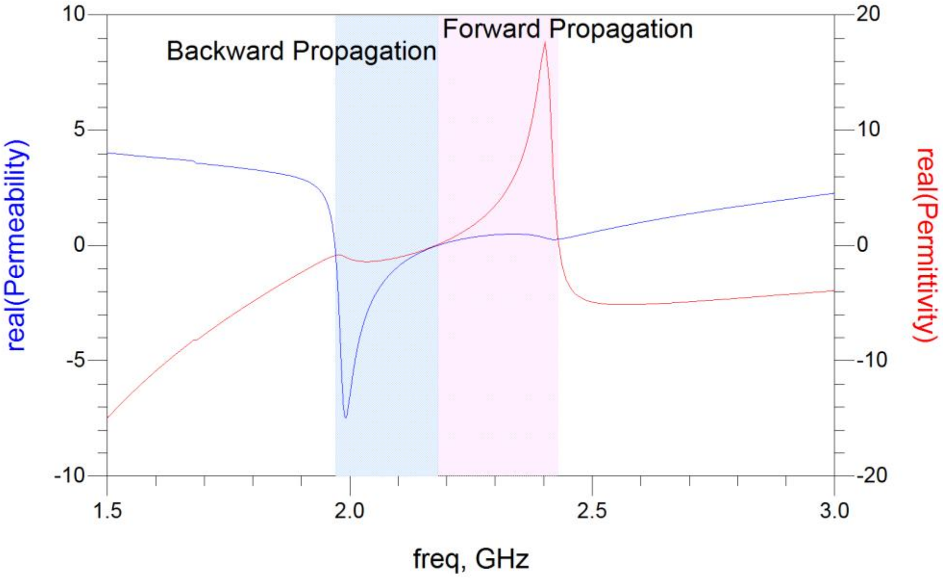

Figure 3.13. Permittivity and permeability (constitutive parameters) of the 3rd iteration Hybrid I-H fractal SIW-metamaterial unit cell

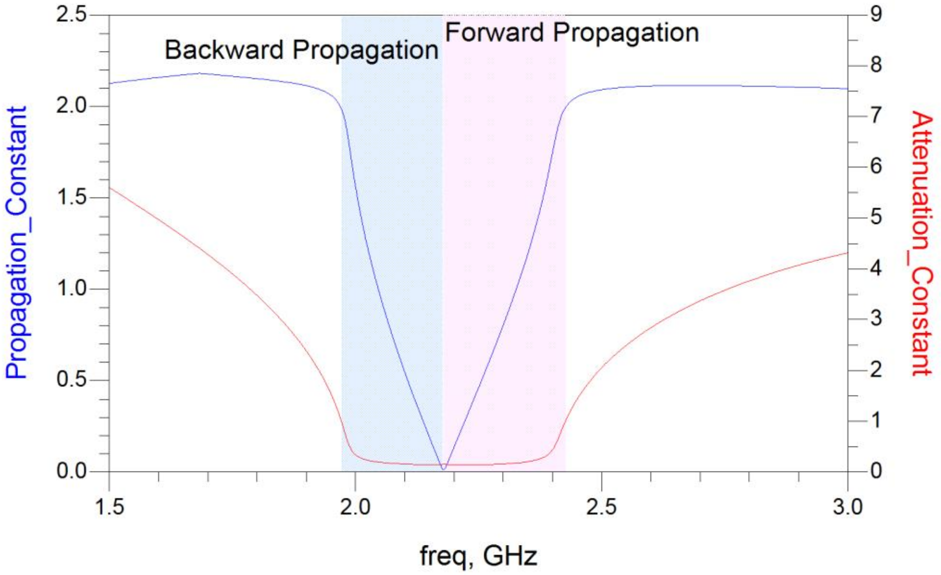

Figure 3.14. Propagation and attenuation constants of the 3rd iteration Hybrid I-H fractal SIW-metamaterial unit cell.

3.4 Circuit Model and Losses

Figure (3.15) shows the equivalent-circuit model that was used to anticipate the behavior of the proposed unit cell. The model begins by assuming the SIW structure as a conventional two wire transmission line constructed by the top layer of the SIW and the ground layer, which is interconnected to an unlimited number of short circuited stubs inserted along the equivalent transmission line. There are transmission line components are connecting between the array of vias and the equivalent two wire transmission line, so the short circuited stubs seem as an equivalent inductance, symbolized by L_{via}, when seen from the guide center. This inductance adds to the SIW structure's highpass properties. The SIW's corresponding transmission-line is expressed by distributed shunt capacitor C_d and distributed series inductor L_d. A series capacitor C_{frac} is used to represent the Hybrid I-H fractal slot. The coupling between the SIW structure and the Hybrid I-H fractal slot is a hybrid of magnetic in nature (inductive) and electric (capacitive). The terms C_c and L_c were created to represent the type of couplings. C_c symbolizes the capacitive coupling between the SIW's ground and the tiny patches bounded by the fractal slots arms.

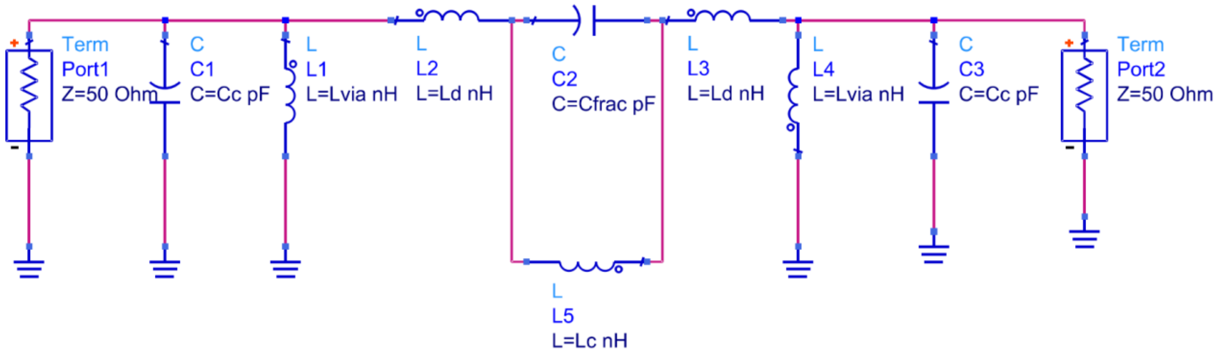

Figure 3.15. The equivalent-circuit model of the SIW-metamaterial unit cell (L_d = 1e-6 nH, L_c = 10.52 nH, L_{via} = 0.364 nH, C_d = 8.96 pF, and C_{frac} = 2.11 pF),

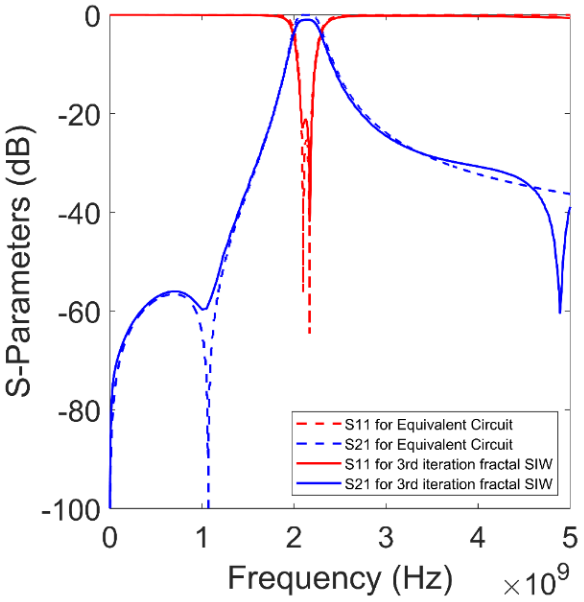

Figure 3.16. A comparison between the frequency response (S11 and S21) of the 3rd iteration Hybrid I-H fractal SIW-metamaterial unit cell and its equivalent circuit model.

C_c is automatically included inside C_d since C_d is dominant. As a result, C_d can be found in our formulae but not available in the equivalent circuit. L_c represents the inductive coupling formed by the Hybrid I-H fractal slots and SIW structure. The suggested circuit model is only applicable for a specific frequency range, and it does not compensate for the impact of high order modes of the resonators. Furthermore, for the purpose of simplicity, dielectric, material, and radiation losses are neglected. Despite being a basic circuit model, it clearly forecasts the transmission properties of the suggested unit cells. The Figure (3.16) compares the results of the circuit model with the full-wave simulation using the advanced design system ADS. The description of Figure 3.15 shows the values of the lumped components. These values of lumped elements were determined using ADS's built-in optimization tool. Hundreds of iterations were performed in order to match the frequency responses of the full wave electromagnetic solver with the circuit model. However, there is a mismatch since the equivalent circuit model has neglected the effects of many elements. We can deduce the effects of equivalent lumped components on the overall response of the unit cell from the circuit, therefore we may tune the unit cell dimensions to achieve any desirable frequency response, as detailed below.

Eq.(3.1) gives the frequency of the 1st transmission zero appearing below the passband.

$$f_z = \frac{1}{2\pi\sqrt{L_c C_{frac}}} \tag{3.1}$$

The position of the transmission zero is controlled by L_c. The transmission zero shifts towards lower frequencies by increasing L_c . It is well known, when the transmission zero positions are near to a passband, the rejecting roll-off is extremely sharp, resulting in improved the selectivity of filters. The value of L_c is determined by the intensity of magnetic coupling between SIW and the Hybrid I-H fractal slot. In other words, the value of L_c is determined by the slot width g and the position of Hybrid I-H fractal slot. As shown in Figure (3.16), when shifting the position of the 1st transmission zero by changing the position of the Hybrid I-H fractal slot, which in turn changes L_c. Furthermore, all of the designed unit cells have a dual-mode response. Because of the low coupling between the SIW and the Hybrid I-H fractal slot, the dual-mode response of the 1st iteration of the SIW-metamaterial Hybrid I-H fractal unit cell is not noticeable. The frequency of the first mode is controlled by C_{frac} and L_d. In other words, the dielectric constant of the substrate, as well as the size, thickness, and width of a slot, are the major parameters that control the values of these equivalent lumped components.

The 1st mode frequency is determined from below equation:

$$f_{1st.mode} = \frac{1}{2\pi\sqrt{(L_d + L_{via})(C_{frac} + C_d + C_c)}} \tag{3.2}$$

As shown, the C_{frac} contributes to both transmission zero and 1st mode frequencies at the same time. And 2nd mode's frequency is given below:

$$f_{2nd.mode} = \frac{1}{2\pi\sqrt{L_{via}(C_d + C_c)}} \tag{3.3}$$

This assessment assists in determining which parameters could be utilized to assess the response of specified unit cells. However, once choosing the basic SIW dimensions, a few of these factors, like L_d, C_d, and L_{via}, cannot be changed. However, C_{frac} and C_c are the two most vital factors that affect the frequencies of the suggested unit cells.

Losses in the designed unit cells are treated as a practical problem found throughout the design process. However, calculations the overall losses become less than 0.16, as shown in Figure (3.17). These losses have been normalized and determined with the Eq (3.4).

$$Losses = 1 - |S_{21}|^2 - |S_{11}|^2 \tag{3.4}$$

The radiation losses grew as slot width grew, resulting in more power leaking into space. The Hybrid I-H fractal slot behaves similarly to the magnetic dipole antennas because it operates as a conventional inductance (magnetic diploe). The extremely minor radiation will be typical on the structure, but it can be simply avoided by shielded covering. The neighboring components will be unaffected. I in the suggested unit cells, the radiation losses are lower than in [111, 112]. They have benefits in terms of selectivity and size, in addition to reduced radiation loss.

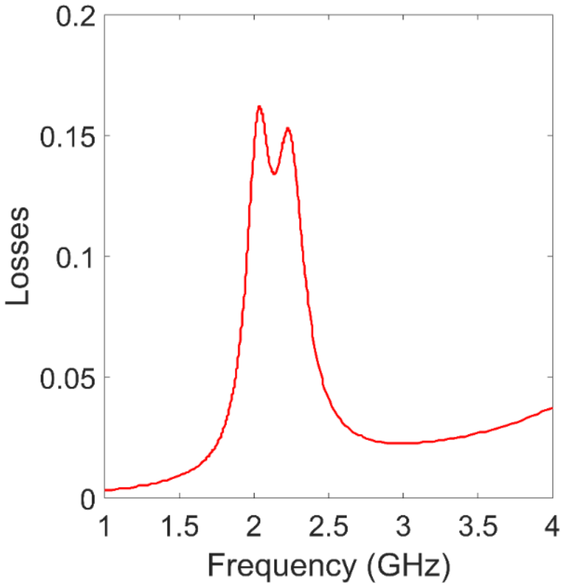

Figure 3.17. Calculated the losses in dB for the 3rd iteration Hybrid I-H fractal SIW metamaterial unit cell.

3.5 Methodology of filter design

After investigating and discussing the suggested metamaterial Hybrid I-H fractal unit cells previously in this thesis, we would then proceed to build filters with only the 3rd iteration for the proposed in SIW-metamaterial Hybrid I-H fractal unit cell [113]. The regular methodology employed to achieve the design parameters is determined by the external quality factor (QF) and the coupling coefficient factor (k). Using the simulator (advanced design system ADS), three alternative filters are simulated. The 3rd iteration of SIW-metamaterial Hybrid I-H fractal unit cell illustrated in Figure (3.8 d) and its dimensions mentioned in the Table (3.1) as shown in Figure(3.18) serves as the foundation for the three filters given in this subsection, which are one, two, and three orders SIW-metamaterial filters. In the other words, the number of filter stages is determined by the number of using the unit cells in the suggested filters as shown in Figure (3.19). Although the suggested SIW metamaterial Hybrid I-H fractal unit cells provide transmissions of passbands below the original SIW structures' cutoff frequency, there's no control over their bandwidths and S-parameters. However, the combination between the SIW structure and Hybrid I-H fractal slots can enhance the degree of flexibility sufficient to achieve the desired filter specification. In this subsection, the filter design process will be discussed briefly using the conventional coupled resonator scheme. A brief description of the design procedure is presented at the outset, followed by a straightforward example that can serve as a guide. First, filter requirements-based circuit synthesis is shown. The characteristics of the low-pass filter, the coupling coefficient and external quality factor, can be calculated in terms of the circuit parts. These quantities are calculated to assist build a connection between both the SIW Hybrid I-H fractal slot interaction, which in turn defines the low-pass filter design components' physical dimensions.

As was indicated before, dual poles, also known as dual modes, are present in the responses of all of the proposed unit cells. This is the case in general. The coupling coefficient and the external quality factor can both be determined with the use of these two distinct resonance frequencies. The formula for the coupling coefficient is as follows:

$$k = \frac{f_2^2 - f_1^2}{f_2^2 + f_1^2} \tag{3.5}$$

While the external quality factor is determined by the following:

$$Q_F = \frac{2f_0}{BW} \tag{3.6}$$

Where f_2 and f_1 are the upper and lower modes' frequencies of the electromagnetically coupled the SIW structure with the Hybrid I-H fractal slot resonator. A 3 dB bandwidth is denoted by BW, while f_0 is the center resonance frequency. Some design dimensions were carefully tuned during investigations to extract both the coupling coefficient k and the external quality factor Q_F.

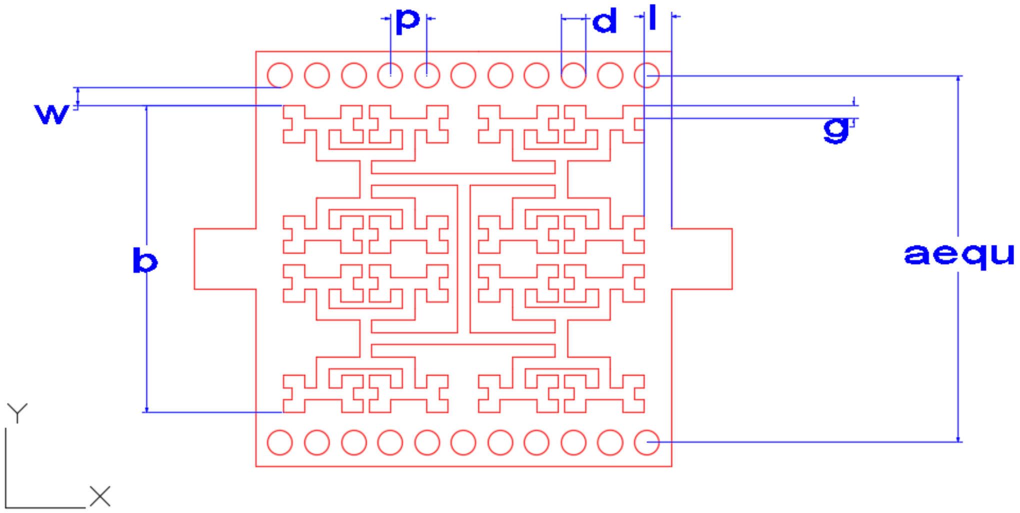

Figure 3.18. Dimensions variables of design for all proposed filter

Table 3.1. Dimensions variable and values of Design

Symbol	Description	Value
a_{equ}	Equivalent width(Distance between sides row of vias	15 mm
w	Distance between the fractal and sides vias	0.73 mm
l	Distance between the fractal and sides edge	1.12 mm
d	Via diameter	1 mm
p	Distance between two adjacent vias	1.5 mm
b	Side length of fractal	12.5 mm
g	Fractal line width	0.5 mm

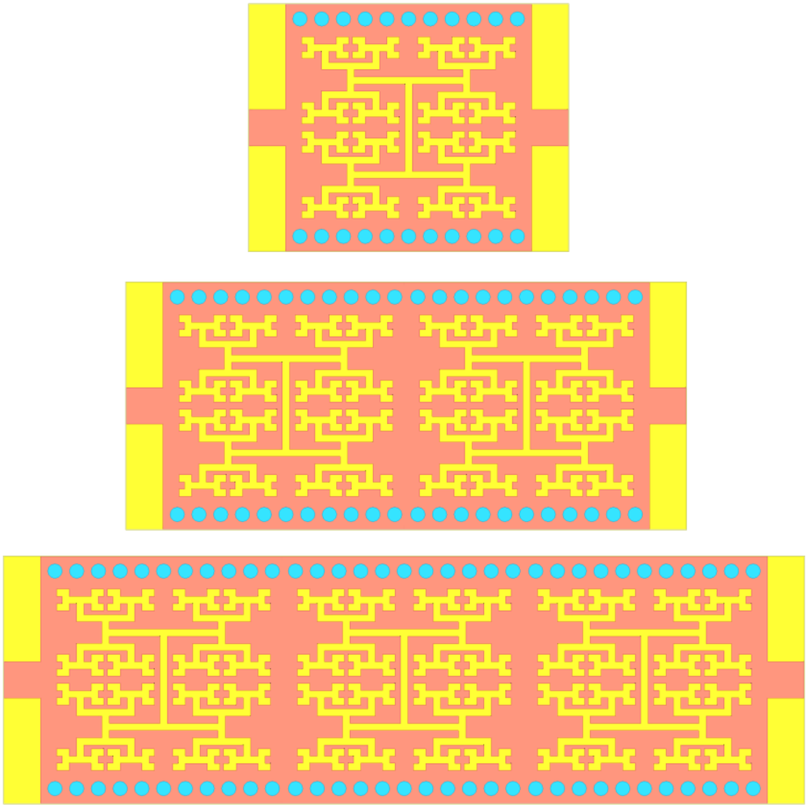

Figure 3.19. Layout of 3rd iteration Hybrid I-H fractal SIW-metamaterial bandpass filter one stage, two stages, and three stages

During experiments, researchers fine-tuned several design parameters in order to determine the external quality factor Q_F and the coupling coefficient k. In order to optimize the design, we can graph two curves, one for the external quality factor and the other one for the coupling factor k and, against the physical dimensions of the suggested filters. The suggested SIW metamaterial Hybrid I-H fractal filter has one stage and three iterations, hence only the third iteration's parameters Q_F and k are shown. Assuming k and Q_F are known, the optimal physical dimensions for the three filters mentioned in this thesis can be calculated. A simple case study is provided as an example. See Figure (3.19) for a specific implementation of a single-stage SIW-metamaterial filter that makes use of a single Hybrid I-H fractal slot generated by the third iteration. Altering the filter's physical w1 and l dimensions yields new values for k and Q_F, which can be used in the same way as before to characterize the filter's performance. The filter has a passband of about 2.15 GHz with a bandwidth of around 0.3 GHz. The SIW has a dual-mode response, despite only having a single Hybrid I-H fractal slot. In this case, we synthesize a circuit of the second order with the parameters $Q_F = 13.6$ and $k12 = k21 = 0.046$. The resonator's starting dimensions are obtained from an electromagnetic simulation (i.e., unit cell). To easily distinguish between the even and odd resonance frequencies of the dual mode behavior, a larger external quality factor is recommended. The electromagnetic advanced design system ADS simulator was used to optimize the primary dimensions of the design curves. Additional physical dimensions are taken into account during filter design; however, they are not mentioned here. Two more filters are provided in this work, each of which has been improved in the same way as the first. Several options can be used for adjusting the external quality factor and the coupling coefficient. Meanwhile, the equivalent circuit model shown above can be used to help establish some design features, such as those that control the bandwidth and the transmission zeroes. Schematics for both the two- and three stage SIW-metamaterial filters are be shown in Figure 3.19. After extensive adjustment and optimization using the electromagnetic solver ADS, the physical dimensions of these two filters have been obtained. Keep in mind that the higher the filter order, more the number of usage slots.

3.6 Result of the simulation and measurements

In this subsection, we put the filters we've been talking about in the preceding chapters to demonstration and practically validation. Figure 3.21 shows photos of the finalized the 1st order filter fabrication. As seen in Figures 3.19, the filter stage makes use of a number of Hybrid I-H fractal slots engraved into each SIW unit cell. The Hybrid I-H fractal slots, now in their 3rd iteration, are engraved over the upper layer of the SIW structures and distributed in a linear fashion along the printed waveguide (SIW). The fabrication used the conventional printed circuit board (PCB) procedure by my owned CNC machine, making use of a FR4 substrate with a thickness of 1.5 mm as shown in Figure (3.20) and a relative permittivity of 4.3. All simulations accounted for dielectric and metallic losses by using the substrate's tangent loss of 0.025 and copper's conductivity (σ) of $5.8*10^7$ S/m. We utilized a vector network analyzer (VNA) as shown in Figure (3.22) to evaluate and measure the filters' efficiency. The simulated data was compared to the measured data, and they showed a significant level of agreement.

Figure 3.20. Fabrication process.

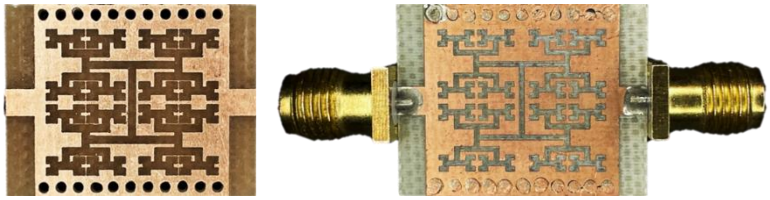

Figure 3.21. A prototype of the fabricated FMSIW filter

In the Figure 3.21 can see the fabricated 1st order filter is quite tiny although acting as a type of waveguide filter. Table 3.1 provides all of the filter dimensions. Figure 3.23 shows a comparison between the simulated and measured frequency responses of a single-stage, 3rd iteration SIW-metamaterial Hybrid I-H fractal filter. With two poles in the passband, the bandwidth BW at -3 dB was around 0.3 GHz, and the center frequency f0 was roughly 2.15 GHz. As a result of the high internal coupling coefficient and low external quality factor. What's more, the slots can be resized to satisfy any desired frequency. Further, two zeros are seen at frequencies of 1 GHz and 4,8 GHz. Measured insertion loss was around -1.5 dB, which includes losses induced by the SMA connections that were not taken into account in the simulation. The measured return loss (Lowest in-band reflection coefficient) was about -19 dB and the results are near to match the value of simulation.

Figure 3.22. Measuring S-Parameters with VNA

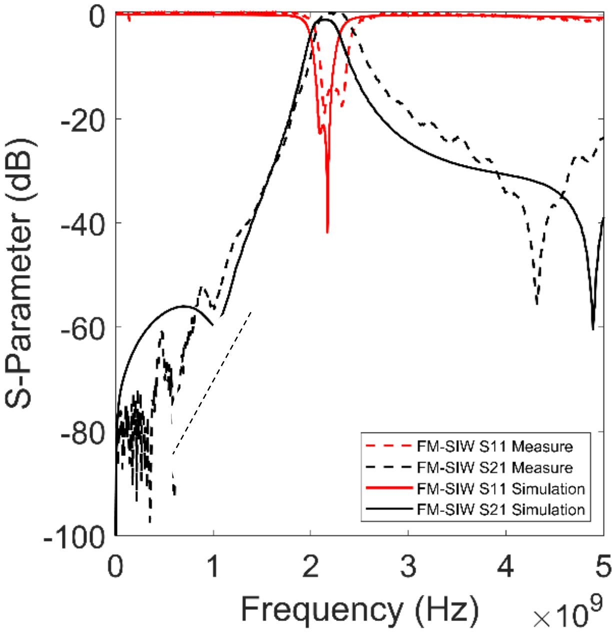

Figure 3.23. Measured and simulated transmission response of the one stage 3rd iteration Hybrid I-H fractal SIW-metamaterial bandpass filter.

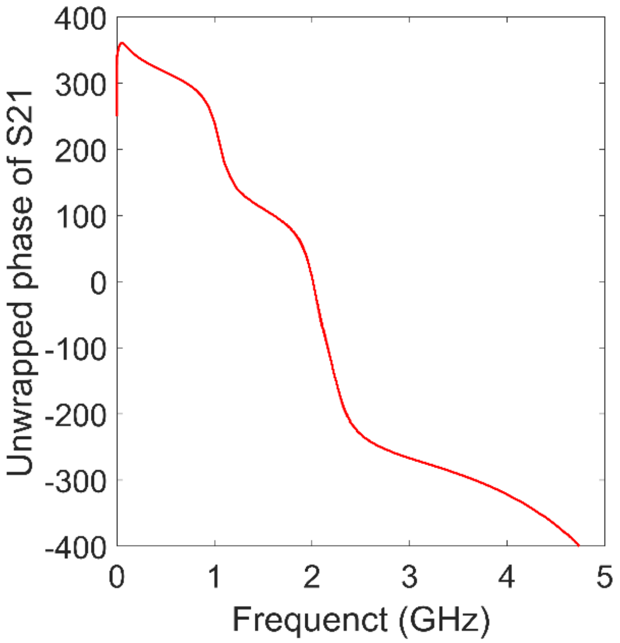

Figure 3.24. Measured unwrapped phase of S21 response of the one stage 3rd iteration Hybrid I-H fractal SIW-metamaterial filter.

Transmission zeros are well-known to help improve filter selectivity in the frequency response. The findings show that the rejection in the lower stopband is roughly -45 dB, while in the upper stopband it is approximate to -30 dB. The suggested one-stage filter's measured unwrapped phase response is shown in Figure 3.24. Within the passband, between around 1.9 GHz and 2.15 GHz,

Figure 3.25 (a) and (b) show the simulated frequency responses (S-Parameters) of the two and three stage of the 3rd iteration FM-SIW metamaterial Hybrid I-H fractal filters. Figure (3.25) (a) show three poles also, the filter in (b) have three poles. Two transmission zeros before and follow the passband in the second and third filters. The filter response roll-off gets very sharp. Both filters has a center frequency about 2.3 GHz and the 3 dB bandwidth of about 0.5 GHz. As can be observed, the suggested two and three stage filters move the center frequencies of the suggested one stage filter down to roughly 2.3 GHz.

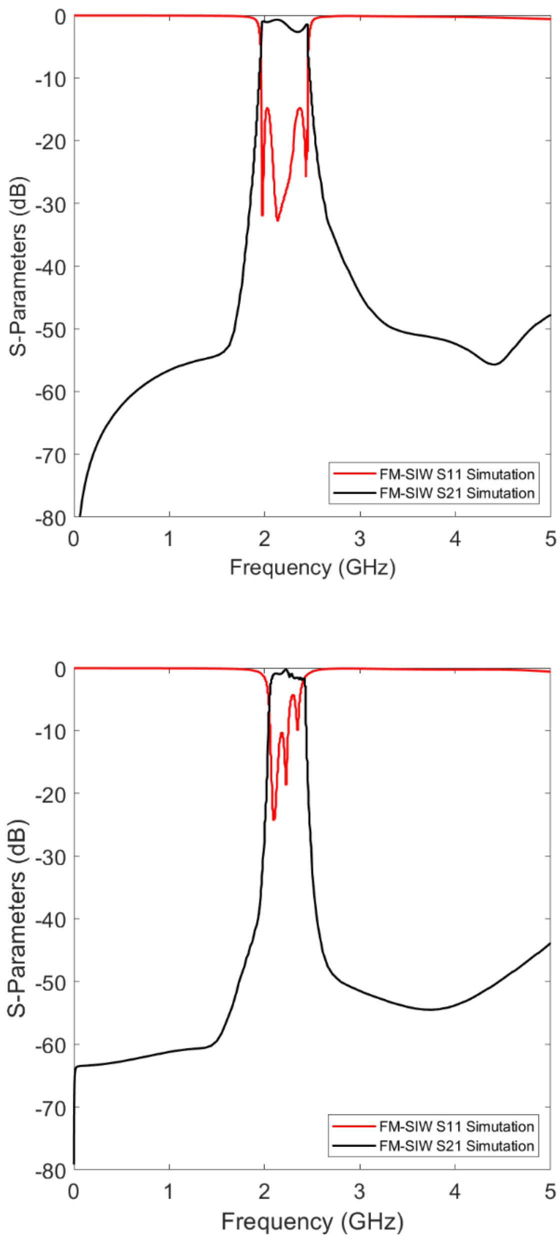

a) b)

Figure 3.25 Simulation result of scattering parameters: (a) the 2nd order FM-SIW, (b) the 3rd order FM-SIW

This is typical for filters with additional slots due to electromagnetic interaction between slots. The last two filters have a broader bandwidth as well. The 2nd and 3rd filters' maximum insertion loss and lowest return loss. Thus, the out-of-band rejection improves with an increase the number of slots utilized in our suggested design, however this comes at the expense of a bigger overall design.

CHAPTER FOUR

HALF MODE SIW BPF

4.1 Half-Mode Substrate Integrated Waveguide Bandpass Filter HMSIW-BPFs

In this chapter, the proposed HMSIW BPFs will be investigated, designed, analyzed, fabricated, and tested. The design procedure starts the FMSIW BPFs, and then they are converted into the HMSIW-BPFs exploiting the magnetic-wall property. This property is combined with the property presented in the last chapter to introduce a new thesis gap. Next, the proposed works are fabricated and tested to prove that our proposed ideas are valid for thesis and investigation. Finally, the chapter discusses and compares the simulation and measured results, and the comparison between the proposed work and the literature is presented as well.

4.2 Design procedure

The HMSIW filter proposed in this chapter originated from the FMSIW filter which was presented in the former chapter. Figure (4.1) displays both FMSIW and HMSIW, side-by-side. All designing details of the FMSIW were presented there and will not be repeated here for the sake of simplicity. The same substrate with a dielectric constant of 4.3 and a thickness of 1.5mm is utilized here. Two rows of vias are used to mimic the functionality of the side walls of the conventional waveguide. Also, they operate to electrically connect the upper and lower conducting layers of the SIW. Previously, the miniaturization occurred when the FMSIW filter operated under the cutoff frequency exploiting the evanescent-mode technique. The miniaturization ratio is obtained once again in this chapter exploiting the magnetically symmetrical wall along the longitudinal side of the waveguide. This miniaturizes the FMSIW to half (i.e., 50% reduction) to convert it to the HMSIW, being the thesis key in this chapter. However, the goal in this thesis is to lower the resonance frequency, the drawback is that the HMSIW has larger radiation losses compared to the FMSIW. The wide-open side results in larger leakage of the guided electromagnetic signals as a radiation, thereby degrading the overall performance. Moreover, this radiation can be lowered to some extent if a row of vias is added to close the wide-open side, but it is out of the thesis scope. The fringing fields can extend from the wide-open side where more equivalent capacitance will be added, and then the resonant frequency will be slightly shifted down. The FMSIW supports the TE_{10} mode, while the HMSIW supports the $TE_{0.5,\,0}$ mode. The modes have the same characteristics of current distribution. The substrate used in the design plays a vital role in determining the cutoff frequency. As known, when the dielectric constant increases, the cutoff frequency of the waveguide decreases provided the structure dimensions should be kept the same.

4.2.1 Design of the FMSIW and HMSIW

To design HMSIW, we should use the formulas of FMSIW given in Eq. (2.15-2.19) to calculate all required dimensions depending primarily on the necessary cutoff frequency. Also, the type of substrate material determines the waveguide dimensions. According to Eq. (2.15), if the substrate is chosen, the waveguide width a_{equ} is the main parameter to determine the cutoff frequency. On contrast, the waveguide length does not change the cutoff frequency if it is changed.

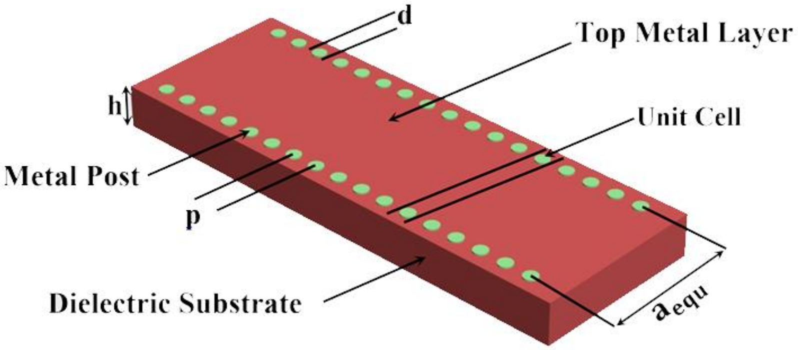

(a)

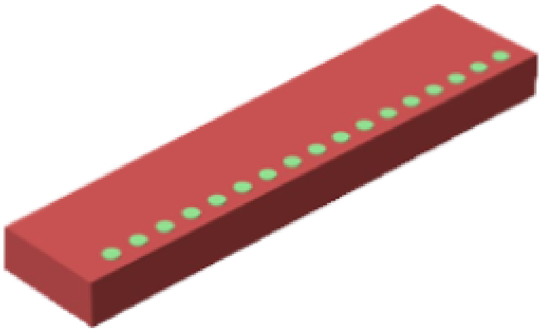

(b)

Figure 4.1 (a) The FMSIW structure and (b) the HMSIW structure

From Figure 4.1, a_{equ} denotes the distance between the two rows of vias, from a center of each via. The h is referred to the thickness of substrate, d is the diameter of the inserted copper vias, and p is the distance between the centers of each adjacent two vias on the same row.

After specifying the operating cutoff frequency and the substrate material, Dimensions of the FMSIW can be easily calculated using Eq. (2.15-2.19). Then, the Advanced System Design ADS software is used to electromagnetically analyze the FMSIW. Figure 4.2

shows the FMSIW and HMSIW with field distribution. As can be seen, when the FMSIW is cut from the center, the field remains undistributed due to the magnetic wall along the transmission path of the FMSIW. Also, the fringing fields are obvious, added extra little width, so the cutoff frequency will be slightly lowered. Figure 4.3 confirms effects of the fringing fields, since the cutoff frequency of the HMSIW (5.16GHz) is lower than the cutoff frequency of the FMSIW (5.33GHz). The transmission and reflection coefficients of the FMSIW and HMSIW are very close to each other and they show high pass filtering as in the conventional waveguides.

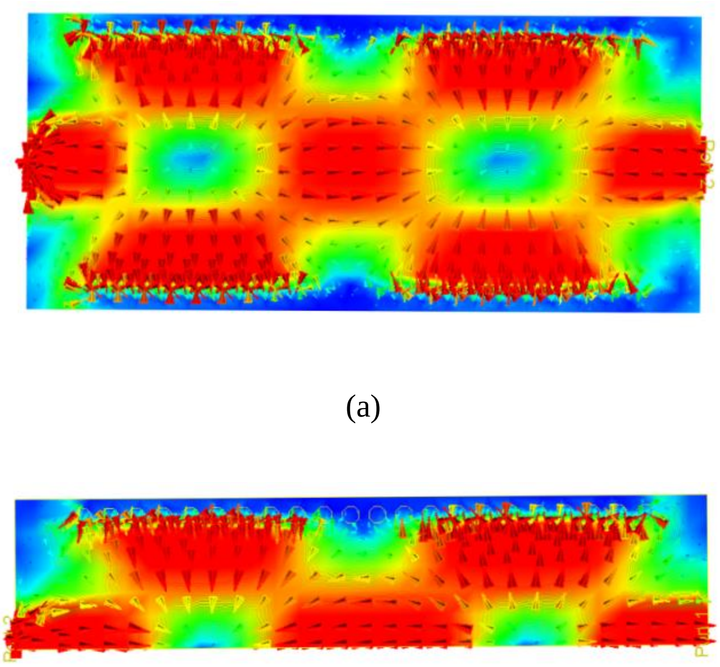

(a)

(b)

Figure 4.2 Field distribution in the (a) FMSIW and (b) HMSIW

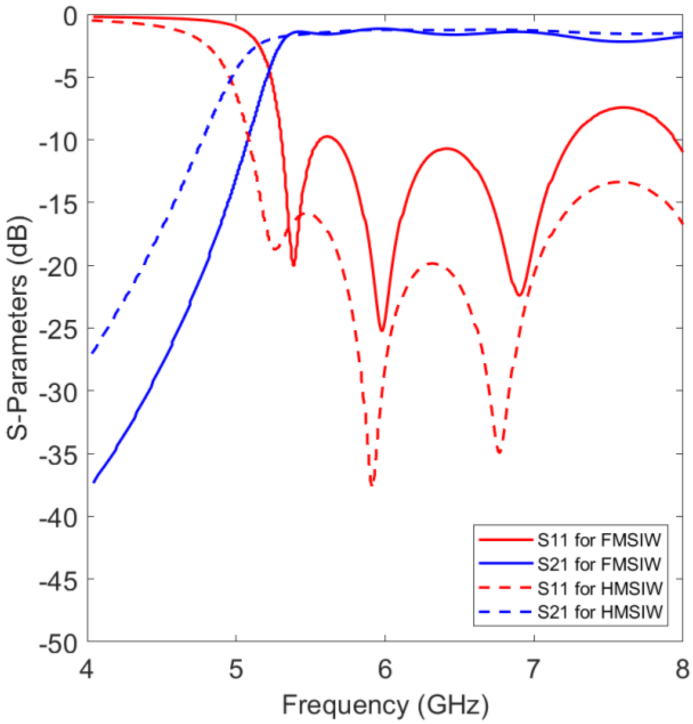

Figure 4.3 Comparison of S_{11} & S_{21} between the FMSIW and HMSIW

4.2.2 Design of the FMSIW and HMSIW Band pass Filter (FMSIW-BPF and HMSIW-BPF)

As demonstrated earlier, the FMSIW is converted to HMSIW by cutting it into two pieces along its longitudinal center, exploiting the magnetic wall property where the electric field will be the highest and the magnetic field is lowest. This leads into 50% miniaturization. Furthermore, the same procedure carried out in preceding chapter, the technique of evanescent-mode filter is applied again to make the proposed filter gets more miniaturization (i.e., more than 50%). For the sake of simplicity, the constitution parameters (i.e., the permittivity and permeability) and the propagation constants will not repeated here.

The structure of the 1st order FMSIW-BPF, also called the unit cell, is demonstrated in Figure 4.4. The slot is etched on the upper layer of the FMSIW. This slot aids to convert the evanescent-mode into propagation-mode by making the signs of the constitution parameters either negative (i.e., backward propagation) or positive (forward propagation). As shown in Figure 4.3, the cutoff frequency of the plain FMSIW is about 5.2GHz, and it typically operates above this frequency. As operating frequency increases, the mode number increases. When loading the slot, the frequency decreases into about 2.2GHz as illustrated in Figure 4.5.

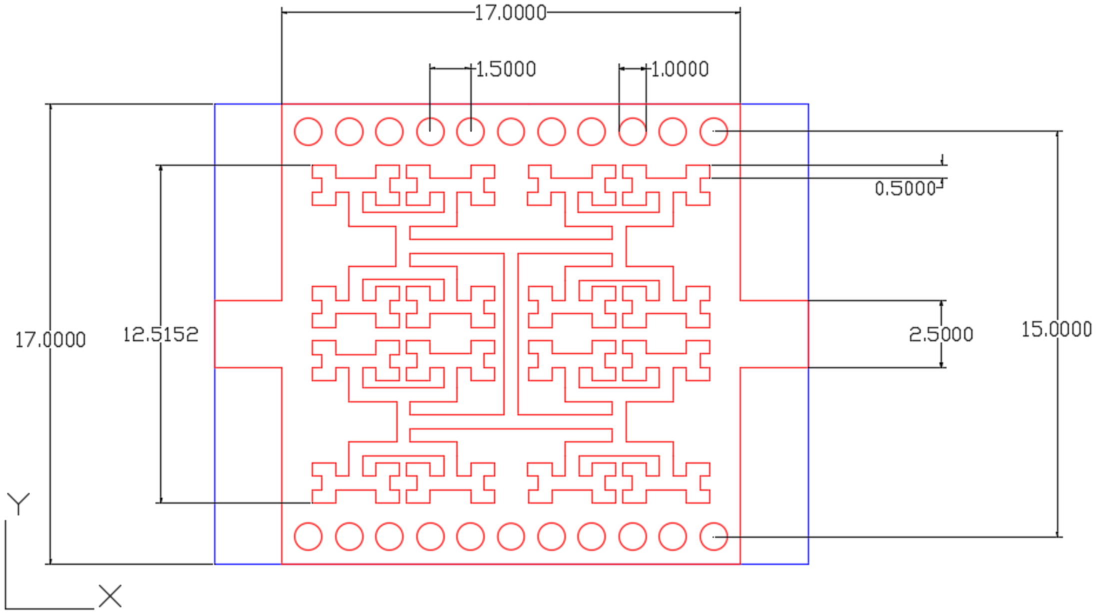

Figure 4.4 Structure of the 1st order FMSIW-BPF

The dimensions, which chosen according to the substrate mentioned above and the cutoff frequency 5.33GHz, are 17mm and 17mm for the width and length of the FMSIW, respectively. Also, the via diameter d =1mm, the distance between adjacent vias p =1.5mm, and the distance between the side sows from vias center a_{equ}=15mm.

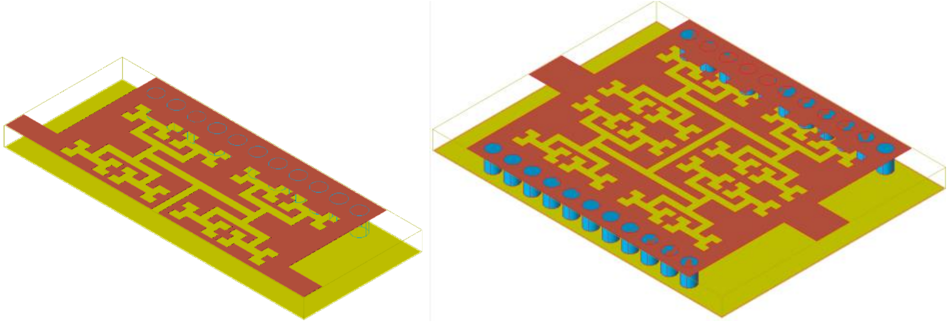

Figure 4.5 shows the 1st order of the (a) FMSIW BPF and (b) HMSIW BPF.

The ADS software is used to design and analyze them. The bandwidth is about 0.4GHz. The transmission losses are less than 1dB, and the reflection coefficient is about -40dB, as demonstrated in Figure 4.6. Also, the out-of-band rejection of the HMSIW-BPF is sharper than of its counter FMSIW-BPF. The interesting band has no ripple. Once again, the filter operates under the cutoff frequency to confirm the concept that says that evanescent-mode can be transformed into the propagation-mode. Figure 4.7 shows one order and high orders of the proposed HMSIW-BPF, being the 2nd, and 3rd order. The order number denotes a number of unit cells used in each filter. Not only the Hybrid I-H fractal slots are loaded into the upper layer of the FMSIW, but also other thick rectangular slots are added between any two adjacent fractal slots. These slots operate increase the coupling between the resonators (i.e., unit cells)

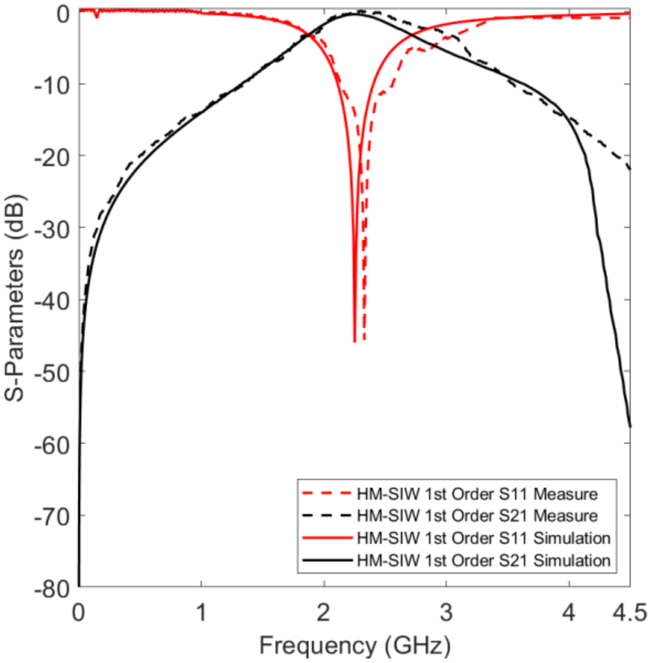

Figure 4.6. The transmission and reflection coefficients of HMSIW

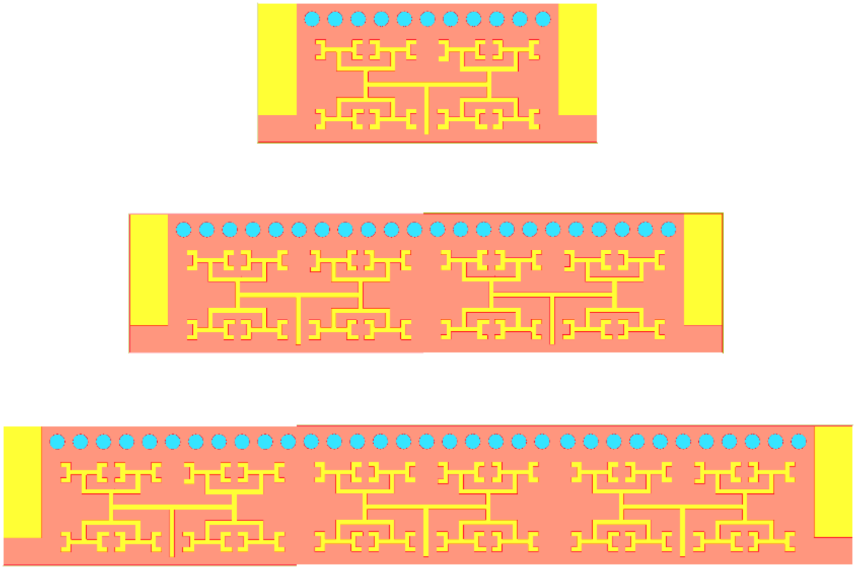

Figure 4.7 High orders of the proposed HMSIW-BPFs one stage, two stages, and three stages

4.3 Results and Discussions

To validate the proposed results, three types of the HMSIW BPFs (one stage, two stages, and three stages) are fabricated and tested using the vector network analyzer VNA. An FR4 substrate with $\varepsilon r = 4.3$ and a thickness of 1.5mm is used. Figure 4.8 shows a prototypes of the fabricated filters.

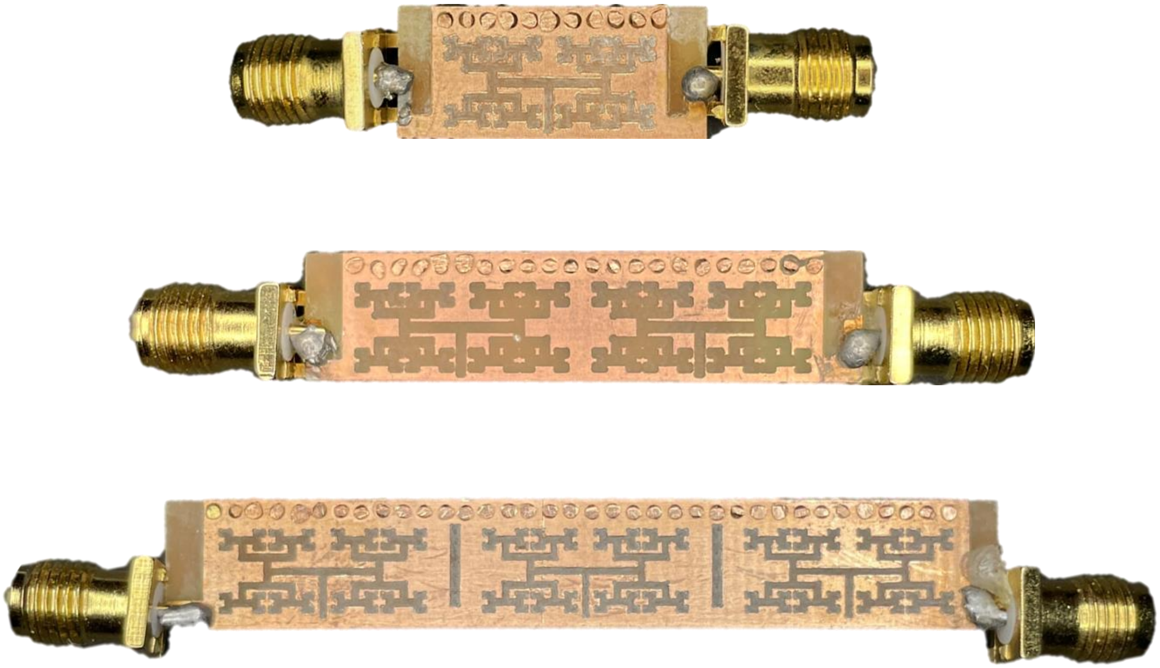

Figure 4.8 Prototypes of the fabrication of the proposed HMSIW-BPFs

Figure 4.9 portrays the comparisons between the simulation and measurement results. As can be seen, the matching between them is very well, but the slight differences belong for some reasons such as the fabrication errors, losses of the SMA connectors, and the software ideality. Moreover, Figure 4.10 (a) shows the simulated transmission coefficients S_{21} for all proposed HMSIW-BPFs and Figure 10 (b) shows the simulated reflection coefficients S11 for the same filters.

The 1st order HMSIW-BPF offers a good response, where the filtering bandwidth extends from 1.9GHz to 2.7GHz, covering all wireless ISM application (2.4GHz). At resonance, the insertion and return losses are about 1.2dB and 40dB, respectively, for both the simulated and measured results. A good rejection which is less than 40dB is obvious when exceeding 4GHz. The simulation and measured results are also shown, and they are very good in regard of the insertion and return losses. As an order increases, the pass band becomes more flat and the rejection skirt becomes sharper.

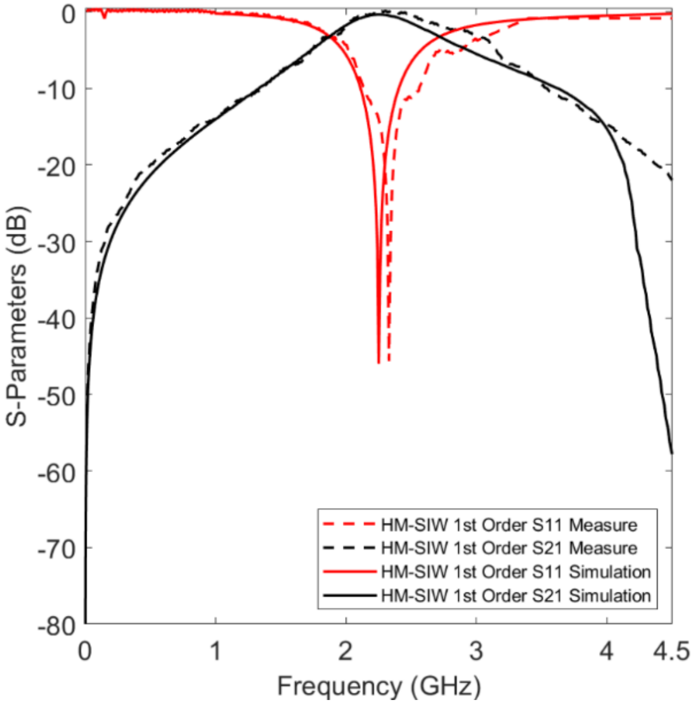

(a)

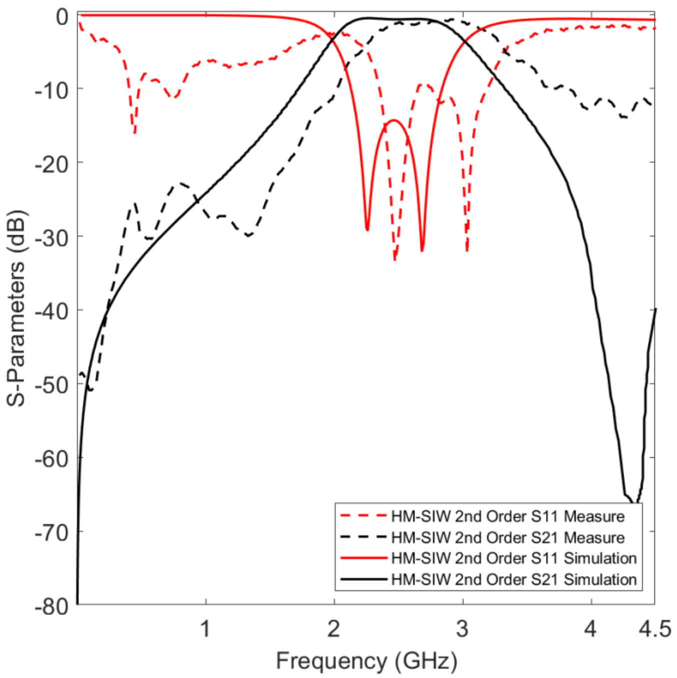

(b)

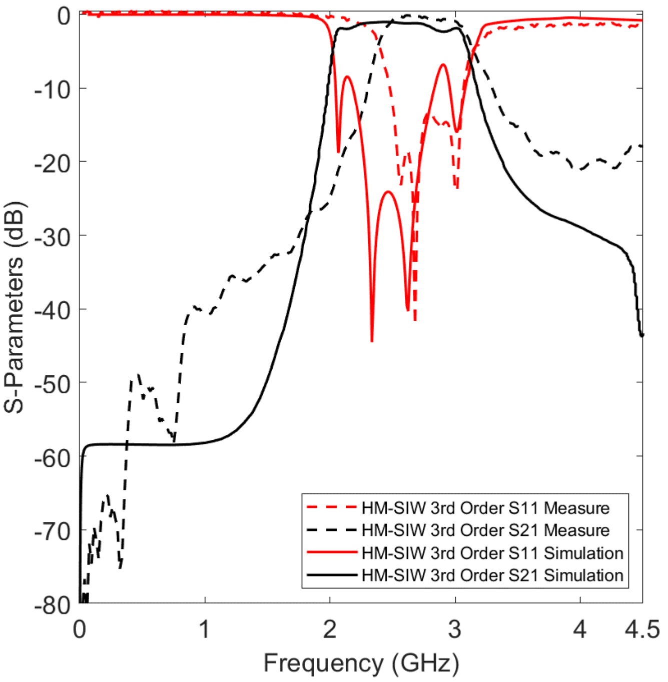

(c)

Figure 4.9 Comparison between results of the simulation and measurement of the proposed HMSIW-PBFs: (a) 1st order, (b) 2nd order, (c) 3rd order

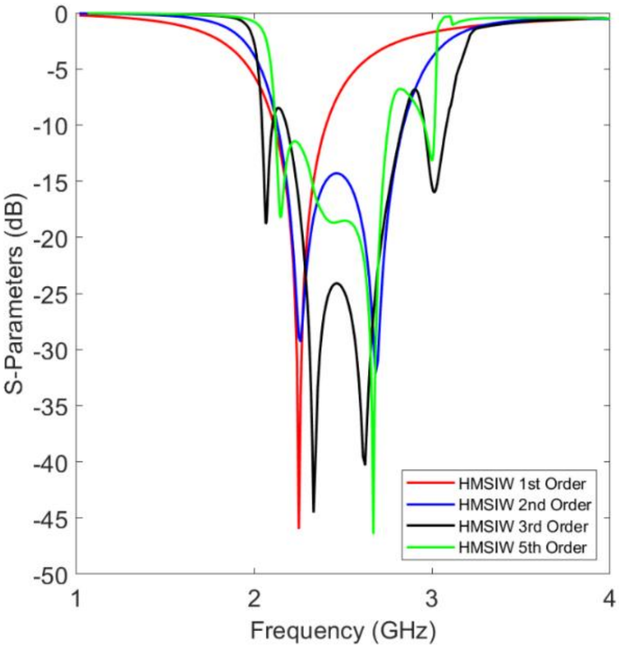

a)

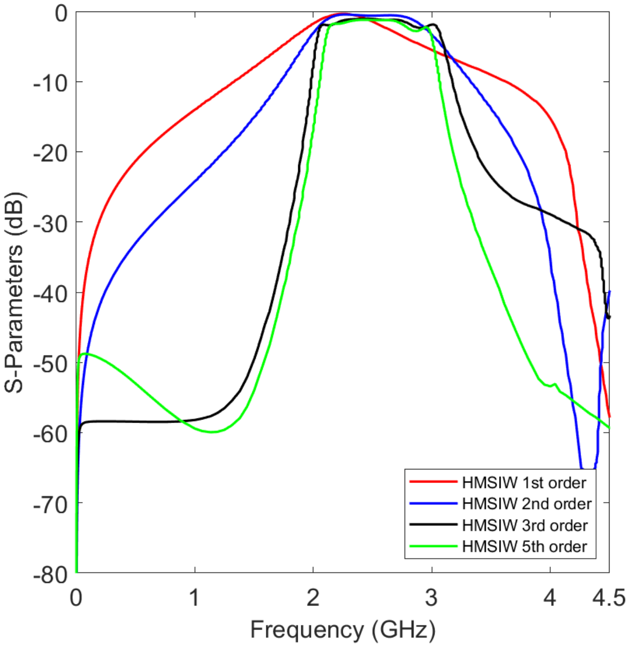

b)

Figure 4.10 Comparison among the simulation results of four orders of the proposed HMSIW-BPFs :(a) is the S_{11}, (b) is the S_{21}

The main key is that should be mentioned that all the proposed filters operate under the cutoff frequency of the half-mode of the waveguide, thanks to loading the fractal slots to SIW structures which converts the evanescent-mode into propagation one. Also, the half-mode property offers extra miniaturizations. Table 4.1 reports a comparison between our proposed work and the thesis efforts found in the literature under the same topic. One can see that our proposed work has many advantages over others.

Table 4.1: Comparison with the works in the same filed in the previous literature

References	Year	F_o (GHz)	RL/IL (dB)	Technique used	3-dB FBW (%)	Dimensions (mm)
[6]	2020	5.3	-23/-0.75	H-shaped fractal SIW-metamaterial	12.5	8X7.5
[33]	2016	5	-15/-1.8	EBG loaded on HMSIW	7.6	22.2 X 9
[50]	2022	5.2	-14.5/-1.1	HMSIW with DGS and CSRR	26.3	27.8 X 7.25
[29]	2011	1.13	-11.8/-0.8	HMSIW Cross shaped fractal	4.3	21.6 X 13.1
[38]	2018	12	-35/-0.56	HMSIW-SPP	5.1	60 X 18
This work	2023	2	-40/-1.2	HMSIW 1st order fractal shaped	11.5	17 X 9

The comparison in Table 4.1 shows that proposed work have a higher matching when compared with the others, where having the best value of return loss which about -40dB, and the insertion loss is -1.2dB, the fractional bandwidth FBW is about 11.5%, where this indicates the wideband was achieved and it was a credit added to this work, highly miniaturization in dimensions with compare it with the others, where the proposed filter working at the frequency 2GHz and its dimensions was less than the others which working in higher frequencies.

CHAPTER FIVE

CONCLUSION AND FUTURE WORKS

5.1 Conclusion

In this thesis, two groups of families have been introduced. The first group was presented in Chapter 3, being called the FMSIW bandpass filters. This type of filters was designed using unit cells introduced earlier in the same chapter. The FMSIW combined advantages of both printed circuits and conventional rectangular waveguides. Also, the conventional waveguide operates above the cutoff frequency, but the proposed designs were operating under the cutoff frequency, thanks to the metamaterial technology. The cutoff frequency was 5.2GHz, but the operating frequency was 2GHz with a miniaturization ratio equal to 60% when utilizing the 3rd iteration fractal curves which are cut out of the upper layer of the SIW. The most important parameters, such as the permittivity, permeability, and propagation constant, were determined to examine if the proposed filters were evanescent-mode bandpass filters. Findings have showed that unit cells supported both backward and forward propagation modes before and after 2GHz, respectively, and these two modes were very close to each other with no frequency gap to form one wideband. Then, the HMSIW bandpass filters were introduced in Chapter 4 exploiting the symmetry around the magnetic wall of waveguide.

Chapter 3 introduced the proposed 1stand 3rd order bandpass filters where these filters were designed, simulated, and fabricated utilizing the Agilent Design software ADS. The simulated results were in very good agreement with the measurements. The results showed that the filter had low losses compared to ones in the literature. The S21s were close to 0dB and the S11s were less than –10dB for most filters. The transmission phases were almost linear, so the group delays were almost constant, thereby introducing less distortion within the transmission bands. As demonstrated in the thesis, Hybrid I-H fractal iteration has played a vital role in determining the resonance frequency of the proposed bandpass filters, so the third iteration was chosen because of introducing the lowest resonance frequency.

Then, the FMSIW filters were converted to their HMSIW counterparts with pertaining almost the same features introduced in the FMSIW filters. Along the longitudinal central line of the SIW, the cut was made exploiting the magnetic symmetry line. Three filters had been designed, simulated, fabricated, and measured. Almost all the simulated and measured results were in good agreement. The proposed designs were miniaturized to 50% if they are compared to their FMSIW counterparts which are introduced in Chapter 3. The most important one finding for the HMSIW filters was the losses due to the open edge of the SIW. These losses can be lowered if a row of vias is used to keep the radiation low as much as possible.

5.2 Future works

This section introduces all the expected works in the future related to the work presented in this thesis.

- Reducing the losses especially for the HMSIW filters using the row of vias
- Using two sizes of fractal slots in the same design to design dual band bandpass filters
- Combining two filters with different bands to create the frequency duplexer
- Using the LTCC technology to build multi-layer SIW to reduce the overall size or to have multi-band filters
- Combining tow filters with the same frequency to design the power combiner with the frequency selectivity filters

References:

[1] Shigeki, F. (1994). Waveguide line. Japan Patent, 6053711.

[2] Wu, K., Deslandes, D., & Cassivi, Y. (2003, October). The substrate integrated circuits-a new concept for high-frequency electronics and optoelectronics. In 6th International Conference on Telecommunications in Modern Satellite, Cable and Broadcasting Service, 2003. TELSIKS 2003. (Vol. 1, pp. P-III). IEEE..

[3] Wu, K. (2001, December). Integration and interconnect techniques of planar and non-planar structures for microwave and millimeter-wave circuits-current status and future trend. In APMC 2001. 2001 Asia-Pacific Microwave Conference (Cat. No. 01TH8577) (Vol. 2, pp. 411-416). IEEE.

[4]Bozzi, M., Georgiadis, A., & Wu, K. (2011). Review of substrate-integrated waveguide circuits and antennas. IET Microwaves, Antennas & Propagation, 5(8), 909-920.

[5] Che, W., Li, C., Zhang, D., & Chow, Y. L. (2010). Investigations on propagation and the band broadening effect of ridged rectangular waveguide integrated in a multilayer dielectric substrate. IET Microwaves, Antennas & Propagation, 4(6), 674-684..

[6] Kumar, R., & Singh, S. N. (2019). Design and analysis of ridge substrate integrated waveguide bandpass filter with octagonal complementary split ring resonator for suppression of higher order harmonics. Progress In Electromagnetics Research C, 89, 87-99.

[7] Lai, Q., Fumeaux, C., Hong, W., & Vahldieck, R. (2009). Characterization of the propagation properties of the half-mode substrate integrated waveguide. IEEE Transactions on Microwave Theory and Techniques, 57(8), 1996-2004.

[8] Hong, W., Liu, B., Wang, Y., Lai, Q., Tang, H., Yin, X. X., ... & Wu, K. (2006, September). Half mode substrate integrated waveguide: A new guided wave structure for microwave and millimeter wave application. In 2006 Joint 31st International Conference on Infrared Millimeter Waves and 14th International Conference on Teraherz Electronics (pp. 219-219). IEEE..

[9] Dong, Y., & Itoh, T. (2010). Composite right/left-handed substrate integrated waveguide and half mode substrate integrated waveguide leaky-wave structures. IEEE Transactions on Antennas and Propagation, 59(3), 767-775.

[10] Huang, X. L., Zhou, L., Völkel, M., Hagelauer, A., Mao, J. F., & Weigel, R. (2018). Design of a novel quarter-mode substrate-integrated waveguide filter with multiple transmission zeros and higher mode suppressions. IEEE Transactions on Microwave Theory and Techniques, 66(12), 5573-5584.

[11] Huang, X. L., Zhou, L., Völkel, M., Hagelauer, A., Mao, J. F., & Weigel, R. (2018). Design of a novel quarter-mode substrate-integrated waveguide filter with multiple transmission zeros and higher mode suppressions. IEEE Transactions on Microwave Theory and Techniques, 66(12), 5573-5584.

[12] Kim, D. W., & Lee, J. H. (2004). A partial H-plane waveguide as a new type of compact waveguide. Microwave and Optical Technology Letters, 43(5), 426-428.

[13] Moro, R., Moscato, S., Bozzi, M., & Perregrini, L. (2015). Substrate integrated folded waveguide filter with out-of-band rejection controlled by resonant-mode suppression. IEEE Microwave and Wireless Components Letters, 25(4), 214-216.

[14] Musallam, M., Bener, A., Zirie, M., Al-Gaud, Y. K., Al-Hamaq, A., Othman, M., & Tewfik, I. (2008). Metabolic syndrome and its components among Qatari population. International Journal of Food Safety, Nutrition and Public Health, 1(1), 88-102.

[15] Dong, Y. D., Yang, T., & Itoh, T. (2009). Substrate integrated waveguide loaded by complementary split-ring resonators and its applications to miniaturized waveguide filters. IEEE Transactions on Microwave Theory and Techniques, 57(9), 2211-2223.

[16] V. G. Veselago. The electrodynamics of substances with simultaneously negative values of ε and μ. Soviet Physics USPEKHI, vol. 10, no. 14, pp. 509–514. January-February 1968

[17] Solymar, L., & Shamonina, E. (2009). Waves in metamaterials. Oxford University Press.

[18] Keshavarz, R., & Shariati, N. (2020, November). Low profile metamaterial band-pass filter loaded with 4-turn complementary spiral resonator for WPT applications. In 2020 27th IEEE International Conference on Electronics, Circuits and Systems (ICECS) (pp. 1-4). IEEE.

[19] Keshavarz, S., Abdipour, A., Mohammadi, A., & Keshavarz, R. (2019). Design and implementation of low loss and compact microstrip triplexer using CSRR loaded coupled lines. AEU-International Journal of Electronics and Communications, 111, 152913.

[20] Karthikeyan, S. S., & Kshetrimayum, R. S. (2009). Harmonic suppression of parallel coupled microstrip line bandpass filter using CSRR. Progress In Electromagnetics Research Letters, 7, 193-201.

[21] Liu, B., Hong, W., Zhang, Y., Tang, H. J., Yin, X., & Wu, K. (2007). Half mode substrate integrated waveguide 180 3-dB directional couplers. IEEE Transactions on Microwave Theory and Techniques, 55(12), 2586-2592.

[22] Liu, J. P., Lv, Z. Q., & An, X. (2016). Compact substrate integrated waveguide filter using dual-plane resonant cells. Microwave and Optical Technology Letters, 58(1), 111-114.

[23] Mansouri, B., Abri, M., Rabah, M. A., Tao, J., & Vuong, T. H. (2015). SIW bandpass filter screens S-band signals. Microwaves & RF.

[24] Parameswaran, A., Athira, P., & Raghavan, S. (2018). Miniaturizing SIW filters with slow wave technique. AEU-International Journal of Electronics and Communications, 84, 360-365.

[25] Liu, B., Hong, W., Zhang, Y., Tang, H. J., Yin, X., & Wu, K. (2007). Half mode substrate integrated waveguide 180 3-dB directional couplers. IEEE Transactions on Microwave Theory and Techniques, 55(12), 2586-2592.

[26] Dong, Y. D., & Itoh, T. (2009, June). Composite right/left-handed substrate integrated waveguide and half-mode substrate integrated waveguide. In 2009 IEEE MTT-S International Microwave Symposium Digest (pp. 49-52). IEEE.

[27] Duran-Sindreu, M., Bonache, J., Martin, F., & Itoh, T. (2013). Single-layer fully-planar extended-composite right-/left-handed transmission lines based on substrate

integrated waveguides for dual-band and quad-band applications. International Journal of Microwave and Wireless Technologies, 5(3), 213-220.

[28] Yang, T., Chi, P. L., Xu, R., & Lin, W. (2012). Folded Substrate Integrated Waveguide Based Composite Right/Left-Handed Transmission Line and Its Application to Partial $ H $-Plane Filters. IEEE transactions on microwave theory and techniques, 61(2), 789-799.

[29] Institute of Electrical and Electronics Engineers. (n.d.). Wireless and Microwave Technology Conference (WAMICON), 2011 IEEE 12th Annual : date: 18-19 April 2011.

[30] Metamaterial Based Compact Band Pass Filter (BPF) Design in UHF Range FRACTIONAL CALCULUS IN CONDENSE MATTER PHYSICS View project Application of Fractional Calculus View project Metamaterial Based Compact Band Pass Filter (BPF) Design in UHF Range, 17 Asian Journal of physics 1 (2012). https://www.researchgate.net/publication/323186170.

[31] de Dios Ruiz, J., Martı, F. L., Alvarez-Melcon, A., & Hinojosa, J. (2015). Substrate integrated waveguide (SIW) with Koch fractal electromagnetic bandgap structures (KFEBG) for bandpass filter design. IEEE Microwave and Wireless Components Letters, 25(3), 160-162.

[32] Coves, A., Torregrosa-Penalva, G., San-Blas, A. A., Sanchez-Soriano, M. A., Martellosio, A., Bronchalo, E., & Bozzi, M. (2016). A novel band-pass filter based on a periodically drilled SIW structure. Radio Science, 51(4), 328-336.

[33] Jia, D., Feng, Q., Xiang, Q., & Wu, K. (2016). Multilayer substrate integrated waveguide (SIW) filters with higher-order mode suppression. IEEE Microwave and Wireless Components Letters, 26(9), 678-680.

[34] Hammas, H. A. (2018). Design of compact multiband microstrip BPF based on fractal open-ring configuration. Engineering and Technology Journal, 36(8 Part A).

[35] Li, Y., Sim, C. Y. D., Luo, Y., & Yang, G. (2019). Metal-frame-integrated eight-element multiple-input multiple-output antenna array in the long term evolution bands 41/42/43 for fifth generation smartphones. International Journal of RF and Microwave Computer-Aided Engineering, 29(1), e21495.

[36] Wei, F., Yue, H. J., Song, J. P., Kang, H. Y., & Li, B. (2018). Half-mode SIW BPF loaded with S-shaped complementary spiral resonators. Progress In Electromagnetics Research Letters, 77, 13-18.

[37] Vicent, G., Bronchalo, E., Coves, A., & Torregrosa, G. (2018, February). Artificial high effective permittivity medium in a SIW filled with metallic cylinders. In Journal of Physics: Conference Series (Vol. 963, No. 1, p. 012001). IOP Publishing.

[38] Guan, D. F., You, P., Zhang, Q., Yang, Z. B., Liu, H., & Yong, S. W. (2018). Slow-wave half-mode substrate integrated waveguide using spoof surface plasmon polariton structure. IEEE Transactions on Microwave Theory and Techniques, 66(6), 2946-2952.

[39] Moitra, S., Dey, R., & Ghosh, C. K. (2019). Angular bend half mode substrate integrated waveguide (HMSIW) based band-pass filter with multiple transmission zeroes. Wireless Personal Communications, 104(1), 259-267.

[40] Troudi, Z., & Osman, L. (2019, October). Design of miniaturized half mode SIW bandpass filter using metamaterial unit cell. In 2019 IEEE 19th Mediterranean Microwave Symposium (MMS) (pp. 1-4). IEEE.41]] Noura, A., Benaissa, M., Abri, M., Badaoui, H., Vuong, T. H., & Tao, J. (2019). Miniaturized half-mode SIW band-pass filter design integrating dumbbell DGS cells. Microwave and optical technology letters, 61(6), 1473-1477.

[42] Chaudhury, S. S., Awasthi, S., & Singh, R. K. (2020). Dual band bandpass filter based on substrate integrated waveguide loaded with mushroom resonators. Microwave and Optical Technology Letters, 62(6), 2226-2235.

[43] Han, Y. K., Deng, H. W., Zhu, J. M., Xing, S. B., & Han, W. (2021). Compact dual-band dual-mode SIW balanced BPF with intrinsic common-mode suppression. IEEE Microwave and Wireless Components Letters, 31(2), 101-104.

[44] Jiang, Y., Liu, B., Huang, Z., Wang, Q., Wang, C., Zhang, X., & Yuan, N. (2021, August). Design of Compact Wideband BPF Based on DGS-HMSIW. In 2021 International Applied Computational Electromagnetics Society Symposium (ACES) (pp. 1-3). IEEE.

[45] Boubakar, H., Abri, M., & Benaissa, M. (2021). Design of complementary hexagonal metamaterial based HMSIW band-pass filter and reconfigurable SIW filter using PIN diodes. Advanced Electromagnetics, 10(2), 19-26.

[46] Troudi, Z., Machac, J., & Osman, L. (2021). A Novel Compact Substrate Integrated Waveguide Filter Using Miniaturized Stepped Impedance Metamaterial Unit Cell. Progress In Electromagnetics Research C, 108, 49-61.

[47] Abbasian, E., & Gholipour, M. (2021). Design of a Schmitt-trigger-based 7T SRAM cell for variation resilient low-energy consumption and reliable internet of things applications. AEU-International Journal of Electronics and Communications, 138, 153899.

[48] Boubakar, H., Abri, M., Akram, A., Benaissa, M., & Ahmad, S. (2022, December). HMSIW Miniaturized Bandpass Filter Loaded with Two Elliptic Complementary Split-Ring Resonators for S-Band Applications. In 2022 International Conference on Emerging Trends in Electrical, Control, and Telecommunication Engineering (ETECTE) (pp. 1-4). IEEE.

[49] Cherif, N., Abri, M., Ahmad, S., Ghaffar, A., Khial, C., Benzerga, F., ... & Roumeiça, B. (2022). Miniaturizing Bandpass Filter Based on Half-Mode SIW for Sub-mm 5G Applications. Progress in Electromagnetics Research Letters, 104.

[50] Muchhal, N., Elkhouly, M., Vintimilla, R. Z., Chakraborty, A., & Srivastava, S. (2022, November). Design of Hybrid Fractal Integrated Half Mode SIW Band Pass Filter with CSRR and Minkowski Defected Ground Structure for Sub-6 GHz 5G Applications. In Photonics (Vol. 9, No. 12, p. 898). MDPI.

[51] Hong, J. S. G., & Lancaster, M. J. (2004). Microstrip filters for RF/microwave applications. John Wiley & Sons..

[52] Pozar, D. M. (2005). Microwave Engineering, Chapter 8. John Wiley & Sons, Hoboken, New Jersey, 3, 91-93..

[53] Matthaei, G. (1980). Microwave filters, impedance-matching networks and coupling structures. Artech House Book, 775-809.

[54] Collin, R. E. (2007). Foundations for microwave engineering. John Wiley & Sons.

[55] Pozar, D. M. (2011). Microwave engineering. John wiley & sons.

[56] Pozar, D. M. (1990). Microwave Engineering Reading. vol. MA: Addison-Wesley.

[57] Hunter, I. (2001). Theory and design of microwave filters (No. 48). Iet.

[58] Deslandes, D., & Wu, K. (2001). Integrated microstrip and rectangular waveguide in planar form. IEEE microwave and wireless components letters, 11(2), 68-7059] .] Xu, F., & Wu, K. (2005). Guided-wave and leakage characteristics of substrate integrated waveguide. IEEE Transactions on microwave theory and techniques, 53(1), 66-73.

[60] Bozzi, M., Perregrini, L., Wu, K., & Arcioni, P. (2009). Current and future research trends in substrate integrated waveguide technology. Radioengineering, 18(2).

[61] Kumar, H., Jadhav, R., & Ranade, S. (2012). A review on substrate integrated waveguide and its microstrip interconnect. Journal of Electronics and Communication Engineering, 3(5), 36-40.

[62] Cassivi, Y., Perregrini, L., Arcioni, P., Bressan, M., Wu, K., & Conciauro, G. (2002). Dispersion characteristics of substrate integrated rectangular waveguide. IEEE Microwave and Wireless components letters, 12(9), 333-335.

[63] Torres-Torres, R., Romo, G., Horine, B., Sachez, A., & Heck, H. (2006, October). Full characterization of substrate integrated waveguides from S-parameter measurements. In 2006 IEEE Electrical Performane of Electronic Packaging (pp. 277-280). IEEE.

[64] Díaz Caballero, E., Miralles, E., Esteban González, H., Belenguer Martínez, Á., Boria Esbert, V. E., Bachiller Martin, M. C., ... & Lucas Borja, A. (2011). Efficient and Accurate Design of Passive Devices in Substrate Integrated Waveguide Technology and their Tapered Transitions from Microstrip Lines. In Waves (Vol. 3, pp. 76-85).

[65] Kumar, H., Jadhav, R., & Ranade, S. (2012). A review on substrate integrated waveguide and its microstrip interconnect. Journal of Electronics and Communication Engineering, 3(5), 36-40.

[66] Lou, Y., Chan, C. H., & Xue, Q. (2008). An in-line waveguide-to-microstrip transition using radial-shaped probe. IEEE Microwave and Wireless Components Letters, 18(5), 311-313.

[67] Grabherr, W., Huder, W. G. B., & Menzel, W. (1994). Microstrip to waveguide transition compatible with mm-wave integrated circuits. IEEE transactions on microwave theory and techniques, 42(9), 1842-1843.

[68] Villegas, F. J., Stones, D. I., & Hung, H. A. (1999). A novel waveguide-to-microstrip transition for millimeter-wave module applications. IEEE transactions on microwave theory and techniques, 47(1), 48-55.

[69] Kaneda, N., Qian, Y., & Itoh, T. (1999). A broad-band microstrip-to-waveguide transition using quasi-Yagi antenna. IEEE transactions on Microwave Theory and Techniques, 47(12), 2562-2567.70]] Huang, T. Y., Shen, T. M., & Wu, R. B. (2010). Design and modeling of microstrip line to substrate integrated waveguide transitions. Passive Microwave Components and Antennas, 11, 225-246.

[71] Wu, K., Deslandes, D., & Cassivi, Y. (2003, October). The substrate integrated circuits-a new concept for high-frequency electronics and optoelectronics. In 6th International Conference on Telecommunications in Modern Satellite, Cable and Broadcasting Service, 2003. TELSIKS 2003. (Vol. 1, pp. P-III). IEEE.

[72] Deslandes, D., & Wu, K. (2001, May). Integrated transition of coplanar to rectangular waveguides. In 2001 IEEE MTT-S International Microwave Sympsoium Digest (Cat. No. 01CH37157) (Vol. 2, pp. 619-622). IEEE.

[73] Hong, W., Liu, B., Wang, Y., Lai, Q., Tang, H., Yin, X. X., ... & Wu, K. (2006, September). Half mode substrate integrated waveguide: A new guided wave structure for microwave and millimeter wave application. In 2006 Joint 31st International Conference on Infrared Millimeter Waves and 14th International Conference on Teraherz Electronics (pp. 219-219). IEEE.

[74] Lai, Q., Fumeaux, C., Hong, W., & Vahldieck, R. (2009). Characterization of the propagation properties of the half-mode substrate integrated waveguide. IEEE Transactions on Microwave Theory and Techniques, 57(8), 1996-2004.

[75] C. Caloz, C., & Itoh, T. (2006). ELECTROMAGNETIC METAMATERIALS: TRANSMISSION LINE THEORY AND MICROWAVE APPLICATIONS The Engineering Approach PREFACE.

[76] Eleftheriades, G. V., & Balmain, K. G. (2005). Negative-refraction metamaterials: fundamental principles and applications. John Wiley & Sons.

[77] Abdalla, M. A. A. (2008). Ferrite left-handed meta-materials for RF microwave applications. The University of Manchester (United Kingdom).

[78] Viktor, G. V. (1968). The electrodynamics of substances with simultaneously negative values of $\epsilon $ and M. Soviet Physics Uspekhi, 10(4), 509-514.

[79] Smith, D. R., Padilla, W. J., Vier, D. C., Nemat-Nasser, S. C., & Schultz, S. (2000). Composite medium with simultaneously negative permeability and permittivity. Physical review letters, 84(18), 4184.

[80] Pendry, J. B., Holden, A. J., Robbins, D. J., & Stewart, W. J. (1999). Magnetism from conductors and enhanced nonlinear phenomena. IEEE transactions on microwave theory and techniques, 47(11), 2075-2084.

[81] Pendry, J. B., Holden, A. J., Robbins, D. J., & Stewart, W. J. (1998). Low frequency plasmons in thin-wire structures. Journal of Physics: Condensed Matter, 10(22), 4785.

[82] Caloz, C., & Itoh, T. (2003, June). Novel microwave devices and structures based on the transmission line approach of meta-materials. In IEEE MTT-S International Microwave Symposium Digest, 2003 (Vol. 1, pp. 195-198). IEEE.

[83] Caloz, C., & Itoh, T. (2004). Transmission line approach of left-handed (LH) materials and microstrip implementation of an artificial LH transmission line. IEEE Transactions on Antennas and propagation, 52(5), 1159-1166.

[84] C. Caloz and T. Itoh, "Application of the transmission line theory of left-handed (LH) materials to the realization of a microstrip "LH line"," in Antennas and Propagation Society International Symposium, 2002. IEEE, 2002, vol. 2, pp. 412-415 vol.2.

[85] Kahng, S., & Ju, J. (2008, April). Design of the UWB bandPass filter based on the 1 cell of microstrip CRLH-TL. In 2008 International Conference on Microwave and Millimeter Wave Technology (Vol. 1, pp. 69-72). IEEE.

[86] Studniberg, M., & Eleftheriades, G. V. (2008). A dual-band bandpass filter based on generalized negative-refractive-index transmission-lines. IEEE Microwave and Wireless Components Letters, 19(1), 18-20.

[87] Tolani, H., Eberspächer, M. A., & Eibert, T. F. (2010, November). Composite right/left-handed leaky wave antenna with structurally non-periodic unit cell arrangement. In 2010 Loughborough Antennas & Propagation Conference (pp. 165-168). IEEE. [88] Mandelbrot, B. B., & Mandelbrot, B. B. (1982). The fractal geometry of nature (Vol. 1). New York: WH freeman.

[89] Hutchinson, J. E. (1981). Fractals and self-similarity. Indiana University Mathematics Journal, 30(5), 713-747.

[90] Gupta, P., & Raina, J. P. S. Miniaturization of Antenna Using Fractals.

[91] Sardar, Z., & Abrams, I. (2004). Introducing chaos: A graphic guide. Icon Books.

[92] Sornette, D. (2006). Critical phenomena in natural sciences: chaos, fractals, selforganization and disorder: concepts and tools. Springer Science & Business Media.

[93] Addison, P. S. (1997). Fractals and chaos: an illustrated course. CRC Press.

[94] Barnsley, M. F. (1993). Fractals Everywhere Second Edition, Iterated Systems. Inc., Atlanta, Georgia.

[95] Geng, W., & Geng, W. (2010). Computer-assisted Cartoon Animation by Traditional Production Pipeline. The Algorithms and Principles of Non-photorealistic Graphics: Artistic Rendering and Cartoon Animation, 263-292.

[96] Birken, M., & Coon, A. C. (2008). Discovering patterns in mathematics and poetry. Brill.

[97] Romm, F. (2004). Microporous media: synthesis, properties, and modeling (Vol. 120). CRC Press.

[98] Plummer, T. (2009). Forecasting financial markets: the psychology of successful investing. Kogan Page Publishers.

[99] Ghosh, B., Sinha, S. N., & Kartikeyan, M. V. (2014). Fractal Apertures in Waveguides, Conducting Screens and Cavities. Springer Series in Optical Sciences, 187.

[100] Edgar, G. A., & Edgar, G. A. (2008). Measure, topology, and fractal geometry (Vol. 2). New York: Springer.

[101] Krzysztofik, W. J. (2013). Fractal Geometry in Electromagnetics Applications-from Antenna to Metamaterials. Microwave Review, 19(2).

[102] Tiwari, A., Rattan, M., & Gupta, I. (2014). Review on: fractal antenna design geometries and its applications. International Journal of Engineering and computer science, 3(9), 8270-8275.

[103] Puente-Baliarda, C., Romeu, J., Pous, R., & Cardama, A. (1998). On the behavior of the Sierpinski multiband fractal antenna. IEEE Transactions on Antennas and propagation, 46(4), 517-524.

[104] Bozzi, M., Georgiadis, A., & Wu, K. (2011). Review of substrate-integrated waveguide circuits and antennas. IET Microwaves, Antennas & Propagation, 5(8), 909-920.

[105] Peano, G., & Peano, G. (1990). Sur une courbe, qui remplit toute une aire plane (pp. 71-75). Springer Vienna.

[106] Palandoken, M., & Henke, H. (2010, March). Fractal negative-epsilon metamaterial. In 2010 International Workshop on Antenna Technology (iWAT) (pp. 1-4). IEEE.

[107]Romeu, J., & Rahmat-Samii, Y. (2000). Fractal FSS: A novel dual-band frequency selective surface. IEEE Transactions on antennas and propagation, 48(7), 1097-1105.

[108] Bao, X. L., Ruvio, G., Ammann, M. J., & John, M. (2006). A novel GPS patch antenna on a fractal hi-impedance surface substrate. IEEE Antennas and Wireless Propagation Letters, 5, 323-326.

[109] Murad, N. A., Esa, M., Yusoff, M. F. M., & Ali, S. H. A. (2006, September). Hilbert curve fractal antenna for RFID application. In 2006 international RF and microwave conference (pp. 182-186). IEEE.

[110] Keshavarz, S., Abdipour, A., Mohammadi, A., & Keshavarz, R. (2019). Design and implementation of low loss and compact microstrip triplexer using CSRR loaded coupled lines. AEU-International Journal of Electronics and Communications, 111, 152913.

[111] Dong, Y. D., Yang, T., & Itoh, T. (2009). Substrate integrated waveguide loaded by complementary split-ring resonators and its applications to miniaturized waveguide filters. IEEE Transactions on Microwave Theory and Techniques, 57(9), 2211-2223.

[112] García-García, J., Bonache, J., Gil, I., Martín, F., Velazquez-Ahumada, M. C., & Martel, J. (2006). Miniaturized microstrip and CPW filters using coupled metamaterial resonators. IEEE Transactions on Microwave Theory and Techniques, 54(6), 2628-2635.

[113]Jia-Sheng, H., & Lancaster, M. J. (2001). Microstrip filters for RF/microwave applications. New York: John Wiley&Sond. Inc, 235-272.

List of Publications

Paper No.	**Paper Title**	**Paper Status**
1	Miniaturized Band Pass Filter using Metamaterial Half Mode technique for Substrate Integrated Waveguide	Accepted
2	Miniaturization of Substrate Integrated Waveguide SIW Metamaterial BPF with Fractal Slots	Accepted
3	Evanescent-mode Half-Mode Substrate Integrated Waveguide Bandpass Filter	Submitted

وزارة التعليم العالي والبحث العلمي
جامعة الفرات الاوسط التقنية
الكلية التقنية الهندسية ـ نجف

تصميم وتنفيذ مرشح شريطي كسوري لتمرير الحزمة باداء المادة الخارقة

رسالة مقدمة الى

قسم هندسة تقنيات الاتصالات في الكلية التقنية الهندسية ـ نجف

وهي جزء من متطلبات نيل درجة ماجستير تقني في هندسة الاتصالات

تقدم بها

محمد يعقوب يوسف الخفاجي

بكالوريوس في هندسة تقنيات الاتصالات

إشراف

الاستاذ الدكتور فارس محمد علي الجعيفري

نيسان/ 2023

الخلاصـــــه

المفتاح الرئيسي لهذا العمل البحثي هو استكشاف وتحقيق مرشحات جديدة لتمرير الموجات الدقيقة , بتطوير الاداء العام مع تصغير الحجم باستخدام مميزات الدليل الموجي المطبوع (الدليل الموجي متكامل الركيزة), مثل نمط المجال الزائل في الدليل الموجي متكامل الركيزة ونمط نصف الدليل الموجي متكامل الركيزة. عادة لايفضل سلوك نمط المجال الزائل (نمط عدم الانتشار) في هياكل المايكرويف, حيث يعمل هذا النوع من النمط تحت تردد القطع للدليل الموجي . وهكذا , فأن الرسالة تجمع بين نمط المجال الزائل وخصائص المادة الخارقة في تصميم واحد لتحويل نمط عدم الانتشار الى نمط انتشار حيث ان التصميم المقترح يستفيد من كلتا التقنيتين.

الجزء الاول للتصميم , هو لتصميم خلية وحدة اساسية والتي تعتبر العلامة الفارقة للعمل المقدم في هذا الرسالة. يتم خفر او خدش منحي الشكل الكسوري من الطبقة العليا للدليل الموجي متكامل الركيزة حيث يساعد هذا الاجراء في تغيير اشارات وقيم السماحية والنفاذية للدليل الموجي متكامل الركيزة. حيث ان الانتشار يحصل فقط عندما تكون كلا القيم موجبة او كلاهما سالبة, في الحالة الاولى يدعى بنمط الانتشار الامامي واما في الحالة الثانية يدى بنمط الانتشار العكسي.

يدعم وضع الانتشار (الأمامي) كلاً من سرعات الطور والمجموعة في نفس الاتجاه ، بينما تكون هاتان السرعتان في الاتجاه المعاكس في وضع عدم الانتشار (العكسي).
تم تصميم خلية الوحدة و تحليلها و محاكاتها و تصنيعها و اختبارها, خلية وحدة الدليل الموجي متكامل الركيزة بدون فتحة كسورية لها تردد قطع يبلغ 5.2 جيجاهرتز, في حين ان الدليل الموجي متكامل الركيزة مع وجود فتحة كسورية تعمل بتردد رنين يبلغ 2 جيجاهرتر. علاوة على ذلك, يتم استخدام التكرارات الاولى والثانية والثالثة للمنحنيات الكسورية المعتمدة لتصميم خلايا الوحدة. اعتمادا على هذه التحقيقات كانت نسب التصغير التي تم الحصول عليها 32.9% و 51.6 % لتكرار الثاني والثالث على التوالي مقارنتا مع التكرار الاول.

بعد ذلك يتم تركيب رنانات خلية الوحدة خطيا لتصميم الترتيب الاول والثاني والثالث لمرشحات تمرير النطاق ذات الوضع الكامل من الدليل الموجي متامل الركيزة والتي تعمل بالقرب من 2 جيجاهرتز. تتمتع هذه المرشحات بأداء جيد بوجود خطوط نقل صفرية لتحسين الاداء العام.

معاملات الارسال (S_{21}) قريبة جدا من (صفر ديسيبيل) ,مما يدل على ان المرشحات المقترحة لها خسائر منخفضة تقترب من الصفر. ايضا , تكون معاملات الانعكاس (S_{11}) اقل من (10 ديسيبيل) , مما يظهر توافقا جيدا داخل نطاق التمرير.

تم تصنيع واختبار مرشحين وكانت نتائج المحاكاة والقياس متوافقة بصورة جيدة جدا

اخيرا, تم محاكاة وتصنيع واختبار مرشحات تمرير النطاق ذات النمط النصفي في الدليل الموجي متكامل الركيزة. كما سيتم توضيحة في الرسالة فأن هذه المرشحات لها نفس استجابات مرشحات النمط الكامل للدليل الموجي متكامل الركيزة. يساعد هذا الاجراء في تقليل الحجم الكلي بنسبة 50% لتصميم هياكل الموجات الدقيقة. يتم استغلال الجدار المغناطيسي الطولي في دليل الموجة متكامل الركيزة لتحقيق هذه المهمة. ايضا تم اجراء مقارنة بين نتائج المحاكاة والنتائج المقاسة عمليا.